LOCALIZED BANDS AND THEIR EFFECTS IN THE STRONGLY CORRELATED *d* AND *f* ELECTRON SYSTEMS: A FIRST PRINCIPLES STUDY

by

HORI PADA SARKER

DISSERTATION

Submitted in partial fulfillment of the requirements

for the degree of Doctor of Philosophy at

The University of Texas at Arlington

August 2021

Arlington, Texas

Supervising Committee:

Muhammad N. Huda, Ph.D., Supervising Professor
Alex Weiss, Ph.D.
Qiming Zhang, Ph.D.
Ali Koymen, Ph.D.
Jonathan Asaadi, Ph.D.

ABSTRACT

LOCALIZED BANDS AND THEIR EFFECTS IN THE STRONGLY CORRELATED *d* AND *f* ELECTRON SYSTEMS: A FIRST PRINCIPLES STUDY

Hori Pada Sarker, Ph.D.

The University of Texas at Arlington, 2021

Supervising Professor: Muhammad N. Huda, Ph.D.

Strongly correlated materials such as *d* and *f*-electron systems manifest a broad range of interesting phenomena such as metal-insulator transition, high temperature superconductivity, topologically insulating behavior etc. Due to the highly localized nature of *d* and *f*-electrons, they are tightly bound about the associated atoms within the crystal lattice and hence strongly interact with intra-site electrons and the corresponding ionic cores. Such a strong localization of electrons results in the creation of polaron quasi-particles in strongly correlated system like $BiVO_4$, a promising photoanode material for photoelectrochemical (PEC) water splitting for H_2 fuel generation using solar irradiation. Using first principles density functional theory (DFT), we have theoretically characterized the polaron formation in $BiVO_4$ and have studied the transport behavior of polarons within $BiVO_4$ crystal. We have also studied the aliovalent doping mechanism of polaron formation suppression in $BiVO_4$. In conjunction with the *d*-electron system like $BiVO_4$, we have also studied solid solutions with rare-earth chalcogenides, $Ca(La_{1-x}Ce_x)_2S_4$ ($0 \leq x \leq 1$). The rear-earth chalcogenides are strongly correlated 4*f*-electron systems. Using post DFT methods (DFT+U theory), we have theoretically determined the optical transition mechanism of experimentally observed colors for $Ca(La_{1-x}Ce_x)_2S_4$ ($0 \geq x \geq 1$). This Ph.D. research is divided into four different projects: 1) The 1st project demonstrated the electronic band structure engineering of *d*-electron system, $BiVO_4$. In this project, the highly

localized V 3d bands within the conduction band of $BiVO_4$ were replaced by less localized Nb 4d-orbitals via isovalent substitutional doping. We have tested the effect of hydrostatic pressure on the microscopic structure of $BiVO_4$ as well as the stability of Nb-doped $BiVO_4$ metastable excited states, and how it affects the transport of free carriers by means of effective mass calculations. 2) The 2nd project is about theoretical characterization of polaron formations in $BiVO_4$, and the calculation of polaronic electronic structure. We have explored how polaron adversely affects the transport of carriers and limits the available photovoltage of $BiVO_4$ by pinning the quasi Fermi-level splitting. 3) In the 3rd project, we have demonstrated a mechanism to suppress polaron formations in $BiVO_4$ crystal lattice. I have applied the aliovalent doping mechanism to suppress polaron formation and showed that this mechanism could serve as a powerful tool to suppress polaron formation in other materials. 4) The 4th and the last research project was to investigate the role of *f*-electrons toward structural, opto-electronic, and magnetic properties of strongly correlated 4*f* systems- $Ca(La_{1-x}Ce_x)_2S_4$ solid solution. In this project, we have successfully explained the optical transition mechanism responsible for experimentally observed color as well insulating to semiconducting to metallic phase transition based on electronic structure calculations. Overall, this dissertation will help to understand some aspects of the electronic structure and transport properties of strongly correlated *d* and *f*-electron materials. The dissertation not only shows the applicability and limitations of the DFT in understanding the strongly correlated systems, but also will facilitate the search for the suitable and efficient materials for solar energy conversions.

DEDICATION

I would like to dedicate this dissertation to all my family members-especially to my loving parents and my lovely wife for their limitless support, encouragement and genuine love.

TABLE OF CONTANTS

LIST OF FIGURES

LIST OF TABLES

Chapter 1: Introduction

Strongly correlated electron systems manifest a wide range of unique and unconventional physical phenomena. These include unconventional superconductivity[1], topologically insulating (TI) behavior[2,3], metal-insulator phase transition (Mott transition)[4], Kondo-effect[5,6], quantum criticality[7], heavy fermions[5], quantum spin-liquid (QSL)[8] etc. All these unique but technologically important materials properties of strongly correlated systems made them a highly active area of research in condensed matter physics. The understanding of these exquisite behaviors stemming from the strong correlation of electrons in the strongly correlated materials was regarded as one of the challenges for the next decades by the U.S. National Academy of Sciences on the current status of condensed matter and materials physics[9]. The U.S. Department of Energy (DOE) also identified the understanding of complex behaviors of strongly correlated systems as a grand challenge[10]. In general, materials having partially filled *d* or *f* electrons belong to the category of strongly correlated materials system. In periodic table, the transition metal, rare-earth as well as actinide group elements and their derivatives (oxides or chalcogenides) fall into the category of strongly correlated system. Due to the spatial confinement of *d* and *f* orbitals, the valence electrons in these orbitals experience strong Coulomb repulsion and possess less kinetic energy (i.e., they produce narrow energy bands)[11]. In the strongly correlated materials system, the ratio of Coulomb repulsion and kinetic energy among electrons is too large. Due to strong repulsion between electrons in a given orbital, electrons cannot be treated independently within the orbital, rather the influence among each other become highly prominent. In this scenario, the motion of the electrons within these orbitals become strongly correlated, and hence the name “strongly correlated materials”. The strong correlation of electrons has profound effect in terms of materials properties in the strongly

correlated materials system. The interplay among the internal degrees of freedom i.e., spin, charge, and orbital moment of *d* and *f* electrons create a whole lot of exotic ordering phenomena among the strongly correlated materials, and these phenomena are very susceptible to the small variation of external parameters i.e., pressure, temperature, electric or magnetic field, doping concentration etc. Unlike *d* and *f* orbitals, which are highly localized, *s* and *p* orbitals are more delocalized, and electrons in these orbitals spend very short amount of time around the constituent atomic sites (which indicates the highly itinerant behavior). Due to the highly localized nature (i.e., high spatial confinement) of *d* and *f* orbitals, electrons tend to spend longer time around a given atomic site within the crystal lattice, and hence shows the tendency to be localized around this specific atom. Sometimes, highly localized *d* and *f* valence electrons interact with the itinerant conduction electrons and create fascinating phenomena such as localized-itinerant crossover[12,13]. Due to the highly localized character of *d* and *f* orbitals along with localized-itinerant crossover behavior, the numerical simulation of *d* and *f* electron materials possess a great challenge in the area of research in condensed matter physics and become the testing ground of different electronic structure calculations method. In light of this, I have explicitly studied one representative material for *d* electron system and one solid solution series as a representative for *f* electron system in this thesis. As a representative model system for *d* electron materials, I have used $BiVO_4$, a prominent photocatalyst material for photoelectrochemical (PEC) H_2O splitting for H_2 fuel generation using sunlight as well as pollutant degradant for environmental remediation. On the other hand, for *f* electron materials, I have used Ce containing $Ca(La_{1-x}Ce_x)_2S_4$ ($0 \leq x \leq 1$) solid solution as a representative model system.

$BiVO_4$ is regarded as one of the benchmarked photocatalyst material for PEC H_2O splitting for H_2 generation[14,15]. Suitable band gap (~2.40 eV), near suitable band edge position with respect to H_2O redox potential, and good absorption of sunlight in the visible spectrum, high stability against photo-corrosion in electrolyte medium etc. are the features which made $BiVO_4$ stand out among other available photocatalyst materials for PEC H_2O splitting[14–16]. Even though, $BiVO_4$ theoretically meets the necessary criteria to be an efficient H_2O splitting photocatalyst, in reality, it suffers severely in terms of solar to H_2 (STH) conversion efficiency. Theoretically, $BiVO_4$ supposed to reach a maximum of 10% STH conversion efficiency[17,18], but until now only 1.1% STH conversion efficiency was reported for a stand-alone $BiVO_4$ PEC reactor[19,20]. The limitation of STH conversion efficiency originates from the low carrier transport in $BiVO_4$, and it has high rate of carrier recombination[21–23]. Due to the presence of highly localized V 3d orbitals in the conduction band and O 2p orbitals in the valence band in $BiVO_4$, free carriers (electrons and holes) move extremely slow (on the order of 10^{-4} cm^2 V^{-1} s^{-1} at 300K in $BiVO_4$, which is sufficiently slower than the carrier mobility (of the order of 10^2-10^3 cm^2 V^{-1} s^{-1} depending on doping level at 300K[24]) in single crystal Si. As a consequence, the free carriers such as electrons and holes interact strongly with the phonons created from the lattice vibrations and get trapped at vanadium (V) and oxygen (O) atomic sites, respectively, and form electron and hole polaron within the bulk of $BiVO_4$. Polarons are massive quasiparticles, and they form when electrons or holes get dressed up by the virtual phonons created from the lattice vibrations within the crystal lattice. Polarons form when slow moving carriers distort the lattice locally and generate an attractive potential well where the free carriers fall and get trapped[25]. Depending on the spatial extension of the local lattice distortion, polarons can be small polaron or large polaron. If the local lattice distortion is smaller compared to the unit cell dimensions then polarons are small,

otherwise they are classified as large polarons. Like other *d* electron systems i.e., α-Fe_2O_3, TiO_2, Cu_2O, $CuFeO_2$ etc., $BiVO_4$ forms small polarons. Polarons limit the STH conversion efficiency within $BiVO_4$ in the following ways: 1) Polarons restrict the mobility of the free carriers; 2) They generate deep and localized electronic states within the band gap of the material, which act as an active recombination center for the free carriers; 3) They limit the available photovoltage which can be achieved from the material by restricting the splitting of quasi-Fermi level. In the following later chapters, I will be describing theses in a detail manner.

As a representative of *f* electron materials system, I have studied Ce containing $Ca(La_{1-x}Ce_x)_2S_4$ ($0 \leq x \leq 1$) solid solution. In this solid solution, the parent compound, $CaLa_2S_4$ does not contain any *f* electrons and it is widely used in different nonlinear infrared optical applications[26,27]. The solid solutions were formed by gradually increasing the Ce concentration by means of substitutional doping in place of La atom in the crystal lattice. In order to do the substitutional doping, I have followed a magnetic moment guided site selection rule which I will be describing in detail in chapter 7. The end member of the solid solution, $CaCe_2S_4$ contains the maximum *f*-electron density compared to the other compositions within the solid solution series, and it is used as a colorful coating material[28]. In order to study the whole solid solution series, along with first and last member of solid solution, I have considered three intermediate compositions containing 25%, 50% and 75% Ce concentration, and they are: $Ca(La_{0.75}Ce_{0.25})_2S_4$, $Ca(La_{0.50}Ce_{0.50})_2S_4$, and $Ca(La_{0.25}Ce_{0.75})_2S_4$. The aim of this study was to understand the physics of strongly correlated *f* electrons and how they play a critical role in determining materials properties such as structural, magnetic, and optoelectrical properties as well as to understand different phase transitions i.e., insulating to semiconducting to metallic phase transition and non-magnetic to antiferromagnetic phase transition. Along with the understanding of the role of *f*-

electrons, I have also tried to explain the origin of experimentally observed n-type conductivity as well as the optical transition mechanism responsible for different observed colors within these compounds. The detail of this study will be presented in chapter 7.

Finally, this dissertation is organized as follows: chapter 2 and 3 give explicit description of the computational methodology used in thses studies and the foundation of polaron theory, respectively. Chapter 4 explains the band structure engineering of $BiVO_4$ by means of Nb substitutional doping as well as the effect of hydrostatic pressure on the microstructure of $BiVO_4$ as well as it's transport behavior. Chapter 5 describes the theoretical characterization of polaron formation in $BiVO_4$ and how polarons act as a major bottleneck towards reaching the predicted theoretical STH conversion efficiency. Chapter 6 demonstrates the conventional yet very powerful aliovalent doping mechanism of polaron formation suppression in $BiVO_4$. Finally, chapter 7 presents the role of *f* electrons toward determining structural, electronic, optical, and magnetic properties of Ca $(La_{1-x}Ce_x)_2S_4$ $(0 \leq x \leq 1)$ solid solution. Overall, this dissertation will serve as an important guidance towards improving the transport properties of other strongly correlated materials as well as to design technological applications based on *d* and *f* electron materials.

References:

[1] M. Capone, M. Fabrizio, C. Castellani, and E. Tosatti, Science (80-.). **296**, 2364 (2002).

[2] B. Yan, H.-J. Zhang, C.-X. Liu, X.-L. Qi, T. Frauenheim, and S.-C. Zhang, Phys. Rev. B **82**, 161108 1 (2010).

[3] S. Raghu, X.-L. Qi, C. Honerkamp, and S.-C. Zhang, Phys. Rev. Lett. **100**, 156401 1 (2008).

[4] H. Zheng and L.K. Wagner, Phys. Rev. Lett. **114**, 176401 (2015).

[5] F. Steglich and S. Wirth, Reports Prog. Phys. **79**, 084502 (22pp) (2016).

[6] I. Aviani, M. Miljak, V. Zlatić, K.D. Schotte, C. Geibel, and F. Steglich, Phys. Rev. B **64**, 184438 (2001).

[7] P. Coleman and A. J. Schofield, Nature **433**, 226 (2005).

[8] W. Liu, Z. Zhang, J. Ji, Y. Liu, J. Li, X. Wang, H. Lei, G. Chen, and Q. Zhang, Chinese Phys. Lett. **35**, 117501 (2018).

[9]*Committe on CMMP 2010, Condensed Matter and Materials Physics: The Science of the World Around US (National Academies Press, Washington, DC, 2007)* (n.d.).

[10]*Basic Energy Sciences Advisory Committee (BESAC) Grand Challenges Subcommittee, Directing Matter and Energy: Five Challenges for Science and the Imagination, (U.S. Department of Energy, Washington, DC, 2007)* (n.d.).

[11] G. Kotliar and D. Vollhardt, Phys. Today **57**, 53 (2004).

[12] H.C. Nguyen and J.B. Goodenough, Phys. Rev. B **52**, 8776 (1995).

[13] H. Lu and L. Huang, Phys. Rev. B **94**, 1 (2016).

[14] Y. Park, K.J. Mc Donald, and K.S. Choi, Chem. Soc. Rev. **42**, 2321 (2013).

[15] K. Sivula and R. Van De Krol, Nat. Rev. Mater. **1**, (2016).

[16] T.W. Kim and K.-S. Choi, Science (80-.). **343**, 990 (2014).

[17] M.S. Prévot and K. Sivula, J. Phys. Chem. C **117**, 17879 (2013).

[18] R. Li, H. Han, F. Zhang, D. Wang, and C. Li, Energy Environ. Sci. **7**, 1369 (2014).

[19] Q. Wang, T. Hisatomi, Q. Jia, H. Tokudome, M. Zhong, C. Wang, Z. Pan, T. Takata, M. Nakabayashi, N. Shibata, Y. Li, I.D. Sharp, A. Kudo, T. Yamada, and K. Domen, Nat. Mater. **15**, 611 (2016).

[20] Q. Wang, T. Hisatomi, Y. Suzuki, Z. Pan, J. Seo, M. Katayama, T. Minegishi, H. Nishiyama, T. Takata, K. Seki, A. Kudo, T. Yamada, and K. Domen, J. Am. Chem. Soc. **139**, 1675 (2017).

[21] T.S. Sinclair, B.M. Hunter, J.R. Winkler, H.B. Gray, and A.M. Müller, Mater. Horizons **2**, 330 (2015).

[22] Y. Ma, S.R. Pendlebury, A. Reynal, F. Le Formal, and J.R. Durrant, Chem. Sci. **5**, 2964 (2014).

[23] Y. Liang, T. Tsubota, L.P.A. Mooij, and R. Van De Krol, J. Phys. Chem. C **115**, 17594 (2011).

[24] A.J.E. Rettie, W.D. Chemelewski, J. Lindemuth, J.S. McCloy, L.G. Marshall, J. Zhou, D. Emin, and C.B. Mullins, Appl. Phys. Lett. **106**, 022106 (2015).

[25] D. Emin, *Polarons* (Cambridge University Press, Cambridge, 2012).

[26] Y. Li, L. Zhang, and Y. Wu, RSC Adv. **6**, 34935 (2016).

[27] P.J. Walker and R.C.C. Ward, Mater. Res. Bull. **19**, 717 (1984).

[28] P. Sotelo, M. Orr, M.T. Galante, M.K. Hossain, F. Firouzan, C. Longo, A. Kormányos, H. Sarker, C. Janáky, M.N. Huda, K. Rajeshwar, and R.T. Macaluso, Inorg. Chem. **58**, 4553 (2019).

Chapter 2: Methodology

2.1. Theoretical Development of Density Functional Theory (DFT)

Density Functional Theory (DFT) is a first principles based numerical method uses to calculate the electronic structure of many body system ranging from physics, chemistry, materials science, and even to biological systems[1,2]. The elegance of density functional theory (DFT) lies within its simplicity though it is mathematically rigorous. The governing idea behind the DFT is to use the electronic density instead of many-body wavefunction in order to describe many-body interacting systems. DFT reduces the 3N degrees of freedom of an N-body interacting system into only three spatial degree of freedom. Over the years, DFT has become one of the most popular and successful theory of all time. The formal origin of density functional theory is dated back in 1964-1965 and come into light from the seminal 1964-65 Hohenberg-Kohn and Kohn-Sham papers[3,4]. Over time, DFT underwent many modifications as it is still going on to give this theory more predictive power and higher accuracy to explain exotic physical phenomena. In the following sections, the development of DFT has been discussed in a concise manner.

2.2. Many-Body Schrödinger equation and Bohn Oppenheimer Approximation

The Hamiltonian of a many-body system having electrons and nuclei can be written as:

$$\widehat{H} = -\sum_{I=1}^{N} \frac{\hbar^2}{2M_I} \nabla_{R_I}^2 - \sum_{i=1}^{N} \frac{\hbar^2}{2m_e} \nabla_{r_i}^2 + \frac{1}{2} \sum_{\substack{I,J \\ I \neq J}} \frac{Z_I Z_J e^2}{|R_I - R_J|} + \frac{1}{2} \sum_{\substack{i,j \\ i \neq j}} \frac{e^2}{|r_i - r_j|} - \sum_{I,i} \frac{Z_I e^2}{|R_I - r_i|}, \qquad (2.2.1)$$

where, the first two terms represent the nuclei and electrons kinetic energy, third and fourth terms represent nuclei-nuclei and electron-electron electrostatic interaction, and finally the fifth term represents the nuclei-electron electrostatic interaction. This Hamiltonian is computationally intractable due to the many-body interactions for a system having Avogadro's number of species.

So, the above Hamiltonian needs simplifications to make it computationally handleable. This Hamiltonian treats electrons and nuclei on an equal quantum mechanical footing. So, the first simplification is to remove the nuclei degrees of freedom from the quantum mechanical problem. Because nuclei are thousand times heavier than electrons and they move much slower than electrons. In 1927, Born and Oppenheimer suggested[5] that, as far as electrons are concerned, nuclei can be approximated as a classical static particle. Using this approximation, nuclei can be replaced by a classical potential, and after solving the electronic part quantum mechanically the nuclear contributions can be added to the total energy. After adopting the Born-Oppenheimer approximation[5], the Hamiltonian in equation (2.2.1) become:

$$\widehat{H} = -\sum_{i=1}^{N} \frac{\hbar^2}{2m_e} \nabla_i^2 + \sum_{i=1}^{N} U_{ion}(r_i) + \frac{1}{2} \sum_{\substack{i,j \\ i \neq j}} \frac{e^2}{|r_i - r_j|}, \qquad (2.2.2)$$

so, the quantum mechanical Schrödinger equation can be written as:

$$\widehat{H}\Psi = E\Psi = -\sum_{i=1}^{N} \frac{\hbar^2}{2m_e} \nabla_i^2 \Psi + \sum_{i=1}^{N} U_{ion}(r_i)\Psi + \frac{1}{2} \sum_{\substack{i,j \\ i \neq j}} \frac{e^2}{|r_i - r_j|} \Psi, \qquad (2.2.3)$$

where, $\Psi(r_1, r_2, r_2 \dots\dots\dots, r_N)$ is a total antisymmetric wave function for N number of systems. This Hamiltonian is still computationally intractable as it stands, even on the largest computers for N larger than 10, a number not large enough to treat most single atoms, let alone molecules or solids.

2.3. Hartree and Hartree-Fock Theory

The many electrons Hamiltonian is given as follows after adopting Born-Oppenheimer approximation[5]:

$$\hat{H} = -\sum_{i=1}^{N} \frac{\hbar^2}{2m_e} \nabla_i^2 + \sum_{i=1}^{N} U_{ion}(r_i) + \frac{1}{2} \sum_{\substack{i,j \\ i \neq j}} \frac{e^2}{|r_i - r_j|}, \qquad (2.3.1)$$

The first term represents the kinetic energy of electrons, the second term represents the external potential set up by the nuclei, and the last term is electron-electron Coulomb interaction term. In this Hamiltonian, all the computational complexity arises from the electron-electron interaction term. In order to make this Hamiltonian computationally tractable, in 1928, Hartree[6] attempted to replace the Coulombic interaction term by an effective electron-electron potential term, $U_{ee}(r)$ and expressed it as follows:

$$U_{ee}(r) = \int dr' \frac{e^2 n(r')}{|r - r'|}, \qquad (2.3.2)$$

where, $n(r)$ represents the number density of electrons and can be expressed as:

$$n(r) = \sum_j |\psi_j(r)|^2, \qquad (2.3.2)$$

where, $\psi_j(r)$ represent single electron wavefunctions. The effective electron-electron potential, $U_{ee}(r)$ means that each of the electron within the system moves in a mean electrostatic field created by all other electrons. After replacing the electron-electron Coulombic interaction term in equation (2.3.2) by the effective electron-electron potential term, $U_{ee}(r)$, the one electron Schrödinger equation become:

$$-\frac{\hbar^2}{2m} \nabla^2 \psi_j + [U_{ion}(r) + U_{ee}(r)]\psi_j = \varepsilon_j \psi_j \qquad (2.3.3)$$

Equation (2.3.3) is known as Hartree equation. The solution of Hartree equation can be writtens as follows:

$$\Psi(r_1, r_2, r_3, \ldots\ldots\ldots, r_N) = \prod_{j=1}^{N} \psi_j(r_j), \qquad (2.3.4)$$

The Hartree product, the right hand side of equation (2.3.4) is not consistent with the Pauli exclusion principle. The total wavefunction of a fermionic many-body system must be antisymmetric with respect to interchanging any pair of electrons in order to obey the Pauli exclusion principle[7]. In 1930, Fock and Slater[8,9] first proposed an antisymmetric wave function which obey the Pauli exclusion principle[7]. The many-body antisymmetric wave function can be expressed as follow:

$$\Psi(r_1\sigma_1 \dots \dots \dots \dots r_N\sigma_N) = \frac{1}{\sqrt{N!}}\sum_s (-1)^s \psi_{s_1}(r_1\sigma_1) \dots \dots \dots \dots \psi_{s_N}(r_N\sigma_N), \qquad (2.3.5)$$

where, the sum is taken over all the permutations, $s = (1 \dots \dots \dots N)$ and σ represents the spin index. The above antisymmetric wave function can be written as determinant form as follows:

$$\Psi(r_1\sigma_1 \dots r_N\sigma_N) = \frac{1}{\sqrt{N!}}\det\begin{bmatrix} \psi_1(r_1\sigma_1) & \psi_1(r_2\sigma_2) \dots \dots \dots & \psi_1(r_N\sigma_N) \\ \vdots & \vdots & \vdots \\ \psi_N(r_1\sigma_1) & \psi_N(r_2\sigma_2) \dots \dots \dots & \psi_N(r_N\sigma_N) \end{bmatrix}. \qquad (2.3.6)$$

This type of wave function is called Slater determinant. As long as the Hamiltonian does not involve spin explicitly, one can solve the Schrödinger equation by defining ψ as:

$$\psi_l(r_i\sigma_i) = \phi_l(r_i)\chi_l(\sigma_i), \qquad (2.3.7)$$

where, $\varphi_l(r_i)$ and $\chi_l(\sigma_i)$ represent spatial and spin functions, respectively. In order to get Hartree-Fock equation, we need to apply the variational principle:

$$\frac{\delta F_H}{\delta\phi_i^*(r_i)} - \frac{\delta}{\delta\phi_i^*}\sum_{i,j}\varepsilon_{ij}\sum_{\sigma_i}\int \phi_i^*(r_i)\phi_j(r_i) = 0, \qquad (2.3.8)$$

where, $F_H\{\Psi\} = \langle\Psi\big|\widehat{H}\big|\Psi\rangle$ and $\langle\Psi|\Psi\rangle = 1$. Application of variation principle on Ψ given in equation (2.3.6) and using equation (2.3.8) leads to the following equation

$$\varepsilon_i \phi_i(r) = -\frac{\hbar^2 \nabla^2}{2m}\phi_i(r) + U_{ion}(r)\phi_i(r)$$

$$+ \phi_i(r) \int dr' \sum_{j=1}^{N} \frac{e^2 \left|\phi_j(r')\right|^2}{|r - r'|}$$

$$- \sum_{j=1}^{N} \delta_{\chi_i \chi_j} \phi_j(r) \int dr' \frac{e^2 \phi_j^*(r')\phi_i(r')}{|r - r'|}. \qquad (2.3.9)$$

Equation (2.3.9) is called Hartree-Fock equation. The first and second terms are simply the kinetic energy and external potential energy term, third term represents the mean-field Hartee term, and finally the last term represents the exchange term.

2.4. Hohenberg-Kohn Theorem

The Density Functional Theory (DFT) comes into light from the two seminal theorems put forward and proven by Hohenberg and Kohn in 1964[3,4]. Hohenberg and Kohn proposed that electron density contains in principle all the information contained in a many body wavefunction. The electron density of a many-electron system at point r is defined as:

$$n(r) = \langle \Psi | \sum_{l=1}^{N} \delta(r - r_l) | \Psi \rangle,$$

$$= N \int dr_1 \dots\dots dr_N \Psi(r_1 \dots\dots r_N) \delta(r - r_l) \Psi(r_1 \dots\dots r_N), \qquad (2.4.1)$$

H-K Theorem-1: For any many body interacting system, the ground state density uniquely determines the external potential in which the electrons reside. In other words, the external potential is a unique functional of the ground state density.

Proof: Let assume that, there exist two external potentials $U_{ion}^{(1)}$ and $U_{ion}^{(2)}$ which generate the same ground state charge density $n(r)$. The two distinct Hamiltonians arising from the external

potentials are $\widehat{H_1}$ and $\widehat{H_2}$ respectively, and the corresponding ground state wave functions are Ψ_1 and Ψ_2. If the ground states of the Hamiltonians are non-degenerate, then we can write-

$$\varepsilon_1 = \langle \Psi_1 | \widehat{H_1} | \Psi_1 \rangle < \langle \Psi_2 | \widehat{H_1} | \Psi_2 \rangle,$$

$$=> \varepsilon_1 < \langle \Psi_2 | \widehat{H_2} | \Psi_2 \rangle + \langle \Psi_2 | \widehat{H_1} - \widehat{H_2} | \Psi_2 \rangle,$$

$$=> \varepsilon_1 < \varepsilon_2 + \int dr\, n(r)[U_{ion}^1 - U_{ion}^2]. \qquad (2.4.2)$$

Interchanging the indices of equation (2.4.2) gives-

$$\varepsilon_2 < \varepsilon_1 + \int dr\, n(r)[U_{ion}^2 - U_{ion}^1]. \qquad (2.4.3)$$

Adding equation (2.4.2) and (2.4.3) yields-

$$\varepsilon_1 + \varepsilon_2 < \varepsilon_1 + \varepsilon_2, \qquad (2.4.4)$$

which is a clear contradiction and thus the theory has been proven by argumentum ad absurdum. Therefore, the two-external potential U_{ion}^1 and U_{ion}^2 must be the same.

H-K Theorem-2: The total energy of a many-electron system can be expressed as a functional of density, $\varepsilon[n(r)]$ and the true ground state density, $n(r)$ minimizes the total energy functional, provided that $N = \int dr\, n(r)$, where N is the total number of electrons.

Proof: The ground state density uniquely determines the external potential and the external potential in turn uniquely determines the ground state wavefunction. So, the other observables of the system such as kinetic energy, electron-electron interaction etc. of the system can also be written as a functional of the density. In that case, the total energy functional can be written as:

$$\varepsilon[n(r)] = T\,[n(r)] + U_{ion}[n(r)] + U_{ee}[n(r)], \qquad (2.4.5)$$

$$=> \varepsilon[n(r)] = F_{HK}[n(r)] + U_{ion}[n(r)], \qquad (2.4.6)$$

where, $F_{HK}[n(r)]$ is a universal functional because it does not depend on the external potential and universal for all systems having N number of particles.

The total energy functional is minimized by the true ground state density, $n_0(r)$. So, we can write-

$$\varepsilon^0 = \varepsilon[n_0(r)] = \langle \Psi^0 \big| \hat{H} \big| \Psi^0 \rangle, \qquad (2.4.7)$$

by the variational principle, a different density, $n'(r)$ will generate higher energy than the ground state energy, ε^0. So,

$$\varepsilon^0 = \varepsilon[n_0(r)] = \langle \Psi^0 \big| \hat{H} \big| \Psi^0 \rangle < \langle \Psi' \big| \hat{H} \big| \Psi' \rangle = \varepsilon'$$

So, the electron density minimizes the total energy functional and only true ground state density minimizes the total energy functional to the ground state energy of the system.

2.5. Thomas-Fermi Theory

Thomas-Fermi Theory[10–12] provides an explicit form of the universal electronic energy functional, $F[n(r)]$, or total energy functional, $\varepsilon[n(r)]$ in terms of density of the system. The idea of Thomas-Fermi theory assumes a system which has non-uniform charge density and charge density varies slowly. Under this assumption, the kinetic energy functional, $T[n(r)]$ and the exchange energy functional, $\varepsilon_{xc}[n(r)]$ can be expressed as follows:

The kinetic energy functional is written as-

$$T[n(r)] = \frac{\hbar^2}{2m}\left(\frac{3}{5}\right)(3\pi^2)^{2/3} \int dr\, n^{5/3}(r), \qquad (2.5.1)$$

and the exchange energy functional, ε_{xc} is given as-

$$\varepsilon_{xc}[n(r)] = -\left(\frac{3}{4}\right)\left(\frac{3}{\pi}\right)^{1/3} e^2 \int dr\, n^{4/3}(r), \qquad (2.5.2)$$

so, the final expression for total energy functional become:

$$\varepsilon[n(r)] = \frac{\hbar^2}{2m}\left(\frac{3}{5}\right)(3\pi^2)^{2/3}\int dr\, n^{5/3}(r) + \int dr\, n(r)U_{ion}(r) + \frac{1}{2}\iint dr_1 dr_2 \frac{e^2 n(r_1)n(r_2)}{|r_1 - r_2|} -$$

$$-\left(\frac{3}{4}\right)\left(\frac{3}{\pi}\right)^{1/3} e^2 \int dr\, n^{4/3}(r). \qquad (2.5.3)$$

This is known as Thomas-Fermi-Dirac theory[11]. If we omit the last term i.e., the exchange energy functional term, $\varepsilon_{xc}[n(r)]$ from equation (2.5.3), then this above equation become the Thomas-Fermi theory[10,12].

$$\varepsilon[n(r)] = \frac{\hbar^2}{2m}\left(\frac{3}{5}\right)(3\pi^2)^{2/3}\int dr\, n^{5/3}(r)$$

$$+ \int dr\, n(r)U_{ion}(r) + \frac{1}{2}\iint dr_1 dr_2 \frac{e^2 n(r_1)n(r_2)}{|r_1 - r_2|}. \qquad (2.5.4)$$

So, equation (2.5.4) is the Thomas-Fermi theory[10,12].

2.6. Kohn-Sham equations

The modern Density Functional Theory (DFT) came into light as an effective and useful tool to solve complex electronic structure of different physical systems with the inclusion of Kohn-Sham formalism. In 1965, exactly one year after Hohenberg-Kohn theorems, Kohn and Sham published their paper[4] which built the foundation of modern DFT. Kohn-Sham ansatz is that the exact ground state density of any interacting physical system can be calculated from the ground state density of a fictitious system of non-interacting particles. This gives a set of equations for the fictitious system of non-interacting electrons. Kohn and Sham then wrote the total energy functional as follows:

$$E[n(r)] = T_s[n(r)]$$

$$+ \int dr\, V_{ext}(r)\, n(r) + \frac{1}{2}\iint dr dr' \frac{n(r)n(r')}{|r - r'|} + E_{XC}[n(r)], \qquad (2.6.1)$$

where, the first term is the Kohn-Sham kinetic energy functional term of non-interacting electrons and the subscript s denotes for single electron. The second and third terms are for external potential and Hartree term, respectively. Finally, the last term is called the exchange and correlation energy functional, and all the many-body effects of electron-electron interactions are contained within this term. The exchange and correlation energy comes from Pauli-exclusion and many-body Coulombic interactions which also include the self-interaction energy of electrons. $E_{XC}[n(r)]$ also includes the difference between the kinetic energy of real interacting electrons and fictitious non-interacting particles. In principle, Kohn-Sham equations can solve the ground state density exactly, but in reality, it cannot because the $E_{XC}[n(r)]$ functional is unknown. In practice, we approximate $E_{XC}[n(r)]$ term to solve for physical systems. Depending on the approximation of $E_{XC}[n(r)]$, DFT comes into many flavors i.e., LDA-DFT, GGA-DFT, Hybrid-DFT etc.. Kohn-Sham system is simply a fictitious system of non-interacting particles having the same ground state density as of the real interacting system.The Kohn-Sham orbitals, $\varphi_i(r)$ of the independent particles can be solved self-consistently by a Schrödinger like equation as follows:

$$\widehat{H}_{KS}\varphi_i(r) = \varepsilon_{KS}\varphi_i(r), \qquad (2.6.2)$$

where, $\widehat{H}_{KS}$ is the Kohn-Sham effective Hamiltonian and ε_{KS} is the respective Kohn-Sham eigenvalues. The Kohn-Sham orbitals, $\varphi_i(r)$ are related to the electron density by the following equation:

$$n(r) = \sum_{i}^{N} |\varphi_i(r)|^2. \qquad (2.6.3)$$

The Kohn-Sham effective Hamiltonian is given as-

$$\widehat{H}_{KS} = -\frac{\hbar^2}{2m}\nabla^2 + V_{KS}(r), \qquad (2.6.4)$$

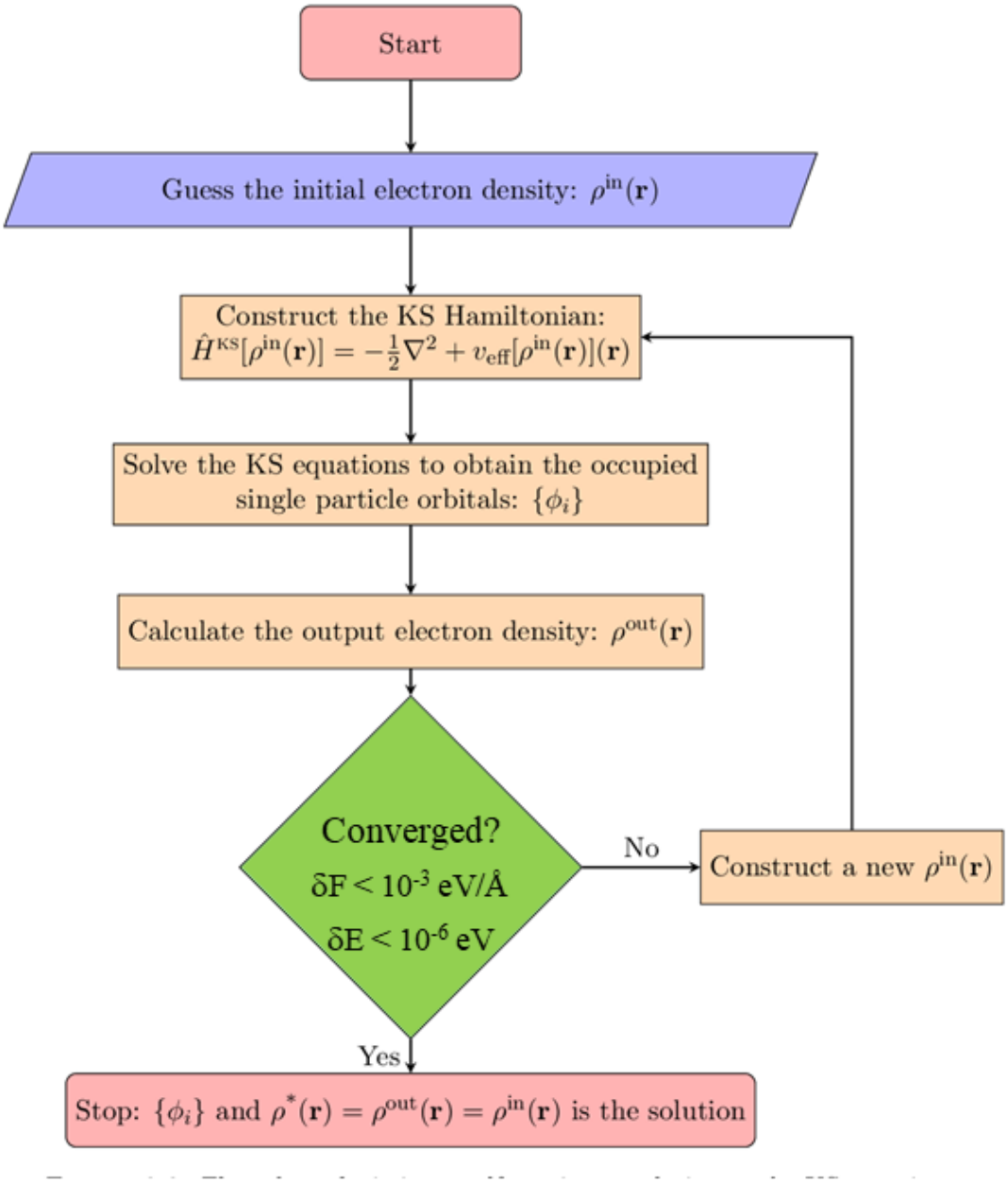

Figure-2. 1: The schematic diagram of Kohn-Sham self-consistent calculation

where, $V_{KS}(r)$ is the Kohn-Sham effective potential and given as-

$$V_{KS}(r) = V_{ext}(r) + V_{Hartree}(r) + V_{XC}(r), \qquad (2.6.5)$$

where,

$$V_{XC}(r) = \frac{\delta E_{XC}[n(r)]}{\delta n(r)}, \qquad (2.6.6)$$

so, $V_{KS}(r)$ is the sum of external potential, Hartree and exchange-correlation potential terms. The schematic diagram (figure-1) shows the workflow of the Kohn-Sham self-consistent calculations.

2.7. Approximation to the exchange-correlation energy functional

In principle, Kohn-Sham DFT can solve the ground state density exactly, but in practice, it can not. Because an important piece of Kohn-Sham equations and that is the exchange-correlation energy functional, $E_{XC}[n(r)]$ is unknown. So, in practice we need to approximate the exchange-correlation energy functional, $E_{XC}[n(r)]$. There are many approximations to the $E_{XC}[n(r)]$. Local density approximation (LDA) and general gradient approximation (GGA) are two mostly used approximations among others.

2.7.1. Local density approximation (LDA)

In 1965, Kohn and Sham proposed the local density approximation (LDA) in the same paper[4] where they published the Kohn-Sham equations. LDA considers the electron gas of uniform density and build the foundation of other approximations of $E_{XC}[n(r)]$. They have proposed the following form of LDA for $E_{XC}[n(r)]$-

$$E_{XC}^{LDA}[n(r)] = \int dr\, n(r)\varepsilon_{XC}^{unif}\big(n(r)\big), \qquad (2.7.1.1)$$

where, $\varepsilon_{XC}^{unif}\big(n(r)\big)$ is the exchange energy per particle of an electron gas of uniform density, $n(r)$. This approximation is exact for uniform electron gas. It is also valid for density that varies slowly over the space i.e.,

$$\frac{|\nabla n(r)|}{n(r)} \ll K_F = (3\pi^2 n)^{1/3}, \qquad (2.7.1.2)$$

and

$$\frac{|\nabla n(r)|}{n(r)} \ll K_s = (n)^{1/6}, \qquad (2.7.1.3)$$

where, K_F and K_s are the local Fermi wave vector and Thomas-Fermi screening length. The exchange energy per particle of a uniform electron gas, $\varepsilon_{XC}^{unif}\big(n(r)\big)$ can be written as a sum of exchange and correlation term as follows:

$$\varepsilon_{XC}^{unif}\big(n(r)\big) = \varepsilon_X^{unif} + \varepsilon_C^{unif}, \qquad (2.7.1.4)$$

where,

$$\varepsilon_X^{unif} = -\frac{3}{4\pi}K_F = -\frac{3}{4\pi}(3\pi^2 n)^{1/3}, \qquad (2.7.1.5)$$

and

$$\varepsilon_C^{unif} = -\frac{a}{b + r_s}, \qquad (2.7.1.6)$$

where, a and b are constants and r_s is the radius of a sphere which contains one electron in average and r_s is written as follows-

$$n(r) = \frac{3}{4\pi r_s^3}, \qquad (2.7.1.7)$$

For high density limit $(r_s \to 0)$, $\varepsilon_C^{unif} = -\frac{a}{b}$ and for low density limit $(r_s \to 0)$, $\varepsilon_C^{unif} = -\frac{a}{r_s} \sim \varepsilon_X^{unif}$.

2.7.2. Generalized Gradient approximation (GGA)

The local density approximation (LDA) considers electron gas of uniform density to approximate the exchange-correlation energy functional, $E_{XC}[n(r)]$. But in reality, systems are not uniformly homogeneous in density. That is why LDA does not model systems correctly. LDA over-binds the atoms or molecules slightly (most of the time) and produces typically shorter bond length and lattice constants compared to the observed one. But in terms of starting point, LDA is an excellent good starting point for the approximation of $E_{XC}[n(r)]$. The next logical step to go beyond LDA approximation is the density gradient expansion approximation (GEA)[13–16]. GEA

starts with the uniform electron gas, then introduces a weak and slowly varying external potential as a perturbation and expands the exchange-correlation energy in terms of the gradient of the density up to 2nd order. The GEA approximation for $E_{XC}[n(r)]$ is as follows:

$$E_{XC}^{GEA}[n(r)] = \int dr \left\{ n(r)\varepsilon_{XC}^{unif}[n(r)] + B_{XC}\big(n(r)\big)\frac{|\nabla n(r)|^2}{n(r)^{4/3}} \right\}, \qquad (2.7.2.1)$$

where, the coefficient, $B_{XC}\big(n(r)\big)$ can be written as-

$$B_{XC}\big(n(r)\big) = B_X + B_C(n). \qquad (2.7.2.2)$$

In practice, the GEA approach turns out to be worse than the LDA. The reason is- GEA violates the fundament sum and sign rule for exchange-correlation hole i.e., $\int n_X(r,r')dr = 0$ and $n_C(r,r') \leq 0$.

Later, D.C. Langreth and J. P. Perdew[17] showed that the 2nd order gradient expansion of the exchange-correlation hole, $n_{XC}(r,r')$ is not the XC hole of any possible physical system. GEA loses the exact constraint on $n_{XC}(r,r')$ that LDA satisfy. This leads to the formulation of the generalized gradient approximation (GGA)[18,19]. According to the GGA approximation, the exchange-correlation energy functional can be written as:

$$E_{XC}^{GGA}[n(r)] = \int dr\, f(n(r), |\nabla n(r)|), \qquad (2.7.2.3)$$

where, $f(n(r), |\nabla n(r)|)$ is a generalized function which contains all orders of $\nabla n(r)$. The early GGA's i.e. Langreth and Mehl[20], Perdew and Wang[21] etc. are constructed from the gradient expansion of the exchange hole, $n_{XC}(r,r')$ and cutting off the spurious long range part to satisfy the sign and sum rule on n_X and n_C. The current approach to construct the GGA is to satisfy the exact constraints on $E_{XC}[n(r)]$, not on n_{XC}. Perdew-Burke-Ernzerhof GGA (PBE-GGA)[18] is the most used GGA exchange-correlation functional in the modern density functional theory. According to PBE-GGA-

$$E_{XC}^{GGA} = E_X^{GGA} + E_C^{GGA}, \qquad (2.7.2.4)$$

$$E_{XC}^{GGA} = \int dr\, n(r)\, \varepsilon_X^{unif}(n)\, F_X^{PBE}(s) + \int dr\, n(r) \left\{\varepsilon_C^{unif}(n) + H^{PBE}(r_s, t)\right\}, \qquad (2.7.2.5)$$

where,

$$F_X^{PBE} = 1 + 0.804 - \frac{0.804}{\left(1 + \frac{0.21951}{0.804} s^2\right)}, \quad with\ s = \frac{|\nabla n(r)|}{2K_F n(r)} \qquad (2.7.2.6)$$

and

$$H^{PBE}(r_s, t) = \frac{\beta^2}{2\alpha} ln\left\{1 + \left(\frac{2\alpha}{\beta}\right)\left(\frac{t^2 + At^4}{1 + At^2 + A^2t^4}\right)\right\}, \qquad (2.7.2.7)\text{ith,}$$

$$A = \frac{2\alpha}{\left(\beta e^{-\frac{-2\alpha\varepsilon_C^{unif}}{\beta^2}}\right) - 1}, \qquad (2.7.2.8)$$

$$\alpha = 0.0716, \beta = 0.066725,$$

$$t = \frac{|\nabla n(r)|}{2K_s n(r)}, \qquad (2.7.2.9)$$

and,

$$K_s = \left(\frac{4K_F}{\pi}\right)^{1/2} \qquad (2.7.2.10)$$

2.8. Hubbard U correction to the Density Functional Theory: DFT+U theory

Density functional theory (DFT)[3,4] with the approximated exchange-correlation functionals, $E_{XC}[n(r)]$, such as LDA[4] and GGA[18] serves as a powerful and convenient numerical tool for materials properties prediction of various classes. DFT with these approximate functionals performs fairly well in terms of structure optimization, total energy as well as electronic structure calculations of simple materials. But DFT drastically fails to predict electronic properties as well as intermolecular interactions and formation energies for strongly correlated systems, especially,

systems having *d* and *f* electrons. DFT severely underestimates one of the important properties of materials, and that is the band gap of strongly correlated materials[22]. It also fails completely to produce localized polaronic solutions for polaron quasi particle calculations of complex ionic materials as well as their charge transport behavior[23–26]. However, predictions of correct descriptions properties related to electronic structures are highly crucial to design electronics and optoelectronic applications as well as other technologies based on strongly correlated materials. For strongly correlated systems, the correlation energy is defined as: $E_c = E_{exact} - E_{HF}$, where E_{HF} represents the Hartree-Fock (HF) approximation of the exact correlation energy, E_{exact}. HF provides mean-field solution of the time-independent Schrodinger equation of a system by using a single Slater determinant where the quantum mechanical exchanges are automatically included, and are exactly described. But the exact exchange integrals of HF theory are missing in widely used local density approximation (LDA[4]) and generalized gradient approximation (GGA)[18] exchange-correlation (XC) functionals. Due to this, LDA or GGA exchange-correlational functionals (XC) dramatically fail to predict the electronic properties like band gap or insulating character of strongly correlated systems. They also provide inaccurate prediction of other physical properties such as lattice parameters of equilibrium crystal structure, magnetic moments, vibrational spectrum etc. On the other hand, hybrid functionals[27,28] are quite successful describing the properties of strongly correlated systems but they are computationally very expensive and intractable for most of the large systems. The failure of DFT to explain the electronic properties of strongly correlated systems is actually attributed from the incapability of treating the proper localization behavior of strongly correlated electrons. The available exchange-correlation functionals (XC) over delocalize the valence electrons of the strongly correlated systems as they are unable to cancel the electron self-interaction in the Hartree term

present in the Hamiltonian[25]. Over time, a lot of research efforts have been given to develop more accurate functionals or applying some corrections to the currently used functionals in order to explain the electronic structure, especially the band gap problem of strongly correlated system. One of corrective approach applied to the existing DFT formulation is DFT+U method[29–31]. The DFT+U method adds an extra Hubbard like Coulombic interaction term U to the localized valence orbitals within the existing DFT method to simulate the proper localization behavior of the strongly correlated electrons. DFT+U method is easily applicable to complex and large system than the other post DFT methods, such as hybrid DFT, and is computationally less expensive. The DFT+U formalism is based on Hubbard model for strongly correlated system.

2.8.1. The Hubbard Model

The Hubbard Hamiltonian is written as follow[32–34]:

$$H_{Hub} = \sum_{ij} \hat{T}_{ij}^{\mu\nu} \sum_{\mu\nu} c_{i\mu}^{\dagger} c_{j\nu} + \sum_{ijkl} \langle \mu_i \nu_j | \sigma_k \tau_l \rangle \sum_{\mu\nu\sigma\tau} c_{i\mu}^{\dagger} c_{j\nu} c_{l\tau}^{\dagger} c_{k\sigma}, \ldots\ldots\ldots\ldots\ldots\ldots (2.8.1.1)$$

where, first term of the Hamiltonian represents the “hopping” or “transfer integral” and indicates hopping of electrons between μ and ν orbitals on the nearest neighbor sites i and j. The explicit form of the “hopping” or “transfer integral” can be written as[35]-

$$\hat{T}_{ij}^{\mu\nu} = \int \phi_{\mu_i}^{*} \left\{ -\frac{1}{2m} \nabla^2 + V_{ext}(r) \right\} \phi_{\nu_j}^{*} dr. \ldots\ldots\ldots\ldots\ldots\ldots\ldots (2.8.1.2)$$

In Hubbard Hamiltonian, this transfer integral is written as a single parameter t. The second term of the Hubbard Hamiltonian corresponds to repulsion integrals of electrons of nearest neighbor sites i, j, k, l with orbitals μ, ν, σ, τ. Since the repulsion between two electrons on the same site is the dominant term and other nearest neighbor contribution is insignificant, Hubbard model neglected the former contributions in the model Hamiltonian. In Hubbard model Hamiltonian,

the same site electron-electron repulsion integral is represented as U. So, in the second quantization form, the Hubbard model Hamiltonian becomes[32–34]:

$$H_{Hub} = t \sum_{\langle i,j\rangle,\sigma} \left(c_{i,\sigma}^{\dagger} c_{j,\sigma} + h.c.\right) + U \sum_{i} n_{i,\uparrow} n_{i,\downarrow}, \qquad (2.8.1.3)$$

where, $\langle i,j\rangle$ represent nearest neighbor atomic sites, $c_{i,\sigma}^{\dagger}$, $c_{i,\sigma}$, and $n_{i,\sigma}$ are electronic creation, annihilation and number operators for electrons of spin σ on site i. $h.c.$ is the Hermitian conjugate. The first term of equation (2.8.1.3) is the site to site hopping term and the amplitude t is proportional to the dispersion of the valence states and represents the single-particle energy term of the total energy. The second term of equation (2.8.1.3) represents the Coulomb repulsion between valence electrons on the same atom and expressed as a product of the occupation numbers of atomic states on the same site and the strength is given by the Hubbard parameter U. Within the DFT+U method, the Hubbard Hamiltonian, H_{Hub} is used to describe strongly correlated valence electronic states (usually, localized d and f orbitals) and the rest of the valence states are treated by the standard DFT approximations. Within the LDA+U[29–31] formalism, the total energy of the system is written as:

$$E_{LDA+U}[n(r)] = E_{LDA}[n(r)] + E_{Hub}\left[\left\{n_{m,m'}^{I,\sigma}\right\}\right] - E_{dc}[\{n^{I,\sigma}\}], \qquad (2.8.1.4)$$

where, E_{Hub} is the electron-electron interaction term for strongly correlated electrons as modeled by the Hubbard Hamiltonian and E_{dc} term is the double counting term that represents the contribution of energy to E_{Hub} coming from correlated electrons as a mean field approximation in DFT and has to be subtracted from E_{Hub}. It is important to note that the Hubbard correction is only applied to the highly localized states and is a functional of occupation numbers that are written as projections of occupied Kohn-Sham orbitals (ψ_{kv}^{σ}) on the states of a localized basis

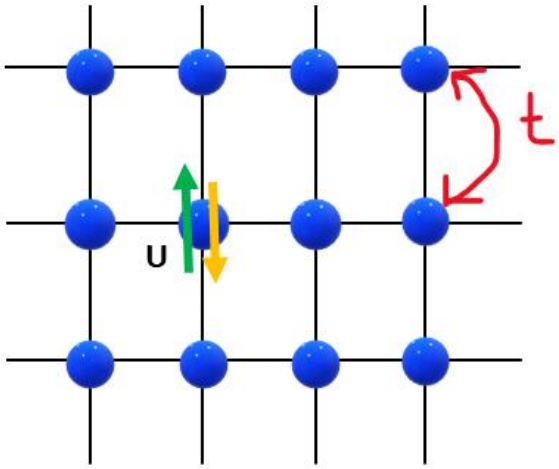

Figure-2. 2: Schematic diagram of parameters of Hubbard model Hamiltonian. The parameter U represents energy penalty of pairing electron in the same atomic site and t represents hopping associated kinetic energy for electron delocalization.

set (ϕ_m^I) as follows:

$$n_{m,m'}^{I,\sigma} = \sum_{k,v} f_{k,v}^{\sigma} \langle \psi_{k,v}^{\sigma} | \phi_{m'}^{I} \rangle \langle \phi_{m}^{I} | \psi_{k,v}^{\sigma} \rangle, \qquad (2.8.1.5)$$

where, $f_{k,v}^{\sigma}$ represents the Fermi-Dirac occupations of the Kohn-Sham states,. k and v denote the k-point and band index. Within the LDA+U framework, the total energy functional in equation (2.8.1.4) can be written as,

$$E_{LDA+U}[n(r)] = E_{LDA} + \sum_{I} \left[\frac{U^I}{2} \sum_{m,\sigma \neq m'\sigma'} n_m^{I\sigma} n_{m'}^{I\sigma'} - \frac{U^I}{2} n^I (n^I - 1) \right], \qquad (2.8.1.6)$$

where, $n_m^{I\sigma} = n_{mm}^{I\sigma}$, and $N^I = \sum_{m,\sigma} n_m^{I\sigma}$, and m is the index for the localized states of same atomic site I. As of equation (2.8.1.4), the second and third term in equation (2.8.1.6) represent the Hubbard and double counting terms, respectively. Even though equation (2.8.1.6) captures the main essence of the LDA+U formalism, the framework of equation (2.8.1.6) is not invariant under rotation of the orbital basis set used to define the occupation of localized states, $n_m^{I\sigma}$. To solve this rotational invariant problem, A. Liechtenstein et. al.[36] introduced a new basis set which is rotationally invariant and independent of LDA+U framework. Within this rotational invariant

formulation, the Hubbard and double counting term of equation (2.8.1.4) and (2.8.1.6) can be expressed as:

$$E_{Hub}\left[\{n^I_{mm'}\}\right] = \frac{1}{2}\sum_{\{m\}\sigma,\mathrm{I}} \{\langle m,m''|V_{ee}|m'm'''\rangle n^{I\sigma}_{mm'} n^{I-\sigma}_{m''m'''} + \langle m,m''|V_{ee}|m'm'''\rangle - \langle m,m''|V_{ee}|m'''m'\rangle n^{I\sigma}_{mm'} n^{I\sigma}_{m''m'''}\}, \quad (2.8.1.7)$$

and,

$$E_{dc}\left[\{n^I_{mm'}\}\right] = \sum_I \left\{\frac{U^I}{2} n^I(n^I-1) - \frac{J^I}{2}\left[n^{I\uparrow}\left(n^{I\uparrow}-1\right) + n^{I\downarrow}\left(n^{I\downarrow}-1\right)\right]\right\}. \quad (2.8.1.8)$$

In equation (2.8.1.7), the integral V_{ee} represents the electron-electron interactions within the wavefunctions of localized basis set such as d or f orbitals, as labeled by index m.

2.9. Dudarev approach to the DFT+U formalism

Depending on the complexity of the Hubbard U term, there are two types of DFT+U formalism. They are rotationally invariant Liechtenstein[36] and Dudarev approach[37]. The Dudarev approach is considered as the simpler version of DFT+U formalism and very popular in computational materials calculations. In this dissertation, we have applied the Dudarev approach to implement DFT+U calculations. The model Hamiltionin within the Dudarev approach is written as follows:

$$\widehat{H} = \frac{U}{2}\sum_{m,m',\sigma} \hat{n}_{m,\sigma}\hat{n}_{m',-\sigma} + \frac{U-J}{2}\sum_{m\neq m',\sigma} \hat{n}_{m,\sigma}\hat{n}_{m',\sigma}, \quad (2.9.1)$$

where, the summation is taken over the magnetic quantum number, m, $m'$and spin quantum number, σ. U and J are the effective on-site Coloumbic and exchange parameters. Within the Dudarev approach, the Hubbard U correction to the DFT functional is considered as an additional correction term which imposes the integer occupation of electrons within the localized states. Within the Dudarev approach to DFT+U formalism, the total energy is written as:

$$E_{DFT+U} = E_{DFT} + E_{nonint.} - E_{int.} \quad (2.9.2)$$

where, E_{DFT} represents the total energy calculated by simple DFT only, $E_{nonint.}$ is the expectation value of $\widehat{H}$ with non-integer number of electrons, and $E_{int.}$ is the expectation value of $\widehat{H}$ with integer number of electrons. The second term of equation (2.9.2) can be expressed as follows:

$$E_{nonint.} = \frac{U}{2} \sum_{m,m',\sigma} n_{m,\sigma} n_{m',-\sigma} + \frac{U-J}{2} \sum_{m \neq m',\sigma} n_{m,\sigma} n_{m',\sigma}, \qquad (2.9.3)$$

where, m and σ are magnetic and spin quantum numbers, respectively. $n_{m,\sigma}$ represents the orbital occupancy and it can be expressed as:

$$n_{m,\sigma} = \sum_{k,v} f_{k,v}^{\sigma} \langle \psi_{k,v}^{\sigma} | P_{mm} | \psi_{k,v}^{\sigma} \rangle. \qquad (2.9.4)$$

Where, P_{mm} is the projector operator and $f_{k,v}^{\sigma}$ indicates the electron occupation number.

The 3rd term of equation (2.9.2) can also be expressed as follows:

$$E_{int.} = \frac{U}{2} \sum_{\sigma} N_{\sigma} N_{-\sigma} + \frac{U-J}{2} \sum_{\sigma} N_{\sigma}(N_{\sigma} - 1), \qquad (2.9.5)$$

where, N_{σ} is expressed as:

$$N_{\sigma} = \sum_{m} n_{m,\sigma}, \qquad (2.9.6)$$

Now, combining equation (2.9.2) with equation (2.9.3) and (2.9.5), E_{DFT+U} can be expressed as:

$$E_{DFT+U} = E_{DFT} + \frac{U-J}{2} \sum_{m,\sigma} \left(n_{m,\sigma} - n_{m,\sigma}^2 \right). \qquad (2.9.7)$$

In matrix notation, equtation (2.9.7) can be expressed as:

$$E_{DFT+U} = E_{DFT} + \sum_{\sigma} \frac{U-J}{2} Tr\left[n_{\sigma} \left(1 - n_{m,\sigma} \right) \right]. \qquad (2.9.8)$$

Equation (2.9.8) represents the total energy functional based on the Dudarev approximation to the DFT+U formalism. It is rotationally invariant because the trace of n_σ and n_σ^2 remain invariant with respect to unitary rotation of the basis set as well as upon matrix diagonalization.

References:

[1] A.E. Mattsson, P.A. Schultz, M.P. Desjarlais, T.R. Mattsson, and K. Leung, Model. Simul. Mater. Sci. Eng. **13**, R1 (2004).

[2] D.W. Koch and D.M.C. Holthausen, *A Chemist Guide to Density Functional Theory* (Wiley-VCH, 2000).

[3] P. Hohenberg and W. Kohn, Phys. Rev. B **136**, B864 (1964).

[4] W. Kohn and L.J. Sham, Phys. Rev. **140**, A1133 (1965).

[5] D. Terme, S. Beitrag, D. Grund, and V. Standpunkte, (1927).

[6] D.R. Hartree, Math. Proc. Cambridge Philos. Soc. **24**, 89 (1928).

[7] W. Pauli, Zeitschrift Für Phys. **31**, 765 (1925).

[8] J.C. Slater, Phys. Rev. **35**, 210 (1930).

[9] J.C. Slater, Phys. Rev. **81**, 385 (1951).

[10] L.H. Thomas, Math. Proc. Cambridge Philos. Soc. **23**, 542 (1927).

[11] P.A.M. Dirac, Math. Proc. Cambridge Philos. Soc. **26**, 376 (1930).

[12] R.P. Feynman, N. Metropolis, and E. Teller, Phys. Rev. **75**, 1561 (1949).

[13] M. Slamet and V. Sahni, Int. J. Quantum Chem. **44**, 333 (1992).

[14] S. MA and K.A. BRUECKNER, Phys. Rev. **165**, 18 (1968).

[15] D.C. Langreth and S.H. Vosko, in *Density Funct. Theory Many-Fermion Syst.*, edited by P.-O.B.T.-A. in Q.C. Löwdin (Academic Press, 1990), pp. 175–199.

[16] L. Kleinman and S. Lee, Phys. Rev. B **37**, 4634 (1988).

[17] D.C. Langreth and J.P. Perdew, Solid State Commun. **17**, 1425 (1975).

[18] J.P. Perdew, K. Burke, and M. Ernzerhof, Phys. Rev. Lett. **77**, 3865 (1996).

[19] J.P. Perdew, K. Burke, and Y. Wang, Phys. Rev. B **54**, 16 533 (1996).

[20] D.C. Langreth and M.J. Mehl, Phys. Rev. B **28**, 1809 (1983).

[21] J.P. Perdew and W. Yue, Phys. Rev. B **33**, 8800 (1986).

[22] I.G. Austin and N.F. Mott, Science (80-.). **168**, 71 (1970).

[23] K.E. Kweon, G.S. Hwang, J. Kim, S. Kim, and S. Kim, Phys. Chem. Chem. Phys. **17**, 256 (2015).

[24] T.J. Smart and Y. Ping, J. Phys. Condens. Matter **29**, 1 (2018).

[25] H.J. Kulik, J. Chem. Phys. **142**, 1 (2015).

[26] M. Cococcioni, *The LDA+U Approach: A Simple Hubbard Correction for Correlated Ground States* (2012).

[27] J. Heyd and G.E. Scuseria, J. Chem. Phys. **118**, 8207 (2003).

[28] J.C. Phys, T.M. Henderson, A.F. Izmaylov, G. Scalmani, G.E. Scuseria, and G.E. Scuseria, J. Chem. Phys. **131**, 1 (2009).

[29] V.I. Anisimov, J. Zaanen, and O.K. Andersen, Phys. Rev. B **44**, 943 (1991).

[30] V.I. Anisimov, I. V. Solovyev, M.A. Korotin, M.T. Czyyk, and G.A. Sawatzky, Phys. Rev. B **48**, 16929 (1993).

[31] I. V. Solovyer, P.H. Dederichs, and V.I. Anisimov, Phys. Rev. B **50**, 16861 (1994).

[32] J. Hubbard, Proc. R. Soc. A Mathemetical, Phys. Eng. Sci. **281**, 401 (1964).

[33] J. Hubbard, Roceedings R. Soc. A Mathemetical, Phys. Eng. Sci. **276**, 238 (1963).

[34] J. Hubbard, Roceedings R. Soc. A Mathemetical, Phys. Eng. Sci. **296**, 82 (1967).

[35] J.C. Slater and G.F. Koster, Phys. Rev. **94**, 1498 (1954).

[36] A. I. Lichtenstein, V.I. Anisimov, and J. Zaanen, Phys. Rev. B **52**, 5467 (1995).

[37] S. L. Dudarev, G.A. Botton, S. Y. Savrasov, C. J. Humphreys and A. P. Sutton, Phys. Rev. B **57**, 1505 (1998).

Chapter 3: Polaron

3.1. Introduction

Polarons are one of the most studied “quasiparticles” among others in condensed matter physics. Polaron is commonly formed among transition metal oxides (TMO)[1–3], organic semiconductors[4,5], conducting polymers[6,7], manganites[8–10], cuprates[11,12], hybrid perovskites[13,14], and 2D materials[15,16]. The beginning of polarons study dated back in 1933 from the seminal paper[17] written by the renowned theoretical physicist Lev Landau. In that paper, he discussed how charge carriers (i.e., electron or hole) moving through a polarizable solid end up getting trapped at atomic sites by the polarization field created from the local lattice distortion. This phenomenology of carrier trapping in materials first coined as polaron by Solomon Pekar[18] in 1946. The charge carrier (electron or hole) and the polarization field associated with it combinedly thought as a single entity as quasiparticle in a solid and was called polaron. Polarons form when slowly moving charge carriers distort the crystal lattice locally, and hence form an attractive potential well for the carriers to fall into. Figure 3.1shows the formation of polaron by carrier trapping in a crystal lattice.

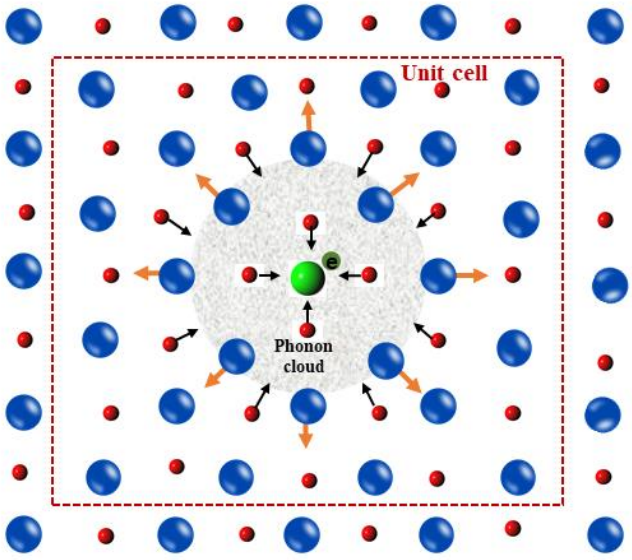

Figure-3. 1: Schematic diagram of polaron formation by self-trapping of carrier (electron) in a crystal lattice site. The green solid ball represents the polaron forming site; black and orange arrows indicate attractive and repulsive forces.

3.2. Polaron classification

Depending on the spatial extension of local lattice distortion, polarons are generally classified as small polaron and large polaron. The extent of local lattice distortion for small polaron is smaller compared to the unit cell dimension, whereas for large polaron, the local lattice distortion extends beyond the unit cell. Figure 3.2 shows a schematic diagram of electron and hole small polaron within a crystal lattice.

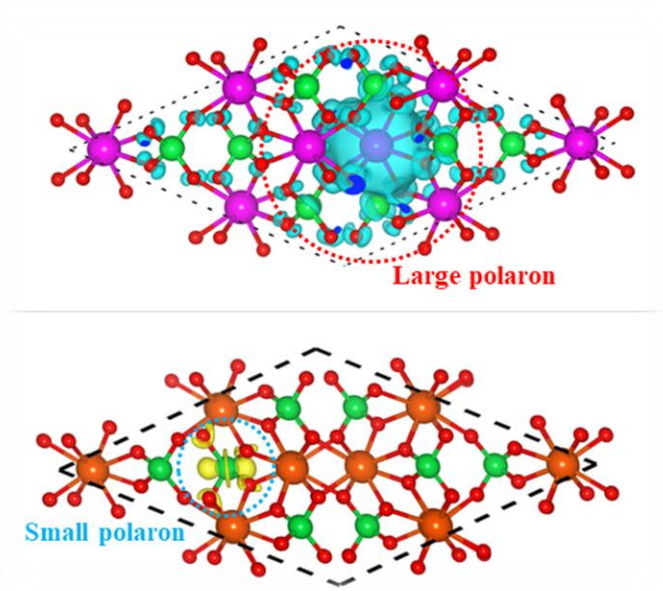

Figure-3. 2: Schematic diagram of large polaron and small polaron. The upper panel shows the large polaron and the lower panel shows the small polaron.

3.3. Polaron Theory

The concept of carrier localization in a perfect crystal due to lattice distortion was first conceptualized by Lev Landau[17], and later on the polaron theory was further developed by the seminal works of Herbert Fröhlich[19,20] and Theodore Holstein[21,22]. After the 1933's seminal work of Lev Landau[17], in 1946 Solomon Pekar[18] quantitatively described the phenomena of a single

electron moving through a polarizable dielectric material like ionic crystal. The resulting formalism is known as Landau-Pekar polaron model. Landau-Pekar model was derived based on the continuum approximation in which ionic crystals were described as continuum of polarizable dielectric medium and electron-electron interaction is expressed in terms of effective-mass approximation. With these approximations, Landau-Pekar polaron model is expressed as:

$$\left\{-\frac{\nabla^2}{2m}-e^2\left(\frac{1}{\varepsilon_\infty}-\frac{1}{\varepsilon_0}\right)\int dr'\frac{|\psi(r)|^2}{|r'-r|}\right\}\psi(r)=E_0\psi(r), \qquad \ldots\ldots\ldots\ldots\ldots(1)$$

where, m is the band mass, ε_0 and ε_∞ are the static and frequency dependent dielectric constant, E_0 is the ground state energy of polaron, and $\psi(r)$ represents polaron wavefunction. The electron-phonon interaction α in Landau-Pekar model is expressed as:

$$\alpha = e^2\left(\frac{1}{\varepsilon_\infty}-\frac{1}{\varepsilon_0}\right)\sqrt{\frac{m}{2\omega_0}}, \qquad \ldots\ldots\ldots\ldots\ldots(2)$$

where, ω_0 represents the longitudinal optical phonon frequency. The acoustic phonon frequency was not considered in Landau-Pekar model because this model was hypothesized within the long-range electron-phonon interaction regime. Due to this long-range interaction, $\varepsilon_0 > \varepsilon_\infty$ (this implies that α is positive), which implies that Landau-Pekar model is only applicable for polar crystals. Later on, Herbert Fröhlich[19,20] hypothesized polaron theory which works very well for large polarons. Fröhlich large polaron theory considered the continuum approximation and long-range electron-phonon interaction very similar to Landau-Pekar polaron model. In second quantization notation, the Fröhlich Hamiltonian is expressed as-

$$\hat{H} = \sum_{k} \varepsilon_k \hat{c}_k^{\dagger}\hat{c}_k + \hbar\omega_0 \sum_{q} \hat{a}_q^{\dagger}\hat{a}_q + \sum_{k,q} V(q)\hat{c}_{k+q}^{\dagger}\hat{c}_k\left(\hat{a}_q + \hat{a}_{-q}^{\dagger}\right),$$

……(3)

where, ε_k is the band energies, ω_0 is the longitudinal optical phonon frequency, $\hat{c}_k^{\dagger}$ and $\hat{c}_k$ are particle creation and annihilation operator having wave vector k, $\hat{a}_q^{\dagger}$ and $\hat{a}_q$ are phonon creation and annihilation operator with wave vector q. The long-range electron-phonon coupling $V(q)$ in Fröhlich Hamiltonian is expressed in terms of volume of the system (v) and dimensionless electron-phonon coupling parameter (α) as follows-

$$V(q) = \left(\frac{2\sqrt{2}\pi\alpha}{v}\right)^{1/2}\left(\frac{1}{q}\right)\left(\frac{\hbar^5\omega_0^3}{m}\right)^{1/4}.$$

……(4)

Even though the Fröhlich Hamiltonian is able to successfully model large polarons in ionic, polar and ferroelectric materials, it completely fails to model small polarons due to the absence of short-ranged electron-phonon interaction term in the model Hamiltonian.

In order to explain the small polaron phenomena in materials, Theodore Holstein[21,22] hypothesized a model Hamiltonian to describe small polaron. The following is the Holstein model Hamiltonian in second quantization notation-

$$\hat{H} = \sum_{k} \varepsilon_k \hat{c}_k^{\dagger}\hat{c}_k + \hbar\omega_0 \sum_{q} \hat{a}_q^{\dagger}\hat{a}_q + \frac{g}{\sqrt{N}}\sum_{k,q} \hat{c}_{k+q}^{\dagger}\hat{c}_k\left(\hat{a}_q + \hat{a}_{-q}^{\dagger}\right),$$

……..(5)

where, g and N represent short-ranged electron-phonon interaction coupling and total number of unit cells. The main difference of Holstein Hamiltonian with the Fröhlich Hamiltonian is that it explicitly considered the discreate nature of crystal. Due to the inclusion of strong short-ranged

electron-phonon interaction in Holstein Hamiltonian, it can successfully explain the small polaron formation phenomenon in non-polar materials.

After almost 90 years later, polaron theory is thriving and still in developing mode. In parallel with continued theoretical advancement of polaron theory, the implementation of polaron theory in various numerical codes nowadays allow to compute polaron related calculations. The first principles Density Functional Theory (DFT) is one of the most popular computational approaches among others i.e., Quantum Monte Carlo (QMC), dynamical mean-field theory (DMFT), and multiscale modeling codes for polaron related calculations. Different physical terms of an effective polaronic Hamiltonian, i.e., the single particle band-structure, phonon dispersion as well as short-ranged and long-ranged electron-phonon interaction terms can be estimated within the framework of the first principle density functional theory. For example, the single particle band energy can be estimated using GW approximations[23,24], hybrid functionals[25,26] as well as DFT+U[27,28] frameworks. The electron-phonon interactions can also be estimated using perturbative approach of density functional Theory[29,30]. Despite the enormous success of density functional theory (DFT) toward materials properties calculation of simple materials, DFT within the local (LDA) and semi-local (GGA) functionals fails to generate localized polaronic solution. Instead, LDA/GGA-DFT produces delocalized solution due to the electron self-interaction correction (SIC) error especially for the highly localized orbitals i.e., d and f-orbitals. In order to reduce the electron self-interaction correction (SIC) embedded in DFT-only theory, various improvements of existing DFT theory have been proposed. These improvements involve inclusion of orbital-selective extra correction terms in the exchange and correlational (XC) functional. Among them, DFT+U[28,31] theory is one of the mostly used DFT framework to study polaron and other highly localized orbital phenomena of strongly correlated

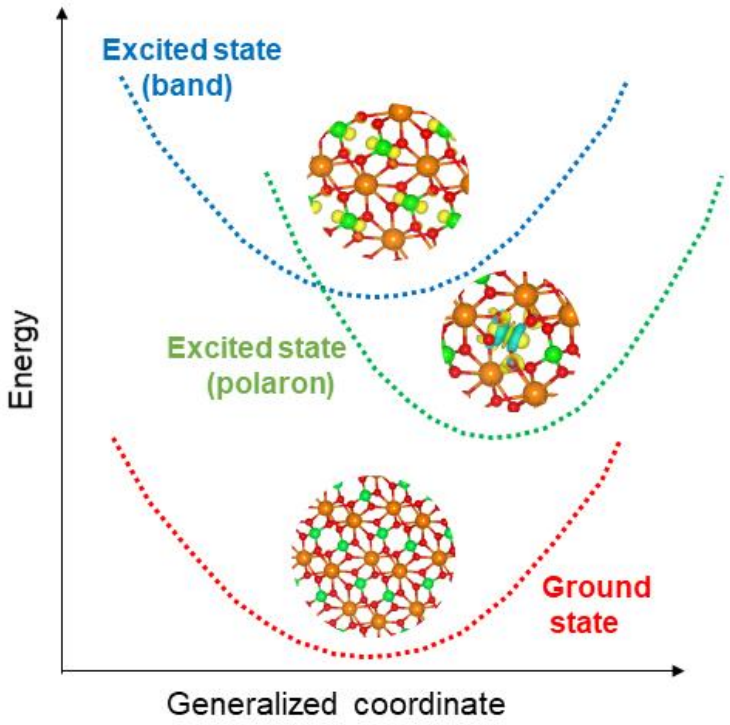

Figure-3.3: Schematic diagram of ground state and excited state (localized and delocalized) structure of a crystal lattice.

systems. In this thesis, I have also used DFT+U[28,31] framework to study polaron in $BiVO_4$. In this framework, an on-site Hubbard U correction term is added to the targeted orbital space in order to retain the correct localized behavior of the localized orbitals i.e., d and f-orbitals. The above mentioned DFT+U framework has been discussed in detail in chapter 2. I have followed the most common method of polaron formation i.e., addition (or subtraction) of an extra electron to (or from) the supercell, to calculate electron (or hole) polaron. In addition to adding (or subtracting) an extra electron, to produce an electron (or a hole) polaronic state, a small perturbation (by means of bond distortion) around a selected polyhedron was applied to break lattice symmetry prior to structural relaxation. Figure 3.3 shows the energetics of localized and delocalized states after applying a small perturbation. Additionally, a compensating homogeneous background counter charge was also added to ensure the charge neutrality of the supercell.

3.4. Polaron hopping activation barrier

Unlike the band transport, polaron transport happens via thermally activated site to site hopping within a crystal lattice.In order to hop from one site to another, polaron has to overcome a hopping activation barrier E_a. In this dissertation, Marcus and Holestein[32,33] framwork has been employed to model the polaron hopping activation barrier. In this framework, polaron hops from intial polaronic configuration to the final polaronic configuration by gradually distorting the crystal lattice. The polaron migration can be described as the gradual change of the distorted polaronic lattice configuration between initial and final polaronic configuration at a specific lattice direction. The intermediate polaronic configurations between the initial and final polaronic configuration can be generated by linear interpolation. In this study, nudge elastic band method developed by Henkelman group at the univeristy of Texas at Austin has been applied to generate the intermediated polaronic configurations between initial and final states. Due to the

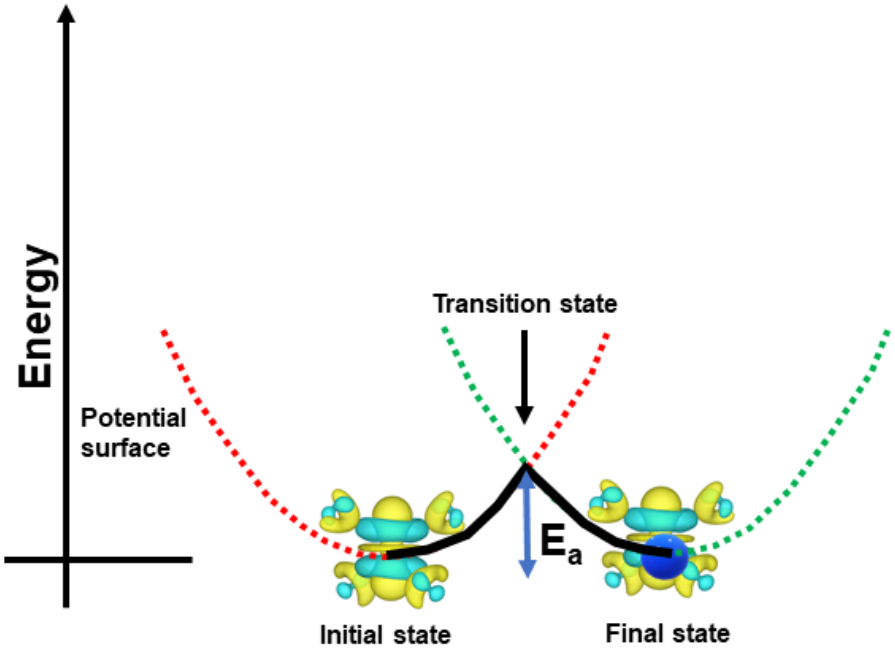

Figure-3. 4: Schematic diagram of polaron migration within a crystal lattice. E_a indicates the polaron hopping activation barrier between initial and final polaronic configuration.

identical nature of the chemical environment (such as atomic coordination, bond lengths etc.) of initial and final polaronic configurations, the transition state (the crossing point of potential surface of initial and final polaronic configuration) occurs at the midpoint between these two configurations. Then the site to site hopping activation barrier E_a can be estimated by taking the energy difference between transition and initial/final polaronic state. Figure 3.4 shows the schematic diagram of site to site polaron hopping as well as the hopping activation barrier.

3.5. Effects of polaron in carrier transport

Polaron plays a crucial role in governing the carrier dynamics i.e., carrier separation, carrier transport as well as reaction kinetics, and hence determine the quantum efficiency of any polaron forming materials. Formation of polaron adversely effects the carrier transport in the following ways: (1) Unlike the free carriers (electron/hole), polaron has comparatively heavy effective mass, hence, they have slow mobility because polaron forms when free carriers get trapped at atomic sites via local lattice distortion; (2) Formation of polaron introduces electronic state within the band gap. Electron polaronic state lies below the conduction band minima (CBM) and hole polaronic state lies above the valence band maxima (VBM). These mid-gap polaronic states restrict the splitting of quasi-Fermi level, and hence limit the available photovoltage which can be achevied from the material; (3) The mid-gap polaronic states sometimes behave as a recombination center for charge carriers, and hence limits the quantum efficiency of the material via carrier recombination efficiency loss channel; (4) For most of the photoelectrochemical (PEC) H_2O splitting photocatalysts, the electron and hole polaronic states straddle below and above the H_2O redox potential, and hence limit the overpotential needed to transfer the charge carriers to the electrolyte medium like H_2O.

References

[1] K.E. Kweon, G.S. Hwang, J. Kim, S. Kim, and S. Kim, Phys. Chem. Chem. Phys. **17**, 256 (2015).

[2] J. Husek, A. Cirri, S. Biswas, and L. Robert Baker, Chem. Sci. **8**, 8170 (2017).

[3] N.A. Deskins and M. Dupuis, Phys. Rev. B **75**, 195212 (2007).

[4] N. Lu, L. Li, D. Geng, and M. Liu, Org. Electron. **61**, 223 (2018).

[5] T. Strobel, C. Deibel, and V. Dyakonov, Phys. Rev. Lett. **105**, 1 (2010).

[6] L. Zuppiroli, M.N. Bussac, S. Paschen, O. Chauvet, and L. Forro, Phys. Rev. B **50**, 5196 (1994).

[7] E.M. Conwell and H.A. Mizes, Phys. Rev. B **51**, 6953 (1995).

[8] A. Daoud-Aladine, J. Rodríguez-Carvajal, L. Pinsard-Gaudart, M.T. Fernández-Díaz, and A. Revcolevschi, Phys. Rev. Lett. **89**, 1 (2002).

[9] C. Jooss, L. Wu, T. Beetz, R.F. Klie, M. Beleggia, M.A. Schofield, S. Schramm, J. Hoffmann, and Y. Zhu, Proc. Natl. Acad. Sci. U. S. A. **104**, 13597 (2007).

[10] C.P. Holfeld, F. Löser, M. Sudzius, K. Leo, P.G. Radaelli, and S.W. Cheong, Phys. Rev. Lett. **81**, 878 (1998).

[11] K.M. Shen, F. Ronning, W. Meevasana, D.H. Lu, N.J.C. Ingle, F. Baumberger, W.S. Lee, L.L. Miller, Y. Kohsaka, M. Azuma, M. Takano, H. Takagi, and Z.X. Shen, Phys. Rev. B - Condens. Matter Mater. Phys. **75**, 1 (2007).

[12] A.S. Alexandrov, J. Supercond. Nov. Magn. **13**, 985 (2000).

[13] D. Cortecchia, J. Yin, A. Bruno, S.Z.A. Lo, G.G. Gurzadyan, S. Mhaisalkar, J.L. Brédas, and C. Soci, J. Mater. Chem. C **5**, 2771 (2017).

[14] F. Zheng and L.W. Wang, Energy Environ. Sci. **12**, 1219 (2019).

[15] M. Kang, S.W. Jung, W.J. Shin, Y. Sohn, S.H. Ryu, T.K. Kim, M. Hoesch, and K.S. Kim, Nat.

Mater. **17**, 676 (2018).

[16] Y. Xiao, Z.Q. Li, and Z.W. Wang, J. Phys. Condens. Matter **29**, (2017).

[17] L.D. Landau, Phys. Z. Sowjetunion **3**, 644 (1933).

[18] S. Pekar, Zhurnal Eksp. I Teor. Fiz. **16**, 341 (1946).

[19] H. Fröhlich, Adv. Phys. **3**, 325 (1954).

[20] H. Fröhlich, H. Pelzer, and S. Zienau, London, Edinburgh, Dublin Philos. Mag. J. Sci. **41**, 221 (1950).

[21] T. Holstein, Ann. Phys. **8**, 325 (1959).

[22] P.I. Thè and P.T. Holstein, Ann. Phys. (N. Y). **281**, 7255773 (2000).

[23] Z. Ergönenc, B. Kim, P. Liu, G. Kresse, and C. Franchini, Phys. Rev. Mater. **2**, 1 (2018)

[24] L. Hedin, Phys. Rev. **139**, A796 (1965).

[25] A.D. Becke, J. Chem. Phys. **98**, 1372 (1993).

[26] C. Franchini, J. Phys. Condens. Matter **26**, (2014).

[27] B. Himmetoglu, A. Floris, S. De Gironcoli, and M. Cococcioni, Int. J. Quantum Chem. **114**, 14 (2014).

[28] V.I. Anisimov, J. Zaanen, and O.K. Andersen, Phys. Rev. B **44**, 943 (1991).

[29] F. Giustino, Rev. Mod. Phys. **89**, 1 (2017).

[30] S. Baroni, S. de Gironcoli, A. Dal Corso, and P. Giannozzi, Rev. Mod. Phys. **73**, 515 (2001).

[31] S. Dudarev and G. Botton, Phys. Rev. B **57**, 1505 (1998).

[32] R.A. Marcus and N. Sutin, Biochim. Biophys. Acta **811**, 265 (1985).

[33] R.A. Marcus, Rev. Mod. Phys. **65**, 599 (1993).

Chapter 4

Niobium doping in $BiVO_4$: an interplay between effective mass, stability, and pressure

Hori Pada Sarker[1], Pratap M. Rao[2] and Muhammad N. Huda[1*]

[1]Department of Physics, University of Texas at Arlington, Arlington, Texas 76019, USA

[2]Department of Mechanical Engineering, Worcester Polytechnic Institute, MA 01609, USA

Published at:

ChemPhysChem

[*] Corresponding author: huda@uta.edu

Abstract

We have applied density functional theory to study the electronic structure changes caused by Nb incorporation in $BiVO_4$ and the application of external pressure. The overall solubility of Nb in $BiVO_4$ is usually high, and the presence of oxygen vacancies affect the dopability of Nb in $BiVO_4$. Through the analyses of the chemical-potential landscape, we have determined the single-phase stability zone of $BiVO_4$ with the Nb doping. The most favorable Nb doping is simultaneous substitutions at both V and Bi sites. Nb substitution at only V-site even though is next favorable, the band gap change is not very significant which agrees with an earlier experiment. However, it does change the electron effective mass by 20% due to the presence of Nb 4d bands in the conduction bands, which explains better catalytic activity by Nb-doped $BiVO_4$. In addition, application of external pressure improved the single-phase stability zone in the chemical-potential landscape. We have also focused on the local structural distortions near the Nb doping site, especially on the BiO_8 octahedra. We have shown here that pressure-induced symmetrization of BiO_8 dodecahedron lower the electron's effective mass further and therefore can help to improve the photo-conduction property of $BiVO_4$.

4. 1. Introduction

For any solar conversion process, a suitable absorber material is necessary to make the conversion process efficient. Given the present state of global warming and the future availability of fossil fuels, it has been a frantic search in recent decades to find such 'suitable' materials. In recent years, $BiVO_4$ attracts attention as a potential photoanode for water oxidation as well as a photo-catalyst for hydrogen evolution via water splitting and environmental remediation by degrading pollutants[1–6]. Earth-abundant for low-cost fabrications, near ideal band gap (2.4-2.5 eV)[2,3,7] for efficient light absorption at visible range, the relative positions of its conduction and valence bands compared to the water reduction potentials[8,9], its optoelectronic responses and nontoxicity are some of the main reasons for this. In fact, monoclinic $BiVO_4$ as a photo-catalyst has been said to achieve one of the highest hydrogen production efficiency among the oxide materials[1–3,7,8,10,11]. Despite these advantages as a potential photo-catalyst, $BiVO_4$ has some limitations, which attribute to its low efficiency. Poor transport of photo-induced carriers, electron-hole recombination and slow reaction kinetics at the interface are the crucial limitations of pristine $BiVO_4$[11–13].

So far, many experimental techniques developed to synthesize $BiVO_4$. The materials quality and stability depend on the experimental environment and routs to synthesize the material. In general, the chosen experimental conditions encourage some defects and impurities and suppress others. These impurities can change the structural as well as the electronic properties of $BiVO_4$ crystals, which may adversely affect its efficiency as a photo-catalyst. On the other hand, some selected impurities may change the electronic properties in the desired way. In fact, doping with appropriate ions and synthesizing it in a corresponding tuned chemical environment is one of the good strategies to overcome the limitations and hence enhancing the photocatalytic properties of

$BiVO_4$. There have been both experimental and theoretical works of $BiVO_4$ in the presence of defects and impurities[12,14–19] to understand such strategies. Theoretical predictions of such strategies and growth environment for the desired dopant in $BiVO_4$ can be an important tool to expedite the search process. In this paper, we will present such predictions for Nb doping in $BiVO_4$.

Like other oxides, electron-hole recombination is one of the major barriers to achieve better photocurrent with $BiVO_4$. A recent study[20] showed the improvement of photocurrent of W-doped $BiVO_4$ by reducing the electron-hole recombination by manipulating the carrier trapping state. Our present study, as well as other studies[12,20], showed that $BiVO_4$ has V 3d band in the conduction band minimum, which contributes to the higher resistivity of the photo-excited electrons. The main motivation for Nb doping is that its 4d band would contribute to the $BiVO_4$'s conduction band minimum, and thereby would lower the electron effective mass; hence, the photoconduction is supposed to improve. Recent studies[15,18] reported the improvement of $BiVO_4$ photocurrent by Nb doping in V-site. Another recent DFT study[16] reported that the formation energy of Nb doping at V-site was the lowest among other transition metal impurities.

Impurity doping in $BiVO_4$ can change the local structure near the doping site. A recent study[20] on W doping on V-site of $BiVO_4$ reported the change of Bi-O ligand bonds of BiO_8 dodecahedron near the W doping site. The ligand bonds of BiO_8 dodecahedron near the doping site became more symmetric as in the dodecahedron of symmetric tetragonal phase. Due to the W doping on V-site of $BiVO_4$, pure monoclinic phase became a 'mixed-phase' of monoclinic and tetragonal phase. Won Jun Jo *et. al*[21] also reported the partial phase transition from pure monoclinic to a mixture of monoclinic and tetragonal phase after In/Mo dual doping in $BiVO_4$.

Given the promise of Nb doping in $BiVO_4$, here we present our systematic study on broader aspects of Nb doping. Previous studies mostly focused on Nb substitution on V-site. However, in one of our previous studies on pyrochlore $Bi_2Ti_2O_7$, we have noticed that transition metal impurities substitutions preferred Bi-site to the transition metal at Ti-site[22,23]. So, here we ask the following questions as well: is substitution on Bi site thermodynamically possible? For photo-electrochemical processes, which one is electronically more desirable: V-site or Bi-site substitution? In general, oxygen vacancies play an important role in oxide materials by rendering them as n-type semiconductors. So, the next question was how these Nb incorporations by substitutions are affected by the presence of the oxygen vacancy. We have shown here that, Nb can substitute either the V- or Bi- sites, where simultaneous Bi- and V-sites substitution being more probable than Bi-site and V-sites substitution separately. With Bi-site substitution, it creates a shallow donor level in the band structure, which implies an Nb at Bi-site as an n-type dopant. We have also discussed the favorable growth condition to incorporate these impurities/defects by avoiding the corresponding binary phases.

In this present study, we have also studied the local structure changes near the Nb doping site of $BiVO_4$. We observed that Nb substitutional doping made the BiO_8 dodecahedron near Nb doping site more distorted. However, I. G. Wood *et. al*[24] reported that external pressure could reduce the distortion of BiO_8 dodecahedron of $BiVO_4$. Also, a recent study[20] reported that less distorted polyhedron contributed to higher photo-activity. In light of these, we have also studied the impact of external pressure on the local structure changes of BiO_8 dodecahedron near the Nb doping site. We observed that upon applying pressure, BiO_8 dodecahedron near the Nb doping site become more symmetric. Symmetric BiO_8 dodecahedron within $BiVO_4$ created relatively more dispersed bands in the band structure and which eventually would make the transport of

photo-induced charge carrier easier and hence improve the photo-current. Also, we have studied the single-phase stability zone of $BiVO_4$ via the chemical potential landscape analysis. We found that it is possible to synthesize a single-phase Nb-doped $BiVO_4$ under thermodynamic conditions. We have also studied the impact of external pressure on single-phase stability zone of $BiVO_4$. We found that the area of single-phase stability region of Nb-doped $BiVO_4$ increases upon applying external pressure. We have noticed that Bi_2O_3 secondary binary phase got separated from $BiVO_4$ phase more clearly than the other binary oxide phases upon applying external pressure. This strategy may help to find a better route to synthesize single-phase $BiVO_4$ photo-catalyst with preferred doping.

4. 2. Computational Methodology

The present calculations were performed using the density functional theory (DFT)[25,26] as implemented in the Vienna ab initio simulation package (VASP[27,28]. The exchange and correlation were treated with the generalized gradient approximation (GGA) proposed by Perdew-Burke-Ernzerhof (PBE)[29]. The projector augmented plane wave (PAW)[30] method was used to treat the core electrons. The Monkhorst-Pack (MP) scheme was used to generate the k-points grid. In this present calculation, for the supercell we used a $3\times3\times5$ k-point mesh which gave a well converge calculation. A plane wave kinetic energy cutoff, E_{cut} of 500 eV was used throughout the calculation. Band gap underestimation is a well-known problem for GGA-PBE calculation. The other approach i.e., hybrid functional or GGA + U calculation can produce a band gap which is close to the experimental value, provided that the choice of amount of HF exchange for hybrid calculation and U value for GGA + U calculations are carefully chosen. For example, a previous study[31] reported the band gap of $BiVO_4$ is 3.41 eV using hybrid calculation including 25% HF exchange functional. Another study[32] reported the band gap of $BiVO_4$ is 2.30

eV using GGA + U method with U = 2.7 eV for V 3d state. The reported experimental band gap of $BiVO_4$ is (2.40 – 2.50 eV). In our present calculation (GGA - PBE), the calculated band gap is 2.10 eV. In this study, our aim was to see how the electronic structure changes when Nb is doped within $BiVO_4$ and the main motivation was to see whether the V 3d band in the conduction band minima get replaced by Nb 4d bands. GGA -PBE calculation gives a good enough qualitative picture of trend in band gap change of BiVO4 and Nb doped $BiVO_4$. We will further investigate $BiVO_4$ using hybrid and DFT + U method later. The visualization software, VESTA[33] was used to visualize and analyze the crystal structure.

4. 3. Relaxed structure of $BiVO_4$

In this study, we have used the clinobisvanite bismuth vanadate structure. Clinobisvanite structure is a widely used $BiVO_4$ structure as opposed to its tetragonal counterpart for its enhanced photocatalytic property[3,5,7,12,14–16,18,34]. It belongs to the monoclinic crystal system and has the space group of C2/c (space group no. 15). The conventional unit cell of the monoclinic clinobisvanite structure consists of 24 atoms, and among them 4 are Bi atoms, 4 are V atoms, and 16 are O atoms. Figure 1 shows the structure used in this calculation. Table 1 presents the calculated values of the lattice parameters of the optimized unit cell. These values of the lattice parameters are in good agreement with the available experimental and theoretical data[34–35]. Monoclinic clinobisvanite structure of bismuth vanadate is formed by alternate layers of Bi and V atoms. Each vanadium atom is coordinated by four oxygen atoms forming an irregular tetrahedron, VO_4, and vanadium atoms sit at the center of the tetrahedron. Eight oxygen atoms coordinate each Bi atom and form an irregular dodecahedron, BiO_8, and Bi atoms sit at the center of the dodecahedron. VO_4 tetrahedrons are isolated and connected with the BiO_8 dodecahedron by sharing one oxygen atom. So BiO_8 is surrounded by eight oxygen atoms comes from eight

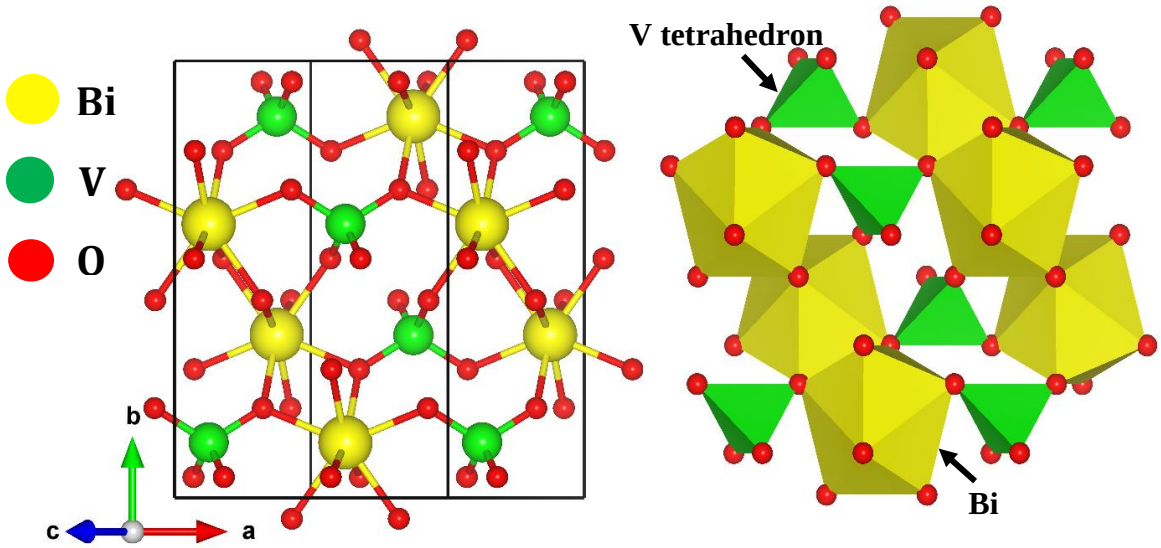

Figure-4. 1: Conventional unit cell of monoclinic clinobisvanite bismuth vanadate.

VO_4 tetrahedra. There are two pairs of distinct V-O bonds within VO_4 tetrahedron and four pairs of distinct Bi-O bonds within the BiO_8 dodecahedron. The calculated V-O bond-lengths are 1.745 Å and 1.744 Å which are very close to the bonds length (1.76 Å and 1.74 Å) obtained by powder X-ray diffraction method[35]. The calculated Bi-O bonds length (2.444 Å, 2.446 Å, 2.495 Å and 2.497 Å) have a little deviation from the bonds length (2.34 Å, 2.38 Å, 2.51 Å and 2.61 Å) with powder X-ray diffraction[35]. Table 2 shows the calculated V-O and Bi-O bond lengths from our calculation as well as from other sources from literature.

Table-4. 1: Crystallographic lattice parameters of monoclinic clinobisvanite bismuth vanadate ($BiVO_4$) conventional unit cell.

	a /Å	**b/Å**	**c/Å**	**β (º)**
This work	7.303	11.750	5.167	135.029
Powder X-ray Diffraction (At room temp.) [34]	7.253	11.702	5.096	134.233

Powder neutron diffraction (At 295 K) [34]	7.247	11.697	5.090	134.226
Powder neutron diffraction (At 4.5 K) [34]	7.258	11.706	5.084	134.073
Theory (PAW calculation) [33]	7.299	11.769	5.145	134.26
Theory [35]	7.224	11.522	5.108	135.003

Table-4. 2: Bi-O and V-O bond lengths within BiO_8 and VO_4 polyhedron of pristine $BiVO_4$.

This study		**X-ray diffraction (at room temp.)[32]**		**Neutron diffraction (at 295 K)[32]**		**Theory[33]**	
Bi-O/Å	**V-O/ Å**	**Bi-O/Å**	**V-O/ Å**	**Bi-O/Å**	**V-O/ Å**	**Bi-O/Å**	**V-O/ Å**
2.444 (2 pairs)	1.745 (2 pairs)	2.34 (2 pairs)	1.74 (2 pairs)	2.354 (2 pairs)	1.69 (2 pairs)	2.416 (2 pairs)	1.730 (2 pairs)
2.447 (2 pairs)		2.38 (2 pairs)		2.372 (2 pairs)		2.418 (2 pairs)	
2.496 (2 pairs)	1.744 (2 pairs)	2.51 (2 pairs)	1.76 (2 pairs)	2.516 (2 pairs)	1.77 (2 pairs)	2.446 (2 pairs)	1.731 (2 pairs)
2.498 (2 pairs)		2.61 (2 pairs)		2.628 (2 pairs)		2.449 (2 pairs)	

4. 4. Defect formation energy and single-phase stability

The method of calculating defect formation energy of a charge-neutral system having defect Ω is[37– 40]

$$E_f(\Omega) = E_{tot}(\Omega) - E_{tot}(\text{host}) + \sum n_\alpha (\mu_\alpha + \Delta\mu_\alpha),$$

where, $E_f(\Omega)$ is the defect formation energy of the system, $E_{tot}(\Omega)$ is the total energy of the system having the defect Ω, E_{tot} (host) is the total energy of the pristine system. The number n_α determines how many atoms of atomic species α is removed from or added to the system: n_α is positive if the atomic species α is removed from the system and negative if it is added to the system. μ_α is the reference chemical potential of the atomic species α in its standard elemental phase; $\Delta\mu_\alpha$ reflects the growth condition, i.e., α-rich or α-poor growth condition. To define these growth conditions first, we define the formation enthalpy, ΔH_f, for a given bulk phase,

$$\Delta H_f = E_{tot}(\text{solid}) - \sum m_\alpha E_\alpha^{bulk},$$

where E_{tot} (solid) is the total energy of the system in its bulk phase, E_α^{bulk} is the energy of a single atom of atomic species α taken out from its standard elemental phase, m_α is the number of atomic species α per formula unit of the solid phase. Now, we define α-rich or α-poor growth condition by the following condition:

$$\Delta H_f \leq n_\alpha \Delta\mu_\alpha \leq 0,$$

where the lower limit $\Delta H_f \leq n_\alpha \Delta\mu_\alpha$ defines the α-poor growth condition where the availability of atomic species α is very rare and the upper limit $n_\alpha \Delta\mu_\alpha \leq 0$ defines the α-rich growth condition where the atomic species α is abundant within the system.

Figure 2 shows the chemical-potential landscape for the $BiVO_4$. The triangle corresponds to the stability zone of $BiVO_4$ for which the chemical-potentials of the constituent elements are constrained by the following equation:

$$\Delta\mu_{Bi} + \Delta\mu_V + 4\Delta\mu_O = -14.3946eV,$$

Where, –14.3946 eV is the formation enthalpy of $BiVO_4$ per formula unit. In ref 14 the chemical potential range of -13.95 eV. The only difference is that we have used 500 eV cutoff energy and

the study in ref 14 used a lower cut off value of 400 eV. So, the small difference in chemical potential range in $BiVO_4$ can be attributed to this minor computational differences.

To avoid the formation of the secondary binary phases[37] following constraints were also considered:

$$2\Delta\mu_{Bi} + 3\Delta\mu_O < \Delta H_f(Bi_2O_3),$$

$$2\Delta\mu_V + 5\Delta\mu_O < \Delta H_f(V_2O_5),$$

$$\Delta\mu_V + 2\Delta\mu_O < \Delta H_f(VO_2),$$

$$2\Delta\mu_V + 3\Delta\mu_O < \Delta H_f(V_2O_3).$$

As long as above equations are satisfied, each of the above binary oxides will not avail enough energy to form. In Figure 2, the shaded area *ABCDE* indicates the single-phase formation zone of $BiVO_4$.

Defect or impurity formation energy of a system gives information about whether the system with the corresponding defect can be formed at thermodynamic equilibrium. Negative values of defect formation energy imply that the defect can be formed spontaneously in the material during its growth process, i.e., an exothermic process. In this present study, we calculated the defect formation energy of Nb substitution at V-site, Nb substitution at Bi-site, and Nb substitution at both V- and Bi-sites simultaneously in the same supercell. Also, we examined all these Nb substitutions with the presence of oxygen vacancies. Figure 3 shows the formation energies for these impurities/defects at the chemical potentials with respect to the single-phase stability zone *ABCDE* as presented in Figure 2. This ensures that the impurities are formed only in the $BiVO_4$, and other binary phases do not interfere. By construction, from point *A* to *E*, oxygen chemical potential progressively increases. For the calculations of impurity formation energies, we used pristine $BiVO_4$ as the host cell. Also, to prevent the formation of the secondary binary phase

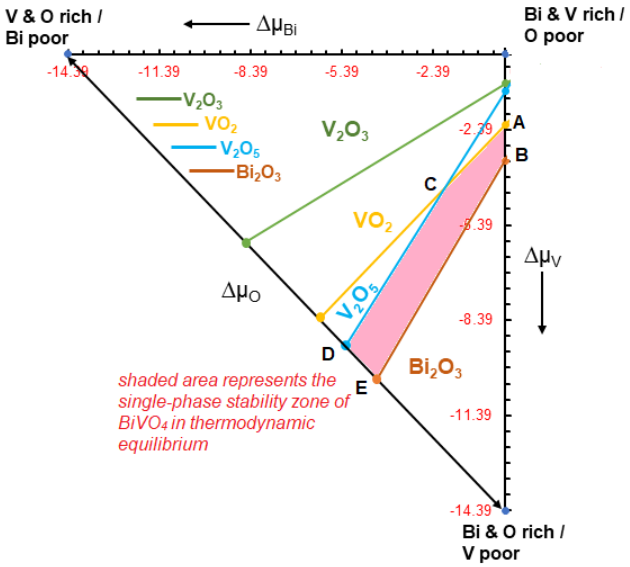

Figure-4. 2: Chemical potential landscape for the stability zone of $BiVO_4$ at the thermodynamic equilibrium condition. The single-phase zone in the stability triangle is marked by the shaded area. The boundaries of the secondary binary phases that may occur with $BiVO_4$ are marked by the line as marked in the figure.

Nb_2O_5, the chemical potential of Nb, μ_{Nb} was taken to be −7.083eV. We observed the following from figure 3: (i) Most probable defect/impurity at all conditions is Nb substitutions at both Bi- and V-sites, where in oxygen-rich condition impurity concentrations are higher. (ii) Comparing Nb substitution at V-sites to Bi-sites, V-sites are more probable. (iii) Nb at V-sites with the presence of an oxygen vacancy has higher formation energy than Nb at V-sites by itself. (iv) Nb at Bi sites with the presence of an oxygen vacancy has small positive formation energy values throughout the region except at *D* point; the reason being *D* is the Bi-poorest point among these five points (*A, B, C, D, E*) which bound the stability zone of $BiVO_4$.

Note, it is quite apparent from the Figure 3 that among all the impurities considered here, "Nb substitution at V-site" containing impurities are more favorable to occur. At oxygen-rich condition, at point *E*, the formation energy of Nb at V-site is about 10 eV lower than Nb at Bi-site. Inferring from the formation energies from figure 3, Nb atoms will substitute both the V and

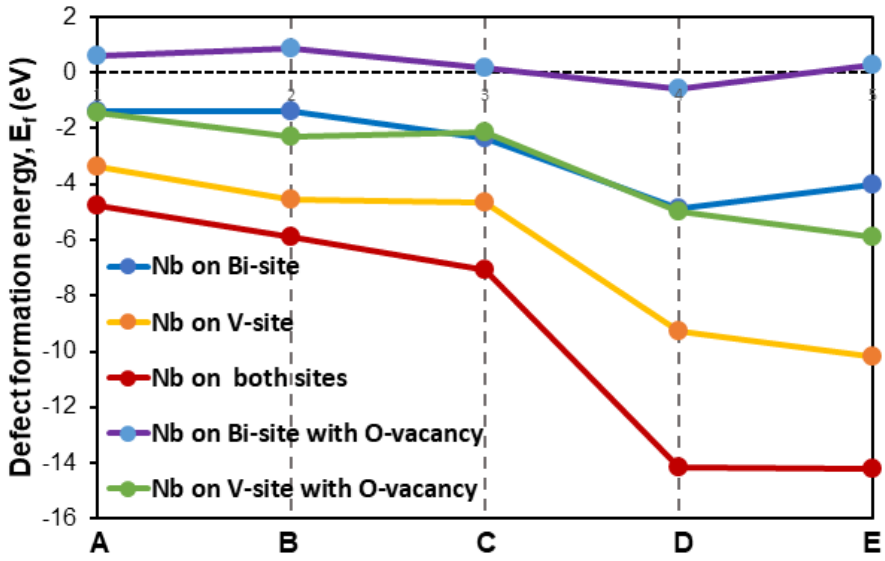

Figure-4. 3: Defect formation energies with respect to the chemical potentials given at points A-E of the single-phase stability zone in the chemical potential triangle as shown in figure 2. Point A represents the O-poor growth condition and point D and E represent O-rich growth condition.

Bi atoms of $BiVO_4$, with a much higher concentration of Nb at V sites. In general, all the metal impurities are highly likely to form at the O-rich condition. With the presence of oxygen vacancy, Nb atom impurity at V-sites, combined (defect+impurity) formation energies are negative throughout the chemical-potential ranges considered here, as shown in Figure 3. So, with the presence of a metal impurity, it is likely that oxygen vacancy will form along with a metal impurity substitution.

4. 5. Electronic structure of pristine bismuth vanadate

The calculated band structure of pristine bismuth vanadate as shown in Figure 4(a) is very similar to the other calculations[14,34,36]. So, we will briefly summarize our calculated electronic structure of $BiVO_4$. We define the Fermi level as the highest occupied state. The calculated indirect band gap of $BiVO_4$ is about 2.10 eV, which is (0.30–0.40 eV) smaller than the experimental result (2.40–2.50 eV)[2,3,7,41]. The band gap under-estimation is a well-known

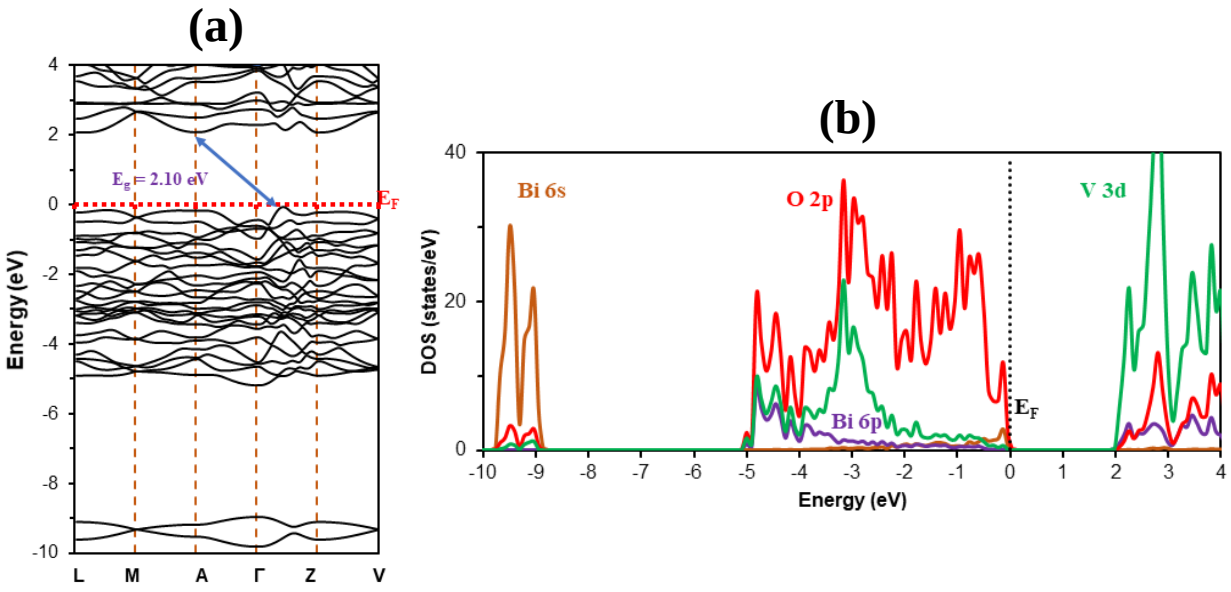

Figure-4. 4: (a) Band structure and (b) partial density of states (PDOS) of pristine $BiVO_4$.

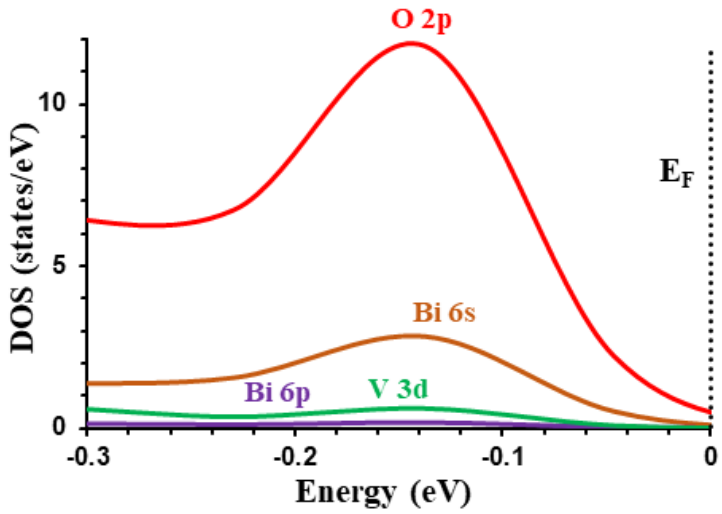

Figure-4. 5: Partial density of states (PDOS) near the Fermi level of pristine $BiVO_4$.

limitation of DFT-GGA for systems with localized d and f electrons[42–45]. Few theoretical studies reported that $BiVO_4$ has a direct band gap and their calculated band gap is 2.16 eV[34] and 2.06 eV[14]. Another theoretical study[36] reported that it has an indirect band gap and their calculated band gap is 2.17 eV. So, the calculated band gap in this present study has proximity to the other calculated results as well.

For a deeper look at the electronic states, the partial density of states (pDOS) for $BiVO_4$ is presented in Figure 4(b). It shows the similar features as reported other theoretical studies[14,34,36,41,46]. The width of the valence band is about 5.2 eV with respect to the highest occupied state. The O 2p contribution is the dominant just below the Fermi level up to -2.78 eV. From -2.78 eV to -5.2 eV the V 3d is the dominant band. Within this range, the hybridization among the V 3d and O 2p is prominent. The Bi 6p also takes part in the hybridization process along with the V 3d and O 2p orbitals from -3.86 eV up to 5.2 eV. The Bi 6s lone pair is located around -9.0 eV to -10.0 eV below the Fermi level. Although Bi 6s lone pair is very localized at this position, it also contributes at the top of the valence band as an anti-bonding orbital. Closer inspection at the very top of the valence band shows that Bi 6s located at the top of the valence band hybridized with O 2p orbital and to a lesser extent with V 3d bands, as shown in figure 5. The same feature is observed for Bi_2O_3 in which coupling between O 2p and Bi 6s produces antibonding Bi 6s states at the very top of the valence band[47]. The coupling of Bi 6s and O 2p orbitals in $BiVO_4$ is justified by the reported excitation and emission spectra[3]. Presence of antibonding cation-anion states at the top of the valence band facilitates the creation and conduction of charge carriers which is reported for Cu_2O[48] and SnO[49]. For the conduction band, the dominant contribution comes mainly from the localized V 3d orbitals; O 2p and Bi 6p contribute to the conduction band as well.

4. 6. Electronic structure of Nb-doped bismuth vanadate

The drawbacks of pristine $BiVO_4$ as a photo-catalyst, such as poor photo-induced charge carrier transports, may be overcome by doping $BiVO_4$ intrinsically or extrinsically. Yin *et. al.*[14] have reported their theoretical calculation of doping of Sr, Ca, K, Na atoms on Bi-site and Mo, W on V-site. Zhao *et. al.*[16] have also reported their theoretical calculation of transition metals (Ti, Cr,

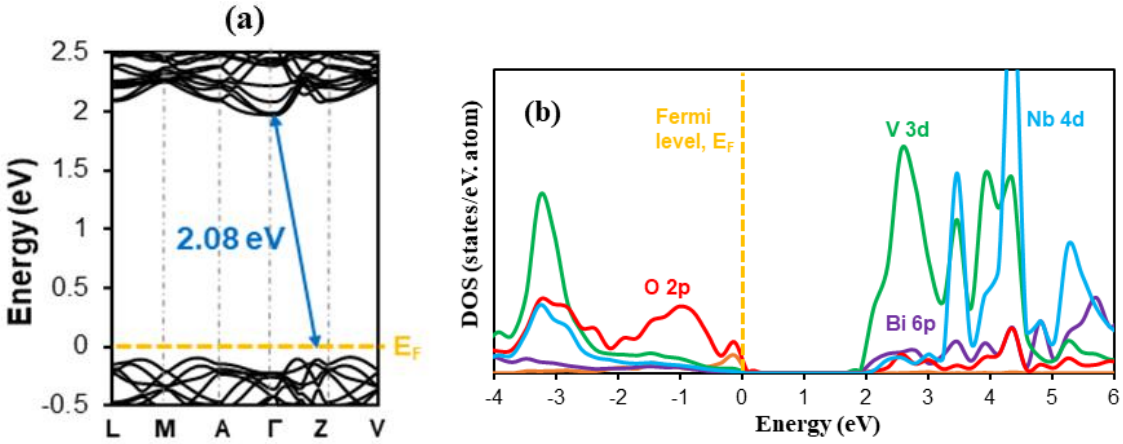

Figure-4. 6: (a) Band structure and (b) partial density of states (PDOS) of $BiVO_4$ with Nb doping on V-site.

Zr, Nb, Mo and W) doping on V-site of $BiVO_4$. Luo *et. al.*[17] have reported the improvement of optical absorption in the visible light region by doping $BiVO_4$ with Mo, W and Sn atoms on V-site and Bi-site. Sameera *et. al.*[18] have reported the structural and optical properties of Nb-doped $BiVO_4$ with experimental techniques like XRD, Raman spectroscopy, SEM, and TEM. They have reported the optical as well as photo-current enhancement of $BiVO_4$ with Nb doping on V-site. In this present study, we have studied the electronic structure of $BiVO_4$ with niobium (Nb) doping on Bi-site, V-site and on both (Bi and V) sites along with oxygen vacancies simultaneously in a systematic way to elucidate their electronic properties and to predict thermodynamic conditions to synthesize the desired doped/alloyed materials. Also, as indicated in the introduction, as pressure improves BiO_8 polyhedra symmetry, we'll also report our study on these systems, their electronic properties, stabilities, and synthesizability when pressure is applied.

The doping of Nb on V-site modify the electronic structure of pristine $BiVO_4$ as shown in Figure 6(a-b). The position of the minima of the conduction band of pristine $BiVO_4$ is at point A,

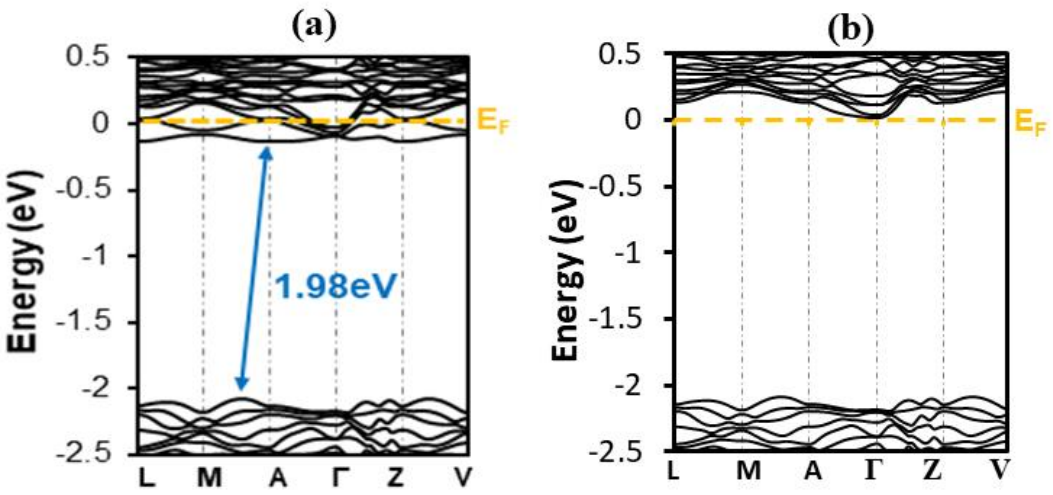

Figure-4. 7: Spin polarized band structure of $BiVO_4$ with Nb doping at Bi site: (a-upper panel) shows spin up and (b-lower panel) shows spin down band structure.

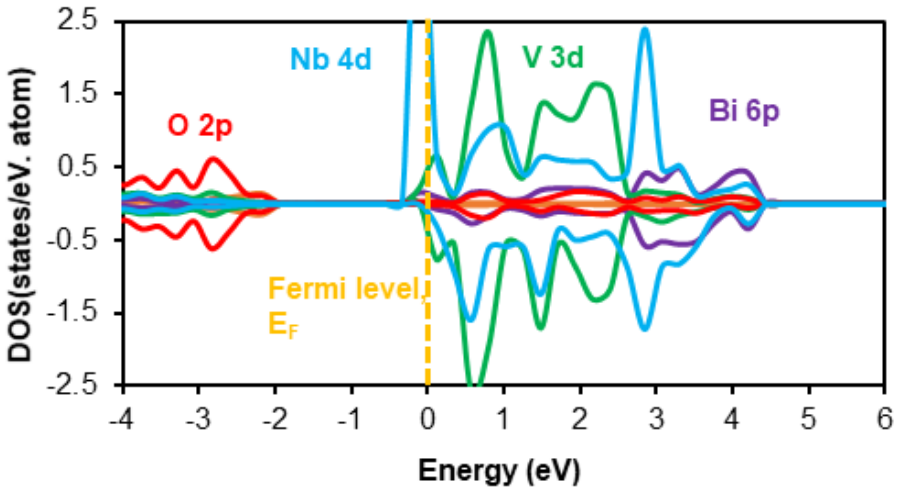

Figure-4. 8: Partial density of states (PDOS) of $BiVO_4$ with Nb doping at Bi site.

as shown in figure 4(a), which is away from the center of the Brillouin zone. Due to the Nb doping on V-site, the position of the conduction band minima has shifted to Γ point as shown in figure 6(a) and the position of the valence band maxima remains unchanged which is in between Γ and Z points. So, due to Nb doping on V-site, it shows a trend to become a direct band gap. Nb doping on V-site also reduces the band gap slightly to 2.08 eV which is 0.02 eV lower than the

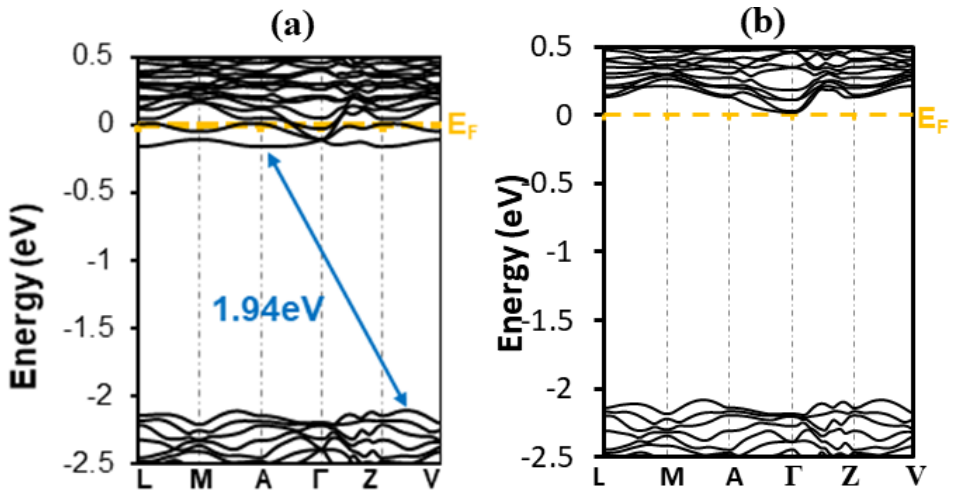

Figure-4. 9: Spin polarized band structure of $BiVO_4$ with Nb doping at both V- and Bi-site: (a-upper panel) shows spin up and (b-lower panel) shows spin down band structure.

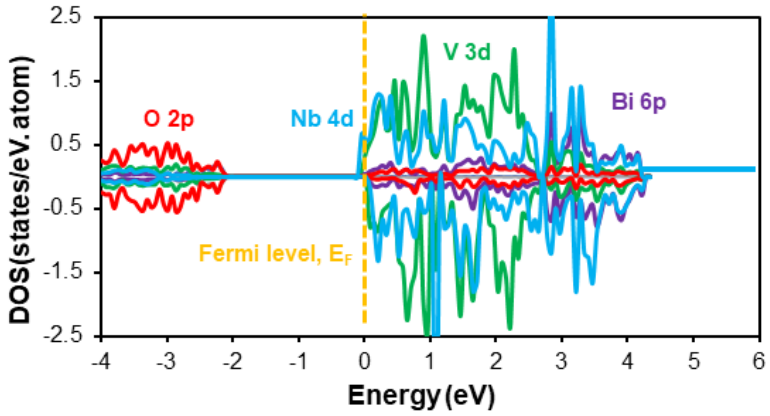

Figure-4. 10: Partial density of states (PDOS) of $BiVO_4$ with Nb doping at both V and Bi-site.

pristine band gap (2.10 eV), which also supported by the experimental finding[15]. Also, note the minimum direct band gap for Nb-doped $BiVO_4$ is 2.15 eV, compared to that of 2.18 eV for pristine $BiVO_4$. The band gap reduction, as well as the tendency to make the band gap direct, are the favorable conditions for efficient solar energy absorption. As shown in the partial density of state plot of pristine $BiVO_4$, figure 4(b), the width of the peak of O 2p orbital at the top of the valence band and V 3d orbital at the bottom of the conduction band of pristine $BiVO_4$ are 1.71 eV and 0.93 eV respectively. Due to the Nb doping on V-site, the width of the peak at the top of valence and bottom of the conduction band in the partial density of states plot become 2.13 eV

and 1.57 eV respectively, as shown in figure 6(b). So, Nb doping on V-site makes the peak near to the top of the valence and bottom of the conduction band wider than the pristine $BiVO_4$. These wider bands near band edges indicate that the top of valence bands and bottom of conduction bands would be more dispersive than the pristine bands, and which eventually make the transport of photo-generated charge carrier easier. The effective mass of charge carriers will reflect this fact, which we will discuss later in this paper.

Now we turn our focus on the Nb substitution at a Bi site in $BiVO_4$. Even though Nb atoms at Bi-sites are less probable, formation energies are negative. So there are possibilities that Nb can occupy Bi sites as well. Due to Nb doping on Bi-site, the relaxed supercell has a total of $2\mu_B$ magnetic moment. So here we have reported both spins up and down band structures (Figure 7) and pDOS plots (Figure 8). For the spin up band structure in Figure 7, there are some partially occupied bands at the lower part of the conduction band. The position of the bottom of the conduction band minima remains unchanged with respect to the pristine $BiVO_4$, but the top of the valence band maxima changed to a point in between A to M. The band gap reduces to 1.98 eV, which is 0.12 eV lower than the pristine $BiVO_4$ band gap. For the spin down case, there are no occupied bands in the conduction bands. Due to the Nb doping on Bi-site, V 3d bands at the bottom of the conduction band get replaced by Nb 4d bands as expected. As shown in the partial density of states plot in figure 8, the partially filled band at the bottom of the conduction band for up-spin is due to Nb 4d bands; also the top of the valence band is mostly O 2p, and there is a significant amount of hybridization between O 2p and Bi 6s orbitals below the Fermi level. So the replacement of localized V 3d band by less localized Nb 4d bands and creation of partially filled bands at the bottom of the conduction band may attribute to easier photo-generated carrier transport and hence improve the photocatalytic activity of $BiVO_4$.

Simultaneous doping of Nb on both Bi and V-sites changes the electronic structure of $BiVO_4$ in a similar manner as Nb doping on Bi-site as shown in figures 9 and 10. Here also the relaxed supercell has a total of $2\mu_B$ magnetic moment. The lower part of the conduction band is also showing partially filled bands. The position of the valence band maxima changed to a point in between symmetry points Z and V, whereas it was somewhere between Γ and Z point for pristine $BiVO_4$ and the position of conduction band minima remains unchanged. It reduces the band gap to 1.94 eV which is 0.16 eV lower than the pristine band gap. From the partial density of states plot, as shown in figure 10, the dominant contribution to the top of the valence band remains the same as was in the pristine $BiVO_4$. On the other hand, the bottom of the conduction band composed of Nb 4d and V 3d bands; the spin-up DOS shows V 3d and Nb 4d are partially occupied with V 3d has little more contribution. On the other hand, spin-down DOS shows they both have similar contributions at the bottom of the conduction band with no occupation. Earlier we have seen that Nb-doping at Bi-site can create this kind of occupied states. We would like to mention here again, that for the individual 'Nb at Vi-site' doping, the band gap reduction was only 0.02eV. For 'Nb at Bi-site' and 'Nb at both Bi and V-sites' the band gap reduction was 0.12eV and 0.16 eV respectively.

The main motivation for Nb doping is that its 4d band would contribute to the $BiVO_4$'s conduction band minima, and thereby would make the conduction bands more dispersive and lower the electron effective masses. It should be mentioned here, that the main mechanism for conduction in $BiVO_4$ is polaron conduction[50]. However, band dispersion can still play a role especially when the band dispersion can be increased by impurity incorporation. The effective mass calculations can provide a quantitative measure for the band edge dispersion changes as well as a qualitative measure of the polaron's nature. Lower effective masses are indicative to

larger polarons. We have calculated the electron effective mass to see whether Nb doping in $BiVO_4$ reduces the electron effective mass. We have indeed observed the reduction of electron effective mass due to Nb doping. The calculated effective mass of electron for pristine $BiVO_4$ is 2.05 m_e, where m_e is the electron's rest mass. Now, doping 'Nb at V-site', 'Nb at Bi-site' and 'Nb at both-sites' $BiVO_4$ have electron effective masses of 1.64 m_e, 1.84 m_e and 1.78 m_e respectively. So, the reduction of electron effective mass will help improve the transport property and hence improve the photo-current by transforming the polaron into large polaron. Higher effective masses are indicative of small polarons[51]. Also, the self-trapped carrier's radius is inversely proportional to the carrier's effective mass. Interestingly, Nb doping also would improve the polaron conduction from another point of view, as the Nb doping at Bi sites decreased the overall volume of the cell by 1.5%. Reduction of the volume implies reduced hopping distances for the electrons which potentially would improve polaron conduction.

4. 7. Structural changes of $BiVO_4$ due to Nb doping

The monoclinic phase of $BiVO_4$ is the most photocatalytically active than the other two phases, i.e., orthorhombic and tetragonal. Here we will discuss the structural changes of monoclinic $BiVO_4$ due to the Nb doping on V-site, Nb doping on Bi-site and Nb doping on both cationic sites simultaneously. The calculated results are shown in table 3. The lattice constants *a* and *b* of Nb-doped (on V-site) $BiVO_4$ remains almost the same as the pristine $BiVO_4$ except for the lattice constant *c*. The lattice constant *c* increased (10.3629 Å) with compared to the pristine lattice constant *c* (10.3231 Å) and hence increase the overall volume of the supercell from 1254.234 $Å^3$ (pristine supercell volume) to 1259.450 $Å^3$ (Nb-doped on V-site cell volume). Nb doping on Bi-site changes the lattice constants as well. The lattice constants became smaller than the pristine $BiVO_4$ lattice constants and hence decrease the overall supercell volume from

1254.234 $Å^3$ (pristine supercell volume) to 1235.466 $Å^3$(Nb-doped on Bi-site cell volume). And the simultaneous doping of Nb on both cationic sites decreases all the lattice constants, and as a result, the supercell volume of the Nb-doped $BiVO_4$ on both sites reduce to 1239.4308 $Å^3$. Changing of cell volume due to Nb doping in $BiVO_4$ has a direct impact on the distortion of BiO_8 and VO_4 polyhedra.

Nb-doping in $BiVO_4$ changes the bond lengths of the BiO_8 dodecahedron and VO_4 tetrahedron. In pristine $BiVO_4$, the BiO_8 dodecahedron has four pairs of Bi-O bonds (2 × 2.498 Å, 2 × 2.496 Å, 2 × 2.447 Å and 2 × 2.444 Å) and VO_4 tetrahedron has two pairs of V-O bonds (2 ×1.745 Å and 2 × 1.744 Å). The calculated as well as other experimental and theoretical bond lengths of Bi-O and V-O bond lengths of pristine $BiVO_4$ are presented in table 2. There are eight distinct Bi-O bonds and four distinct V-O bonds within the BiO_8 dodecahedron and VO_4 tetrahedron respectively when Nb is doped on V-site, Bi-site and both cationic sites of $BiVO_4$ and the calculated Bi-O and V-O bond lengths are presented in table 4. So, it is clear that Nb doping in $BiVO_4$ breaks the pairwise bonding nature of Bi-O and V-O bonds of pristine $BiVO_4$ and the Bi and V polyhedra get more distorted as compared to that of the pristine case.

The distortion of BiO_8 dodecahedron has an important role to play in improving the photocatalytic property of $BiVO_4$ photo-catalyst[9,18,20]. Nb doping on $BiVO_4$ increases the distortion within the BiO_8 dodecahedron near the Nb doping site. To study this distortion and to control it, we studied the bond distortion index. The bond length distortion index, D[52] is defined by the following equation:

$$D = \frac{1}{n}\sum_i^n \frac{|l_i - l_{avg}|}{l_{avg}},$$

where, l_i is the bond length from the central atom to the ith coordinating atom, and l_{avg} is the average bond length from the central atom within the polyhedra. The bond length distortion

index, *D* of BiO_8 dodecahedron for pristine, Nb-doped $BiVO_4$ (Nb on V-site), Nb-doped $BiVO_4$ (Nb on Bi-site) and Nb-doped $BiVO_4$ (Nb on both cationic sites) are 0.01039, 0.01747, 0.02126 and 0.01745 respectively. So it shows that the BiO_8 dodecahedron gets more distorted due to Nb doping.

Table-4. 3: Lattice parameters of pristine $BiVO_4$ supercell, Nb dopped $BiVO_4$ (Nb on V - site) supercell, Nb doped $BiVO_4$ (Nb on Bi – site) supercell and Nb doped $BiVO_4$ (Nb on both Bi – site and V - site) supercell.

	Pristine $BiVO_4$	**$BiVO_4$ with Nb doping on V – site**	**$BiVO_4$ with Nb doping on Bi - site**	**$BiVO_4$ with Nb doping on both Bi and V – site**
Crystal structure	Base centered monoclinic	Base centered monoclinic	Base centered monoclinic	Base centered monoclinic
a (Å)	13.832	13.834	13.766	13.753
b (Å)	13.832	13.834	13.766	13.753
c (Å)	10.323	10.362	10.275	10.311
α (º)	68.116	67.987	68.100	67.973
β (º)	68.1166	67.987	68.100	67973
γ (º)	116.275	116.026	116.277	115.968
Cell volume ($Å^3$)	1254.233	1259.449	1235.466	1239.430

Table-4. 4: Bi-O and V-O bond length of BiO_8 and VO_4 polyhedron of Nb doped $BiVO_4$.

Pristine $BiVO_4$		**$BiVO_4$ with Nb doping on V-site**		**$BiVO_4$ with Nb doping on Bi-site**		**$BiVO_4$ with Nb doping on both cationic sites**	
Bi-O/ Å	**V-O/Å**	**Bi-O/ Å**	**V-O/Å**	**Bi-O/ Å**	**V-O/Å**	**Bi-O/ Å**	**V-O/Å**
2.444 (2 pairs)	1.745 (2 pairs)	2.3846	1.7457	2.4084	1.7385	2.4089	1.7344
		2.4223		2.4222		2.4091	
2.447 (2 pairs)		2.4306	1.7491	2.4252	1.7391	2.4425	1.7400
		2.4735		2.4268		2.4483	
2.498 (2 pairs)	1.744 (2 pairs)	2.4949	1.7418	2.4604	1.7419	2.4661	1.7454
		2.5010		2.4693		2.4804	
2.496 (2 pairs)		2.5144	1.7510	2.5090	1.7760	2.4816	1.7762
		2.5392		2.6419		2.6188	

4. 8. Effect of external pressure on the local structure of BiO_8 dodecahedron

A recent study[20] reported that less distortion of BiO_8 dodecahedron of monoclinic $BiVO_4$ near to the doping site could facilitate the enhancement of photocatalytic activity. In the present study, even though Nb doping reduces effective mass of the electrons, it also increased the distortions

in the BiO_8 polyhedra. One way to reduce the distortion within the BiO_8 dodecahedron is to apply external pressure. I. G. Wood *et. al.*[24] reported the pressure induced reduction of distortion

Table-4. 5: Bond length distortion index of BiO_8 dodecahedron

	Pristine $BiVO_4$ (Tetragonal)	**Pristine $BiVO_4$ (Monoclinic)**	**$BiVO_4$: Nb_V**	**$BiVO_4$: Nb_{Bi}**	**$BiVO_4$: $Nb_{Bi/V}$**
Pressure (GPa)	**Bond length distortion index, D of BiO_8**	**Bond length distortion index, D of BiO_8**	**Bond length distortion index, D of BiO_8**	**Bond length distortion index, D of BiO_8**	**Bond length distortion index, D of BiO_8**
0	0.01068	0.01039	0.01747	0.02126	0.01745
4		0.00834	0.01450	0.01703	0.01420
8		0.00662	0.01274	0.01436	0.01260
12		0.00560	0.01157	0.01204	0.01154
16		0.00483	0.01080	0.01093	0.01087

of BiO_8 dodecahedron. Hence, here we have studied the impact of external pressure on the distortion of BiO_8 dodecahedron. We have studied the change of distortion of BiO_8 dodecahedron up to 16 GPa pressure. We have noticed that applying external pressure could reduce the distortion of BiO_8 dodecahedron near the Nb doping site. The bond length distortion index, *D* of BiO_8 dodecahedron for pristine monoclinic and tetragonal $BiVO_4$ are 0.01039 and 0.01068.

After applying 16 GPa external pressure, the bond length distortion index, *D* of BiO_8 dodecahedron for Nb-doped $BiVO_4$ (Nb on V-site), Nb-doped $BiVO_4$ (Nb on Bi-site) and Nb-

Table-4. 6: Electron effective masses in Nb doped BiVO4 with and without 16GPa pressure.

System	Effective mass (m_e) without 16 GPa pressure	Effective mass (m_e) with 16 GPa pressure
Pristine $BiVO_4$	2.05	
Nb_V: $BiVO_4$	1.64	1.49
Nb_{Bi}: $BiVO_4$	1.84	1.60
$Nb_{Bi,V}$: $BiVO_4$	1.78	1.56

doped $BiVO_4$ (Nb on both cationic sites) becomes 0.01080, 0.01093 and 0.01087 respectively. The bond length distortion index, *D* of BiO_8 dodecahedron after applying 16 GPa external pressure become very similar to the distortion index as pristine tetragonal and monoclinic phase BiO_8 dodecahedron. So, the external pressure reduces the distortion and transform the BiO_8 dodecahedron into the more symmetric structure. The distortion index of BiO_8 dodecahedron for different applied external pressure is shown in Table 5. A similar calculation with the VO_4 tetrahedron showed very small distortions. For example, for pristine monoclinic $BiVO_4$ the distortion index is 0.00051, and with Nb doping at V site it is 0.00196 at 0 GPa. At 16 GPa these indices became 0.00001 and 0.00066, respectively. Here also external pressure reduced the distortions.

So, pressure induced symmetric polyhedra in $BiVO_4$ would create more disperse band at the conduction band minima and reduce the effective mass of the electrons. In fact, the electron effective masses have reduced significantly. The calculated effective mass of electron after applying 16 GPa external pressure are 1.49 m_e, 1.60 m_e and 1.56 m_e for Nb-doped on V-site, Nb-doped on Bi-site and Nb-doped on both cationic sites respectively. Table 6 shows the electron

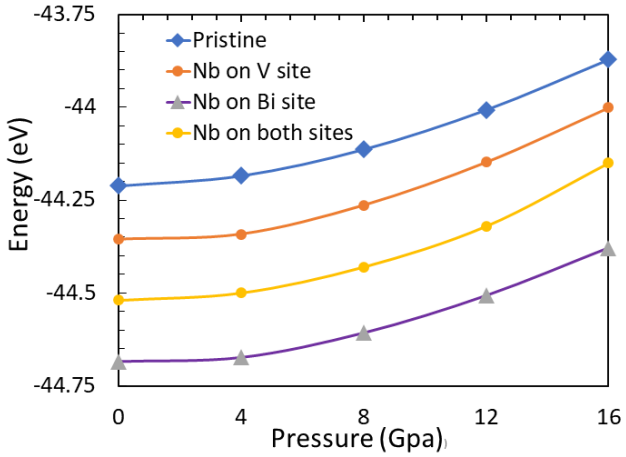

Figure-4. 11: Relative stability of pristine and Nb-doped $BiVO_4$ phases after applying external pressure.

effective mass of Nb-doped $BiVO_4$ without and with 16 GPa external pressure. It shows that pressure-induced symmetrization of BiO_8 dodecahedron could help to improve the photo-catalytic property of $BiVO_4$ photo-catalyst by reducing the electron effective mass.

The band structures of $BiVO_4$ with different pressures are provided in the supplemental information (Figure S1(a)-(d)). The band structures were aligned with respect to the deep O 1s level (set to 0 eV). Key observations are: (i) band gap decreases with increasing pressure, 2.10 eV to 1.78 eV from 0 GPa to 16 GPa; (ii) as the pressure increased from 0 to 16 GPa, overall the VBM was lowered by 0.9 eV; (iii) the localized Bi lone-pair s-bands below 490 eV became wider with pressure (see table S1 in SI). Consequently, their anti-bonding counterpart, bands at the top of the valence band were more dispersive, as well, at high pressure. The first two changes are mostly linear with respect to the pressure (see Figure S2(a) to (f)). The third one would be helpful for generating large hole polaron for better conductivity.

4. 9. Impact of pressure on single phase stability zone of $BiVO_4$ in the chemical-potential landscape

The secondary binary oxide phases (VO_2, V_2O_3, V_2O_5, Bi_2O_3, and Nb_2O_5) may appear within the $BiVO_4$ phase during the synthesis process. These impurity phases would negatively impact the photo-catalytic properties of $BiVO_4$ photo-catalyst. Therefore, synthesizing a single phase $BiVO_4$ is important for the better photo-catalytic property. We have calculated the area of single phase stability zone of $BiVO_4$ within the chemical potential landscape without external pressure as shown in Figure 2. It gives an area of 0.86 eV^2 for a single phase $BiVO_4$ within the chemical potential landscape. We have also studied the impact of external pressure on the single-phase stability zone of $BiVO_4$. Supporting information Figures S3 (a-e) show the single-phase stability zones of $BiVO_4$ within the chemical-potential landscape for 0, 4, 8, 12 and 16 GPa, respectively. The following equations define the bounded area of these various chemical potential triangles:

For zero pressure: $\Delta\mu_{Bi} + \Delta\mu_V + 4\Delta\mu_O = -14.3946eV$

For 4 GPa pressure: $\Delta\mu_{Bi} + \Delta\mu_V + 4\Delta\mu_O = -14.3677eV$

For 8 GPa pressure: $\Delta\mu_{Bi} + \Delta\mu_V + 4\Delta\mu_O = -14.2964eV$

For 12 GPa pressure: $\Delta\mu_{Bi} + \Delta\mu_V + 4\Delta\mu_O = -14.1894eV$

For 16 GPa pressure: $\Delta\mu_{Bi} + \Delta\mu_V + 4\Delta\mu_O = -14.0536eV$

To avoid the formation of the binary secondary phases following constraints were also considered for each respective pressure:

$$2\Delta\mu_{Bi} + 3\Delta\mu_O < \Delta H_f(Bi_2O_3),$$

$$2\Delta\mu_V + 5\Delta\mu_O < \Delta H_f(V_2O_5),$$

$$\Delta\mu_V + 2\Delta\mu_O < \Delta H_f(VO_2),$$

$$2\Delta\mu_V + 3\Delta\mu_O < \Delta H_f(V_2O_3).$$

The shaded area within the triangle represents the single-phase region of $BiVO_4$. The calculated results are presented in table 7. These results showed that single phase region of $BiVO_4$ could be

Table-4. 7: Area of the single phase stability zone of $BiVO_4$ within the chemical ptential landscape.

Pressure (GPa)	**Single phase area of $BiVO_4$ (eV^2)**	**Boundary of the chemical potential triangle (eV)**
0	0.860	$-14.3946 \leq \Delta\mu_{Bi} \leq 0$ $-14.3946 \leq \Delta\mu_V \leq 0$
4	0.884	$-14.3677 \leq \Delta\mu_{Bi} \leq 0$ $-14.3677 \leq \Delta\mu_V \leq 0$
8	0.889	$-14.2964 \leq \Delta\mu_{Bi} \leq 0$ $-14.2964 \leq \Delta\mu_V \leq 0$
12	0.905	$-14.1894 \leq \Delta\mu_{Bi} \leq 0$ $-14.1894 \leq \Delta\mu_V \leq 0$
16	0.918	$-14.0536 \leq \Delta\mu_{Bi} \leq 0$ $-14.0536 \leq \Delta\mu_V \leq 0$

increased by applying external pressure while synthesizing Nb-doped $BiVO_4$. It should be noted that the Bi_2O_3 secondary phase gets separated prominently than the other secondary oxide binary phases from the $BiVO_4$ phase upon applying external pressure. So, applying external pressure while synthesizing could be a good strategic route to synthesis Nb-doped $BiVO_4$ photo-catalyst.

As compared to the unpressurized phases, pressurized synthesis of Nb-doped $BiVO_4$ phases give less distortion within the BiO_8 dodecahedron and hence reducing the electron

effective mass by creating more disperse band at the conduction band minima and has the potential to improve the photo-catalytic property. Furthermore, the single-phase stability zone of $BiVO_4$ within the chemical potential landscape become larger upon applying external pressure. From the above discussions, it can be argued that the synthesis of Nb-doped $BiVO_4$ at high-pressured environment can produce high-efficient solar-absorber and photo-catalyst materials. Such high-pressure synthesis environment can be achievable via a diamond anvil cell (DAC) synthesis process[53]. Other oxides materials have also been synthesized by DAC method[54–56]

Conclusions

We have presented here DFT study of Nb-doped $BiVO_4$. Nb was doped on both Bi and V sites. From the results, it can be concluded that Nb substitution at both sites simultaneously was the most energetically favorable according to our present study. This doping strategy introduces charge carriers at the bottom of the conduction band composed of Nb 4d band. If conduction band position does not change, this would be a better doping strategy in $BiVO_4$. The combined Nb substations at both Bi and V-sites decreased the gap by 0.16 eV. The Nb 4d band is more dispersive than the V 3d band, so incorporations of Nb lower the effective mass of the electron significantly. On the other hand, Nb on V-site-only substitution did not decrease the band gap much, only by 0.02eV. However, the band gap reduction of $BiVO_4$ due to doping at Bi-site-only was by 0.12 eV. Reduction of effective masses due to these doping strategies indicate better polaron conduction compared to the pristine $BiVO_4$. To this end, we also considered the effect of external pressure on the $BiVO_4$. Distortion reduction of BiO_8 dodecahedron near the doping site, further reduction of effective masses and area increment of the single-phase region of $BiVO_4$ under pressure suggests a good strategic rout of synthesizing single phase $BiVO_4$ for efficient photo-catalysis.

Acknowledgments

P.M.R. and M.N.H. were supported by National Science Foundation award no. DMR-1609538 and DMR-1609811, respectively.

Conflict of Interest:

The authors declare no conflict of interest.

Keywords:

$BiVO_4$, Density Functional Theory (DFT), H_2 production, Photo-catalyst, Polaron conduction

References:

[1] L. Zhou, Y. Yang, J. Zhang, P. M. Rao, ACS Appl. Mater. Interfaces **9**, 11356–11362 (2017).

[2] F. F. Abdi, L. Han, A. H. M. Smets, M. Zeman, B. Dam, R. Van De Krol, Nat. Commun. **4**, 1-7 (2013).

[3] A. Kudo, K. Omori, H. Kato, J. Am. Chem. Soc. **121**, 11459–11467 (1999).

[4] S. Hernández, G. Barbero, G. Saracco, A. L. Alexe-Ionescu, J. Phys. Chem. C **119**, 9916–9925 (2015).

[5] Y. Park, K. J. McDonald, K. S. Choi, Chem. Soc. Rev. **42**, 2321–2337 (2013).

[6] C. Regmi, Y. K. Kshetri, S. K. Ray, R. P. Pandey, S. W. Lee, Appl. Surf. Sci. **392**, 61-70 (2017).

[7] M. V. Malashchonak, E. A. Streltsov, D. A. Kuliomin, A. I. Kulak, A. V. Mazanik, Mater. Chem. Phys. **201**, 189–193 (2017).

[8] D. J. Payne, M. D. M. Robinson, R. G. Egdell, A. Walsh, J. McNulty, K. E. Smith, L. F. J. Piper, Appl. Phys. Lett. **98**, 1–4 (2011).

[9] S. Tokunaga, H. Kato, A. Kudo, Chem. Mater. **13**, 4624–4628 (2001).

[10] L. Zhou, C. Zhao, B. Giri, P. Allen, X. Xu, H. Joshi, Y. Fan, L. V. Titova, P. M. Rao, Nano Lett. **16**, 3463–3474 (2016).

[11] P. M. Rao, L. Cai, C. Liu, I. S. Cho, C. H. Lee, J. M. Weisse, P. Yang, X. Zheng, Nano Lett. **14**, 1099–1105 (2014).

[12] H. S. Park, K. E. Kweon, H. Ye, E. Paek, G. S. Hwang, A. J. Bard, J. Phys. Chem. C **115**, 17870–17879 (2011).

[13] D. K. Zhong, S. Choi, D. R. Gamelin, J. Am. Chem. Soc. **133**, 18370–18377 (2011).

[14] W. Yin, S. Wei, M. M. Al-jassim, J. Turner, Y. Yan, Phys. Rev. B **155102**, 1–11 (2011).

[15] O. Monfort, S. Sfaelou, L. Satrapinskyy, T. Plecenik, T. Roch, G. Plesch, P. Lianos, Catal. Today **280**, 51–57 (2017).

[16] Z. Zhao, W. Luo, Z. Li, Z. Zou, Phys. Lett. A **374**, 4919–4927 (2010).

[17] W. Luo, J. Wang, X. Zhao, Z. Zhao, Z. Li, Z. Zou, Phys. Chem. Chem. Phys. **15**, 1006–1013 (2013).

[18] S. S. Fathimah, P. P. Rao, V. James, A. K. V Raj, G. R. Chitradevi, S. Leela, Dalton Trans. **43**, 15851 (2014).

[19] D. S. Khaerudini, G. Guan, P. Zhang, A. Abudula, Ionics **22**, 93–97 (2016).

[20] B. Pattengale, J. Ludwig, J. Huang, J. Phys. Chem. C. **120**, 1421–1427 (2016).

[21] W. J. Jo, H. J. Kang, K.-J. Kong, Y.S. Lee, H. Park, Y. Lee, T. Buonassisi, K.K. Gleason, J.S. Lee, Proc. Natl. Acad. Sci. **112**, 13774–13778 (2015).

[22] C. L. Mayfield, M. N. Huda, J. Cryst. Growth **444**, 46–54 (2016).

[23] C. L. Mayfield, V. Subramanian, M. N. Huda, J. Phys. Condens. Matter. **27**, 315502 (2015).

[24] I. G. Wood, B. Welber, W. I. F. David, A. M. Glazer, J. Appl. Crystallogr. **13**, 224–229 (1980).

[25] P. Hohenberg, W. Kohn, Phys. Rev. B **7**, 1912–1919 (1973).

[26] W. Kohn, L. J. Sham, Phys. Rev. **140**, 1133 – 1138 (1965).

[27] G. Kresse, J. Furthmüller, Comput. Mater. Sci. **6**, 15–50 (1996).

[28] G. Kresse, J. Furthmüller, Phys. Rev. B - Condens. Matter Mater. Phys. **54**, 11169–11186 (1996).

[29] J. P. Perdew, K. Burke, M. Ernzerhof, Phys. Rev. Lett. **77**, 3865–3868 (1996).

[30] P. E. Blöchl, Phys. Rev. B **50**, 17953–17979 (1994).

[31] K. E. Kyoung, G. S. Hwang, Phys. Rev. B **86**, 165209 (2012).

[32] J. Zhang, M. Deng, F. Ren, Y. Wu, Y. Wang, RSC Adv. **6**, 12290 (2016).

[33] K. Momma, F. Izumi, J. Appl. Crystallogr. **44**, 1272–1276 (2011).

[34] A. Walsh, Y. Yan, M. N. Huda, M. M. Al-Jassim, S. H. Wei, Chem. Mater. **21**, 547–551 (2009).

[35] A.W. Sleight, H. Chen, A. Ferretti, D. E. Cox, Mater. Res. Bull. **14**, 1571–1581, (1979).

[36] Z. Zhao, Z. Li, Z. Zou, Phys. Chem. Chem. Phys. **13**, 4746 – 4753 (2011).

[37] P. Sarker, M. M. Al-Jassim, M. N. Huda, J. Appl. Phys. **117**, 035702 (2015).

[38] C. Persson, Y.J. Zhao, S. Lany, A. Zunger, Phys. Rev. B - Condens. Matter Mater. Phys. **72**, 1–14 (2005).

[39] A. Nagoya, R. Asahi, R. Wahl, G. Kresse, Phys. Rev. B - Condens. Matter Mater. Phys. **81**, 1–4 (2010).

[40] S. Zhang, S. H. Wei, A. Zunger, H. Katayama-Yoshida, Phys. Rev. B - Condens. Matter Mater. Phys. **57**, 9642–9656 (1998).

[41] J. K. Cooper, S. Gul, F. M. Toma, L. Chen, P. A. Glans, J. Guo, J. W. Ager, J. Yano, I. D. Sharp, Chem. Mater. **26**, 5365–5373 (2014).

[42] J. P. Perdew, M. Levy, Phys. Rev. Lett. **51**, 1884–1887 (1983).

[43] F. Zhou, C. A. Marianetti, M. Cococcioni, D. Morgan, G. Ceder, Phys. Rev. B - Condens. Matter Mater. Phys. **69**, 1– 4 (2004).

[44] V. I. Anisimov, J. Zaanen, O. K. Andersen, Phys. Rev. B **44**, 943 – 954 (1991).

[45] M. V. Ganduglia-Pirovano, A. Hofmann, J. Sauer, Surf. Sci. Rep. **62**, 219 –270 (2007).

[46] K. Ding, B. Chen, Z. Fang, Y. Zhang, Theor. Chem. Acc. **132**, 1–7 (2013).

[47] A. Walsh, G. W. Watson, D. J. Payne, R. G. Edgell, J. Guo, P.A. Glans, T. Learmonth, K. E. Smith, Phys. Rev. B **73**, 1–13 (2006).

[48] X. Nie, S. H. Wei, S. B. Zhang, Phys. Rev. Lett. **88**, 066405 (2002).

[49] Y. Ogo, H. Hiramatsu, K. Nomura, H. Yanagi, T. Kamiya, M. Hirano, H. Hosono, Appl. Phys. Lett. **93**, 032113 (2008).

[50] M. Ziwritsch, S. Müller, H. Hempel, T. Unold, F. F. Abdi, R. van de Krol, D. Friedrich, R. Eichberger, ACS Energy Lett. **1**, 888–894 (2016).

[51] A. J. E. Rettie, W. D. Chemelewski, D. Emin, C. B. Mullins, J. Phys. Chem. Lett. **7**, 471–479, (2016).

[52] W. H. Baur, Acta Crystallogr., Sect. B: Struc. Sci. **30**, 1195 (1974).

[53] A. Jayaraman, Rev. Mod. Phys. **55**, 65–108 (1983).

[54] B. Lavina, Y. Meng, Sci. Adv. **1**, 5 (2015).

[55] Y. Wenge, K. D. Young, Y. Liuxiang, L. Nana, T. Lingyun, A. Khalil, M. Ho-Kwang, Adv. Sci. **4**, 1600453, (2017).

[56] V. S. Bhadram, Q. Cheng, C.K. Chan, Y. Liu, S. Lany, K. Landskron, T.A. Strobel, ACS Appl. Energy Mater. **1**, 260–266 (2018).

Chapter 5

Slow carrier transport and photovoltage limitation in $BiVO_4$: Role of polaron

Hori Pada Sarker and Muhammad N. Huda[*]

Department of Physics, The University of Texas at Arlington

Arlington, Texas 76019, United States of America

Submitted for publication at:

Journal of Materials Chemistry A

[*] Corresponding author: huda@uta.edu

Abstract

$BiVO_4$ is one of the most studied absorber materials for photoelectrochemical (PEC) H_2O splitting due to its near ideal band gap and suitable band edge positions. Despite its high promise, $BiVO_4$ comes short in achieving the speculated expectation. The obtained photocurrent as well as solar to hydrogen (STH) conversion efficiency is far too low compared to theoretically predicted values. Recent experimental footprints indicate polaron formation as the key bottleneck for limited efficiency. However, atomistic mechanism of polaron mediated efficiency limitation in such ternary oxides is not well understood. In order to understand the electronic origin of polaron mediated performance limitations, we have studied polaron formation in $BiVO_4$ by using first principles density functional theory with Hubbard U correction (DFT+U). We have identified that electron and hole polarons form at V and O sites, respectively. In conjunction with slow carrier transport, polaron also limits the available photovoltage, required to drive the PEC reaction, by pinning the Fermi level within band gap. We have also presented the concept of effective polaronic gap which plays an important role over the optical gap of any polaronic materials for PEC application. The calculated effective polaronic gap (1.22 eV) of $BiVO_4$ is substantially lower than the experimental optical gap (2.40 eV), and even smaller than the least required energy (1.23 eV) to split water. These results correlate well with recent experimental studies.

5. 1. Introduction

The conversion of solar energy into easily transportable and storable chemical fuel in the form of H_2 is regarded as a potential carbon footprint free clean energy route to attain the 21st century energy security and stability[1–5]. Photoelectrochemical (PEC) cell is one of the developing technologies which splits H_2O into H_2 and O_2 using sunlight. The crucial component of water

splitting PEC cell is the solar absorber material, and it must meet several simultaneous stringent requirements in order to harness solar energy effectively. These requirements include, among others, fast charge transfer kinetics[1,6,7]. Among the best available photo absorber candidates, $BiVO_4$ is regarded as a champion material and received the most attention within the PEC community due to its near ideal band gap, suitable band alignment with respect to H_2O redox potential, good absorption of sunlight in the visible spectrum, and stability against photo-corrosion. Regardless of having good match of required criteria for PEC H_2O splitting, $BiVO_4$ has extremely low solar to hydrogen (STH) conversion efficiency with low photocurrent. Theoretically, $BiVO_4$ can reach STH conversion efficiency of ~10% with a photocurrent of ~8 mA cm^{-2} under standard AM 1.5 solar light irradiation[4,8–10]. Until now, the maximum lab scale STH conversion efficiency of only 1.1% has been achieved for a standalone $BiVO_4$ PEC cell[11,12]. Kristine et. al[13]. reported a list of top performing modified $BiVO_4$ photoanodes. All of these modified $BiVO_4$ photoanodes showed moderate STH conversion efficiency. The reported major efficiency loss channels include poor charge separation, slow charge transfer kinetics, and high recombination rate[14–16]. So far, various strategies have been considered to reduce the efficiency loss, but none yield STH conversion efficiency close to theoretical value. The major efficiency limitation stems from the extremely slow carrier mobility, on the order of 10^{-4} $cm^2V^{-1}s^{-1}$ at 300K for $BiVO_4$, (it is sufficiently lower, for example, compared to the mobility in single crystal Si, which is of the order of 10^2-10^3 $cm^2V^{-1}s^{-1}$ depending on doping level at 300K)[17]. Such a slow carrier mobility is an indication of strong carrier-lattice interaction, which eventually favors trapping of charge carriers (electron/hole) as polaron[18,19] in strongly correlated materials like $BiVO_4$, Fe_2O_3, $CuFeO_2$, $CaMnO_3$ etc[19–21]. Polaron forms when slow moving charge carriers displace surrounding atoms around a specific atomic site from their equilibrium and distorts the

lattice locally to form a potential well[22]. There are two types of polarons depending on the extent of local lattice distortion: highly localized small polaron where the spatial extent of lattice distortion is much smaller compared to the unit cell, and large polaron where the extent of lattice distortion is larger than the unit cell[17,23]. Recently, Rettie et. al.[17,24] characterized the formation and transport of small polaron in W:$BiVO_4$ and Ti:Fe_2O_3 using DC electrical conductivity, Seebeck and Hall co-efficient measurements. Time resolved terahertz spectroscopy measurements by Butler et al.[25] and Ziwritsch et al.[26] also reported the carrier trapping in $BiVO_4$. Very recently, Hermans et. al.[27] identified polaron formation in $BiVO_4$ via in-situ photoelectron spectroscopy measurements. There are also reported theoretical studies to justify the experimental observations of polaron formation in $BiVO_4$. Kweon et al.[28–30] have calculated electron and hole polaron formation and their transport properties using hybrid density functional theory. They have reported that electron small polaron forms at V-atom with an estimated activation barrier of ~0.35eV for nearest neighbor hopping. They have also reported hole polaron formation at O-atoms around a Bi-polyhedron. Furthermore, they assumed Bi-site hole polaron transport as band conduction type. Due to the lack of explicit study of Bi-site hole polaron, we have explicitly studied Bi-site hole polaron formation in $BiVO_4$. Our study showed Bi-site hole localization generates shallow acceptor level just above ((~20 meV)) the valence band maxima, which we have discussed in detail in the result section. Taifeng Lui et al.[31,32] employed DFT+U theory to calculate polaron formation and their transport properties. They described electron and hole polaron at V and O site, respectively, as small polaron. Their predicted activation barrier for electron and hole polaron in different hopping directions ranges (0.19-0.78) eV and (0.17-0.85) eV, respectively. Very recently, Wiktor et al.[33,34] applied molecular dynamics simulation to

characterize electron and hole polaron formation at $BiVO_4$-water interface. There are also many theoretical studies[35–40] on polaron formation of different transition metal oxides (TMO).

Almost all the available literatures reported the formation and transport behavior of polaron, but the molecular level parameters as well as the key idea of photovoltage limitation by polaron was completely unexplored until the study reported by Lohaus et.al.[41] on α-Fe_2O_3. They have postulated the polaron induced photovoltage limitation by measuring the quasi-Fermi level splitting on α-Fe_2O_3. For PEC H_2O splitting reaction, sufficient photovoltage as overpotential is necessary for efficient charge separation as well as fast charge transfer. Thus, limitation on photovoltage induced by polarons restrict efficient charge carrier separation in the bulk as well as reduce the rate of charge transfer kinetics to electrolyte medium. All these factors adversely affect the STH conversion efficiency in $BiVO_4$. The photovoltage limitation corresponds to a fundamental limitation of the usable optical energy gap (or band gap). Instead of optical gap, a significantly smaller effective polaronic gap become important in any materials with competing polaron formation upon thermal excitation. Polaronic gap is defined as the energy difference between electron and hole polaronic states within the optical gap. Additionally, thermally activated polarons move extremely slow (~ 10^{-4} cm^2 $V^{-1}s^{-1}$)[17,24], which leads to higher recombination, shorter carrier lifetime, smaller diffusion length (~10nm) of the reactive polarons, which eventually limit the photoconversion efficiency of the photoanodes. Recent ultrafast carrier dynamics study[21,42,43] on α-Fe_2O_3 suggested that light activated polaron formation determines the charge separation, charge transfer kinetics and eventually the STH conversion efficiency. Very recently, Yannick et. al.[20] showed by in-situ interface formation and photo-electron spectroscopy measurements that STH conversion efficiency of delafossite $CuFeO_2$ is limited solely by small polaron formation on Fe sites. Hence, it is an utmost importance to get a

deeper understanding of key parameters associated with polaron formation in $BiVO_4$ at atomistic level which will eventually help to overcome the efficiency bottleneck in $BiVO_4$ and to design $BiVO_4$ based photocatalyst. In this study, we have presented detail electronic structure calculations to understand the limitation of photovoltage in $BiVO_4$ imposed by polaron formations. We theoretically characterized polaron formation, determined energetics of polaronic state, and compared them with available experimental data. The comparison of calculated data showed a good agreement with published experimental results. We have also presented the polaron transport behavior as well as supercell size dependency on the polaron formation in $BiVO_4$. Finally, we presented an outlook on how to overcome the efficiency bottleneck results from polaron formation in the results and discussions section.

5. 2. Computational Methodology

First principles spin polarized density functional theory (DFT) calculations were performed using the Vienna ab initio Simulation Package (VASP)[44]. The exchange and correlations were described by the PBE (Perdew-Burke-Ernzerhof) functional[45] within the generalized gradient approximation (GGA). Projector-augmented wave (PAW)[46] method was employed to treat the ion-electron interactions. To model polaron in $BiVO_4$, we have used a 96 atoms supercell with periodic boundary conditions in all three directions. The 1st Brillouin zone (BZ) was sampled using the Mohkhorst-Pack (MP) scheme into a 3×3×5 k-point grid for geometric optimization, and a higher k-point gird has been used for density of states (DOS) and polaronic state calculations. The supercell was fully relaxed until the residual forces on all the constituent atoms become smaller than 0.01 eV Å^{-1}. A plane wave energy cut-off of 500 eV was used throughout the whole calculations, which gave a well converged results.

DFT has a well-known limitation of underestimating the electron self-interaction correction (SIC) error. Because of SIC error, DFT fails to produce localized solution for polaron calculations. To overcome the SIC error of standard DFT method, and to produce polaronic solution properly, we employed DFT+U framework[47] to study the polaron formation in $BiVO_4$. DFT+U theory has been proven successful towards producing localize polaronic solution in various transition metal oxides (TMO)[48–50]. Within this framework, the on-site Coulombic interaction term U and exchange parameter J are the main controlling factors to manipulate the SIC. U_{eff} = U-J controls the magnitude of the SIC correction. The respective values of U = 5 eV, 6 eV, 3 eV for V 3d, O 2p, Bi 6s orbitals and a fixed value of J = 1 eV was applied in this study. Similar kind of U values for $BiVO_4$ system has also been reported in the previous studies[31,32]. The chosen values of U in this study gave a well reasonable description of lattice constants, band gaps, as well as well-defined localized polaronic solution within the supercell.

To model electron polaron, one extra electron was added to the relaxed $BiVO_4$ supercell. In addition to adding an extra electron, to produce an electron polaronic state, we initially applied a small perturbation around a selected VO_4 tetrahedron to break lattice symmetry prior to structural relaxation. Similarly, for hole polaron, one extra hole was added by removing an electron from the relaxed supercell. Then a small perturbation around a selected Bi-site or O-site was applied for Bi-site or O-site hole polaron, respectively. In both (electron/hole polaron) cases, a compensating homogeneous background counter charge was also added to ensure the charge neutrality of the supercell.

To model the polaron mobility, we have used Einstein's equation of mobility[51,52]-

$$\mu = \frac{eD}{K_B T} = \frac{e(1-c)a^2 \upsilon_0 e^{-\left(\frac{E_a}{K_B T}\right)}}{K_B T}.$$

The migration of polaron from initial to final polaronic configuration was modeled by distorting the initial atomic positions toward the final atomic positions. The intermediate configurations between initial and final states were obtained by linear interpolation. Due to the periodicity, initial and final configurations are identical, and transition state occurs at midpoint between initial and final state. Finally, the activation barrier was calculated by subtracting the energy between transition state and initial state. In addition, we have used the "PHONOPY" code[53] to calculate the phonon vibration frequency required to calculate polaron mobility.

5. 3. Results and discussions

5. 3. 1. Pristine $BiVO_4$

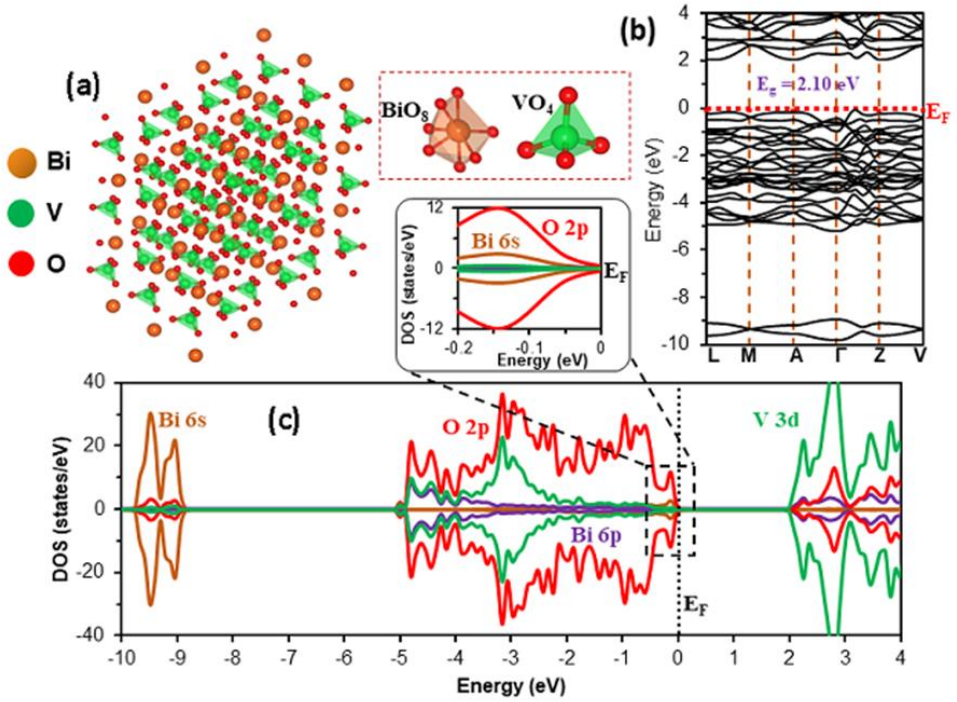

Figure-5. 1: (a) Crystal structure of monoclinic scheelite $BiVO_4$ supercell with its respective VO_4 and BiO_8 polyhedron. The equilibrium V-O bond length is ~1.74Å and Bi-O bond length ranges from ~2.46 Å-2.51Å (b) Electronic band structure of monoclinic $BiVO_4$. The Fermi level is set at zero eV and indicated by the red dashed line. (c) Orbital decomposed electron density of states (DOS) of $BiVO_4$. The energy zero eV is set at the Fermi level (E_F), which is indicated by vertical dashed line. The inset shows the amplified view for the top of the valence band.

At ambient condition, clinobisvanite scheelite type $BiVO_4$ crystallizes into monoclinic phase (space group: C2/c). The calculated lattice constants are given in SI table 1. In this structure, Bi and V atoms form alternate layers of VO_4 tetrahedron and slightly distorted BiO_8 dodecahedron. Within BiO_8 polyhedron, each O atom comes from eight isolated VO_4 tetrahedra. The calculated equilibrium V-O bond length is ~1.74Å and equilibrium Bi-O bond length ranges from ~(2.46-2.51)Å. Figure 1(a) shows the crystal structure of $BiVO_4$ supercell with its VO_4 and BiO_8 polyhedron. Figure 1(b-c) shows the electronic band structure and orbital projected density of states (DOS) of $BiVO_4$. As shown in DOS plot, the valence band maximum (VBM) is mainly composed of O 2p orbitals and there is some non-negligible contribution from Bi 6s orbitals. The hybridization among Bi 6s and O 2p states create anti-bonding orbitals near the Fermi level (0 eV) and bonding orbitals lie far below the Fermi level (~8.5-10 eV). Due to the low-lying O 2p orbitals character, the valence band edge of $BiVO_4$ is positioned at sufficiently lower energy position with respect to oxygen evolution potential (H_2O/O_2)[17]. On the other hand, the conduction band minimum (CBM) is predominantly composed of highly localized V 3d orbitals. Due to the strong localized nature of V 3d orbitals, some of the conduction electrons can be trapped within the unoccupied d bands and can form electron polaron. In case of $BiVO_4$, electron small polarons form at V-site and change the oxidation state of V atom from V^{5+} to V^{4+}. On the other hand, hole polarons can form at both Bi and O site and transform the oxidation state of Bi-atom from Bi^{3+} to Bi^{4+} and O-atom from O^{2-} to O^{-}, respectively. Furthermore, the coupled Bi 6s-O 2p anti-bonding state near the Fermi level get stabilized by mixing with Bi 6p unoccupied states in the conduction band via the monoclinic lattice distortion, which eventually, makes the monoclinic scheelite phase energetically favorable and photo catalytically more active than the other polymorphs of $BiVO_4$[54,55].

5. 3. 2. Electron polaron in $BiVO_4$

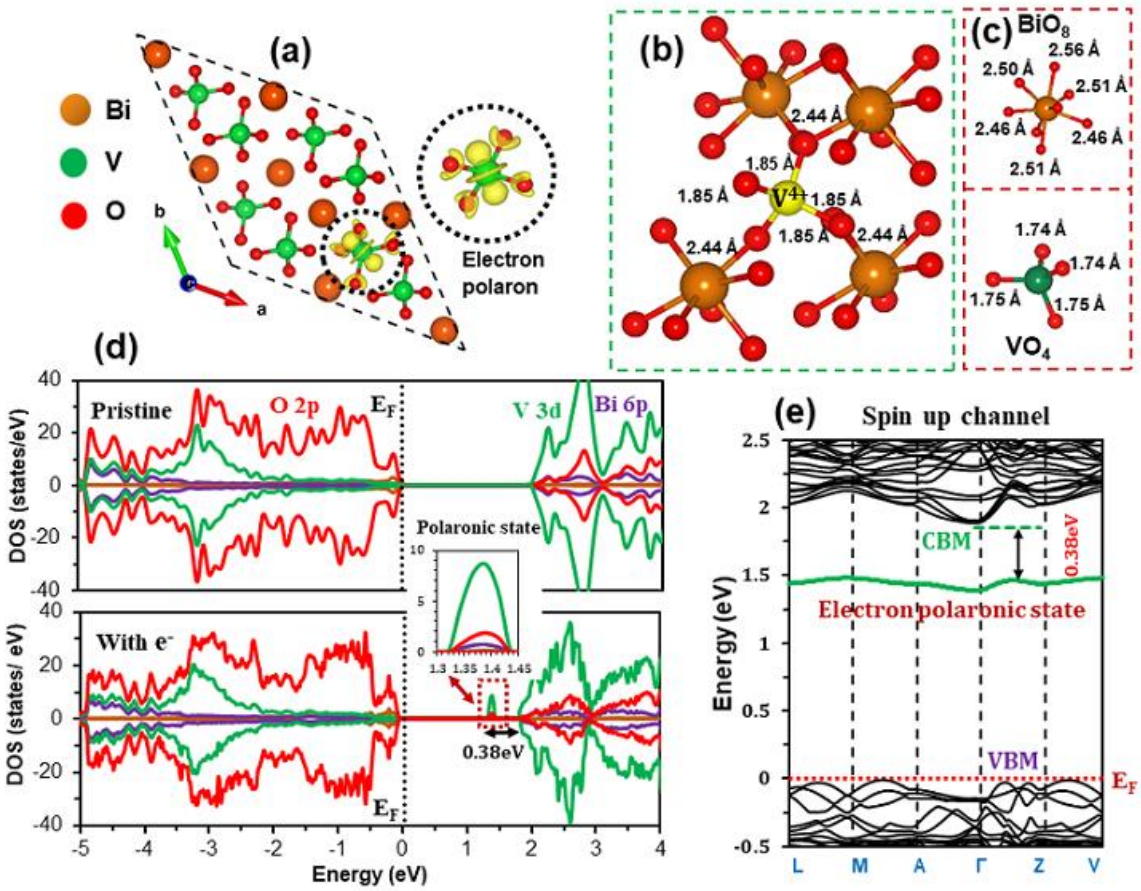

Figure-5. 2: (a) Charge density difference plot of localized electron polaron in V-site. The charge difference is taken between the cell with an extra electron and the cell without an extra electron. The density plot is drawn with an isosurface value of 0.004 $eÅ^{-3}$. The yellow isosurface indicates the localization of electron. (b) Geometry of local lattice distortion due to electron polaron formation. Polaron is formed in V^{4+} lattice site as indicated by yellow sphere. (c) Equilibrium V-O and Bi-O bond lengths of respective VO_4 and BiO_8 polyhedron.(d) Orbital decomposed electron density of states (DOS) of $BiVO_4$ with an extra electron. The energy zero is set at the Fermi level (E_F), which is indicated by vertical dashed line. The electron polaron state is seen in the up-spin channel as shown by the arrow symbol. The electron polaronic state is below 0.38 eV from the CBM. The inset figures show the amplified view of electron polaronic state. (e-f) Electronic band structure for spin up and down channels, respectively.

Polaron formation is ubiquitous in transition metal oxides (TMO)[17,24,36–38] as well as organic semiconductors[56,57]. Polaron forms when slow moving charge carriers locally distort the lattice and get trapped at lattice sites. Trapping of charge carriers as polaron generates deep electronic

state within the band gap of the material. Therefore, energetics of the deep polaronic state within the gap plays crucial role in determining carrier separation, charge transfer kinetics, PEC reaction, and eventually the STH conversion efficiency. Irrespective of nondispersive nature of the deep polaronic state (indication of heavy polaron effective mass), these states can act like carrier recombination center. Very recently, Shababa et al.[58] identified the deep electron polaronic state in bulk $BiVO_4$ as a hole trapping center using five complementary electrochemical, thermal and optical techniques. Polaron also limits the available photovoltage, a key requirement for PEC reaction, by pinning the Fermi level within the band gap. Very recently, this not-so-much unexplored idea has been demonstrated by Lohaus et. al[41] for hematite (α-Fe_2O_3) via photoelectron spectroscopy. In this paper, we have also performed a detail theoretical investigation to understand how polaron limits the photovoltage in $BiVO_4$, which has been discussed extensively in the following section. In this section, we have discussed the theoretical characterization of electron polaron formation and energetics of the resulting electron polaronic state.

Like other transition metal oxides (TMO), $BiVO_4$ has localized empty d-bands (V-3d orbitals) in the conduction band minimum (CBM). Due to the localized nature of d orbitals as well as strong carrier-lattice interaction in $BiVO_4$, some of the empty V-3d orbitals become occupied by trapping conduction electrons generated by photo excitation or by electrons coming from defects i.e., O-vacancy in case of $BiVO_4$. In general, O-vacancies are the most prominent type of vacancy defect in metal oxides. A single O-vacancy in the lattice leads to transfer of two extra electrons which can act like free carrier or can form polaron by getting trapped at the adjacent metallic sites depending on the materials. Typically, O-vacancy generates shallow donor state at the bottom of the CBM and responsible for the n-type character of the material. But in $BiVO_4$,

O-vacancy produces deep electronic states. Cooper et. al.[59] and Kim et. al.[60] showed that these states are indeed deep and have negative ionization energy, which leads O-vacancy center to have +2 charge state. We have calculated that these two extra electrons coming from the O-vacancy form small polaron by means of self-trapping at nearby V-atoms (see SI figure 1). By implementing Hybrid DFT calculations, Seo et. al.[61] explicitly demonstrated the formation of small polaron by the extra electrons coming from O-vacancy defect in $BiVO_4$. In this study, we have followed the most common method[28,31,32,35,36,61] of polaron calculation i.e., addition (or subtraction) of an extra electron to (or from) the supercell, to calculate electron (or hole) polaron in pristine $BiVO_4$. The detail of the polaron calculation methodology has been discussed in the computational methodology section. In case of electron polaron, the extra electron gets trapped at V site after full relaxation and forms polaron by filling up the empty V-3d orbitals in CBM. Electron trapping at V-site changes the oxidation state of that V-atom from $V^{5+} \rightarrow V^{4+}$. Figure 2(a) shows the localized electron polaron charge density at reduced V^{4+}-site. A small portion of electronic charge density is also shared by the nearby O atoms. The extra electron fills the lowest energy V-$3d_z^2$ orbital as it is clearly seen by the shape of iso-surface of the localized polaronic charge density. In addition to carrier localization, polaron formation is always associated with a local lattice distortion. Figure 2(b) shows the local lattice distortion around the V^{4+} reduced site. The bond length around the reduced V-site (i.e., V^{4+}-O bonds) become elongated by ~7% compared to the equilibrium V^{5+}-O bond length. The V^{4+}-O bond length elongation is attributed to the Coulombic repulsion resulted from partial filling of V-3d and O-2p hybridized orbitals near the reduced site. On the other hand, Bi-O bond length around the reduced V^{4+}-site become shorter (by ~5%) compared to the equilibrium Bi-O bond lengths of undistorted geometry (non-polaronic geometry). The Bi-O bond length shortening is attributed to the strong hybridization

between Bi-6s and O-2p orbitals as well as reduction of interaction between Bi-6p orbitals above the CBM with (Bi-6s+O-2p) antibonding states below the VBM. The other (far away from the reduced V-site) V-O and Bi-O bonds remain unchanged. The spatial extent of the local lattice distortion is limited to nearest neighbor atomic sites (~3.85 Å radius around V^{4+} reduced site) which tells that the resulting electron polaron is small polaron in nature.

We now turn our discussion to the energetics of electron polaronic state. Electron polaron generates a deep localized state within the band gap as shown in figure 2(d-e). The calculated polaronic state is located ~ 0.38 eV below CBM. A recent in-situ photoelectron spectroscopy experiment[27] reported the position of deep state at ~0.3 eV below CBM. Another theoretical study[31] also predicted that the polaronic state lies at ~ 0.3 eV below CBM. This present study overestimates the polaronic state position by ~0.08 eV compared to the reported values, but the calculated value is well comparable within the DFT limit. For an ideal PEC absorber material, the conduction band edge must straddle the H^+/H_2O potential to provide enough overpotential for efficient charge transfer to electrolyte medium. Instead of free conduction electron, if electron polaron become the dominant charge carrier in any PEC absorber materials, then electron polaronic state also has to be straddled at higher energy with respect to H^+/H_2O potential for efficient H_2O reduction by polarons. In case of $BiVO_4$, the consensus of dominant charge transfer mode is site to site hoping of excited polarons. It is reported[62] that the conduction band edge of $BiVO_4$ is ~0.1 eV lower in energy with respect to H^+/H_2O reduction potential. Hence, the calculated electron polaronic state will lie far lower energy (~0.48 eV) w.r.t. H^+/H_2O potential. Such a low lying polaronic state will not be able to provide enough overpotential to drive the reactive polarons to electrolyte medium at room temperature. Therefore, efficient polaronic charge transfer will be hindered. This will negatively affect the PEC reaction as well as the STH

conversion efficiency. The other attributes of low quantum yield i.e., slow mobility and photovoltage limitations has been discussed in later sections.

5. 3. 3. Hole polaron in $BiVO_4$

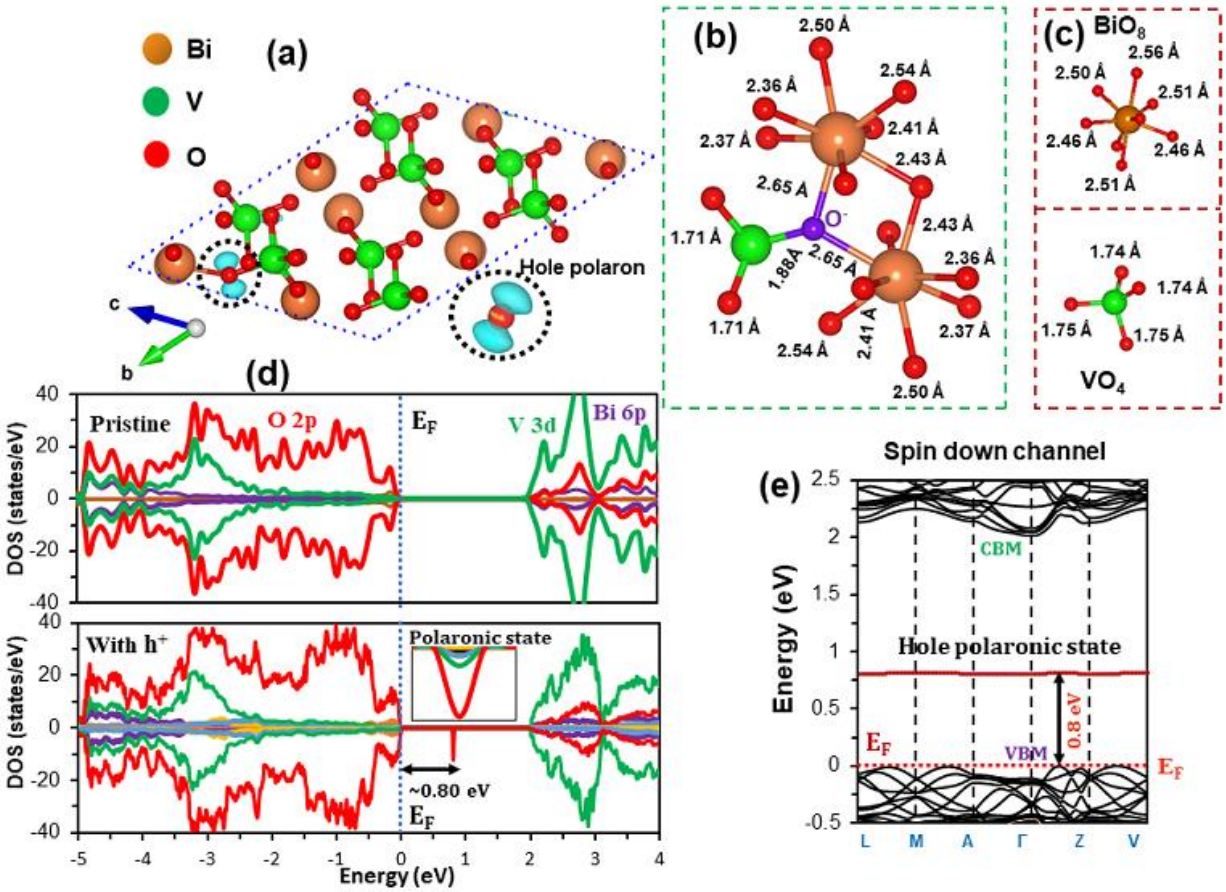

Figure-5. 3: (a) Charge density difference plot of localized hole polaron at O-site. The charge difference is taken between the cell with an extra hole and the cell without an extra hole. The density plot is drawn with an isosurface value of 0.002 $eÅ^{-3}$. The azure blue isosurface indicates the localization of a hole. (b) Geometry of local lattice distortion due to hole polaron formation. Polaron is formed at O^- lattice site as indicated by purple blue sphere. (c) Equilibrium V-O and Bi-O bond lengths of respective VO_4 and BiO_8 polyhedron. (d) Orbital decomposed electron density of states (DOS) of $BiVO_4$ without and with an extra hole. The energy zero is set at the Fermi level (E_F), which is indicated by vertical dashed line. The hole polaron state is seen in the down spin channel. The hole polaronic state is above 0.80 eV from the VBM. The inset figures show the amplified view of hole polaronic state. (e) Electronic band structure for spin-down channel.

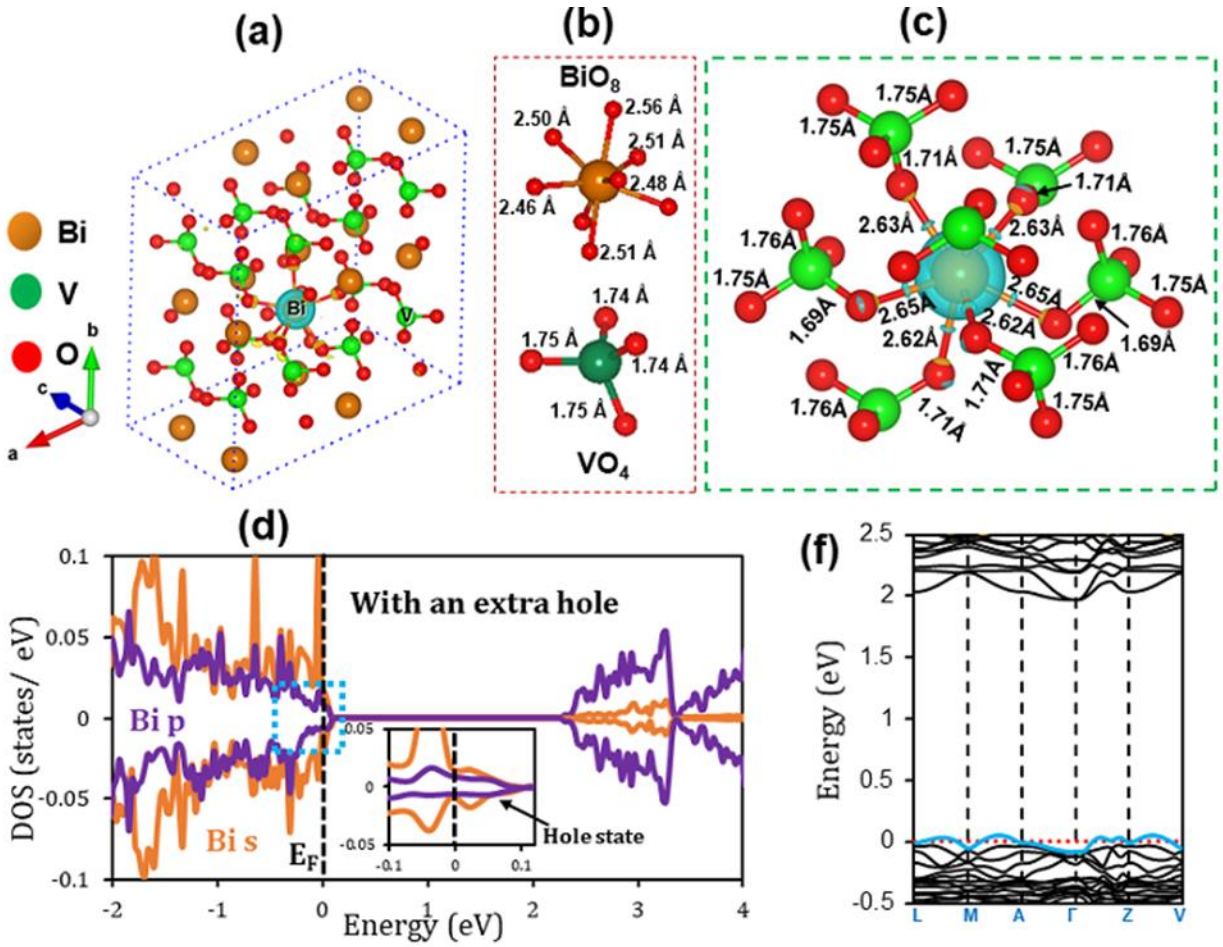

Figure-5. 4: (a) Charge density difference plot of localized hole polaron on Bi-site. The charge difference is taken between the cell with an extra hole and the cell without an extra hole. The density plot is drawn with an isosurface value of 0.015 eÅ^{-3}. The azure blue isosurface indicates the localization of a hole. (b) Equilibrium V-O and Bi-O bond lengths of respective VO_4 and BiO_8 polyhedron. (c) Geometry of local lattice distortion due to hole polaron formation. Polaron is formed in Bi^{2+} lattice site as indicated by azure blue sphere. (d) The orbital projected density of states for Bi 6s and 6p orbitals. The amplified figure in the inset panel shows the hole state created by Bi hole polaron. (f) Electronic band structure of Bi-site hole polaron. The hole state is denoted by light blue color band.

Now, we turn our discussion to hole polaron in $BiVO_4$. As shown in the DOS plot of pristine $BiVO_4$ (figure 1(c)), VBM is predominantly O-2p character, and there is also a small contribution from the stereo-chemically active Bi-6s orbitals[55]. So, hole polaron in $BiVO_4$ can form either at O-site or Bi-site, or at both sites simultaneously. Based on the higher orbital contribution to the VBM, the hole polaron will most likely form at O-site rather than Bi-site; in

addition, spherically symmetric Bi-6s orbital is far less localized than the O-2p orbitals. There are studies[29–32] which reported O-site hole polaron, but no explicit study on Bi-site hole polaron to the best of our knowledge. Most of the studies demonstrated simultaneous hole polaron formation at both sites in a BiO_8 polyhedron. Wiktor et. al.[33,34] reported simultaneous hole polaron formation at both Bi and O-sites via molecular dynamics simulation. Another experimental study by Yannick et. al.[27] also presumed the independent formation of Bi-site hole polaron based on the spectroscopic signature of in-situ photoelectron spectroscopy. In this study, we have explicitly investigated hole polaron formation at both sites separately and calculated their respective polaron binding energy (BE) to determine their qualitative formation probability in $BiVO_4$. In order to calculate hole polaron, we have added an extra hole by removing one electron from the supercell and slightly perturbed the desired atomic site to facilitate the hole localization. Our calculations showed that hole trapping is possible on both sites independently. Unlike O-site hole trapping, which is purely polaronic in nature, Bi-site hole trapping acts like a shallow acceptor doping. To answer which lattice site is more favorable for hole trapping, Bi-site or O-site, we calculated the polaron binding energy for both sites. The polaron binding energy is defined[63] as,

$$E_{bind}^{\pm} = E^{polaron}(N \mp 1) - E^{perf}(N \mp 1),$$

where $E_{bind}^{\pm}$ is the polaron binding energy and (+) sign corresponds to hole polaron, while (-) sign corresponds to electron polaron. A negative $E_{bind}^{\pm}$ implies energy gain and hence formation of a stable polaron. $E^{polaron}$ is the total energy of the system with polaronic (distorted) geometry, E^{perf} is the total energy of the system with non-polaronic (undistorted) geometry and the number of electrons is given in parenthesis, where *N* is the total number of electrons of the neutral system. The calculated binding energy is negative for both O-site (BE ~ −189.2 meV)

and Bi-site (BE ~ –5.5 meV) hole polaron which implies that holes trapping is possible on both sites independently. But the energy gain for O-site hole polaron is much higher than Bi-site, which indicates that O-site hole polaron will be thermodynamically more stable than at Bi-sites. Bi-site hole polaron actually behaves like an acceptor state and its transport is more likely to be band conduction type, which we have discussed in the later section of polaron transport.

Now we are going to discuss the hole polaron formation at O and Bi site as well as the energetics of respective electronic states arising from hole trapping. Figure 3 shows the hole polaron formation at O-site. As shown in figure 3(a), the excess hole is trapped within the O-2p orbital as it is clearly seen by the shape of the isosurface charge density. Due to hole trapping at the O-site as indicated by the circular dotted boundary, the oxidation state of formerly O^{2-} become O^{-}. Formation of hole trapping at O-site also distorts the lattice locally around the O^{-} site. Figure 3(b) shows the local lattice distortion due to hole polaron formation at O-site. The V-O^{-} and Bi-O^{-} bonds length around the polaronic site is elongated by (~8-10%) compared to the equilibrium bond length of pristine geometry. The bond length elongation is attributed to the weakening of V-O^{-} and Bi-O^{-} bond strength. The other V-O and Bi-O bonds of respective VO_4 and BiO_8 polyhedra connected to the O^{-} polaronic site become shorter (~2-5)% than the equilibrium bond length. The V-O and Bi-O bonds far from the polaronic site are unchanged as they are in the pristine case. The spatial extension of local lattice distortion due to O-site hole polaron is not more than ~3.85Å radius around the polaronic site (less than lattice constant). So, this indicates that O-site hole polaron is small polaron in nature. The trapping of hole at O-site as polaron generates a deep highly localized (nondispersive) state within the band gap as shown in the DOS plot as well as band structure plot in figure 3(d-e). The calculated hole polaronic state is located ~0.8 eV above the valence band edge. The reported theoretical[31] and experimental[27] position of

polaronic state with respect to valence band edge are 0.9 eV and 1.02 eV, respectively. The calculated position of polaronic state is close to the reported theoretical value but a little off from the experimental reported value, but comparable within the DFT limit. Since the carrier transport in $BiVO_4$ is mainly governed by polaron conduction, it is important that the deep electronic state originated from hole polaron lies sufficiently lower in energy with respect to O_2/H_2O oxygen evolution potential. This ensures that the hole polaron gets sufficient energy as overpotential to transfer themselves to electrolyte medium for efficient PEC reaction. In pristine $BiVO_4$, the VBM is positioned sufficiently lower in energy (~1.27 eV)[17,64] with respect to O_2/H_2O redox potential (see figure 5(b)), but hole polaronic state is positioned relatively closer in energy, ~0.47eV below O_2/H_2O redox potential (see figure 5(b)). Due to this relatively low overpotential, the transport of excited hole polaron to the electrolyte will be kinetically slower. In fact, it was reported[14–16] that the oxygen evolution reaction (OER) is kinetically very slow for $BiVO_4$ photoanode. This sluggishness of OER is originated from the fact that the hole polarons have less overpotential to drive them to the electrolyte medium. This eventually attributes to the limitation of PEC as well as STH conversion efficiency. In addition, the hole polarons also limit the available photovoltage of $BiVO_4$ by pinning the Fermi level within the gap, which we have discussed in detail in the following section.

For the hole trapping at a Bi-site, an initial perturbation was applied to a selected Bi atom. As shown in figure 4(a), the extra hole gets trapped within Bi-6s orbital, which is evident by the shape of the isosurface for charge density. Due to hole trapping at Bi-site, Bi-O bonds within the perturbed BiO_8 dodecahedron elongated by ~6% compared to the equilibrium Bi-O bond length of pristine system. On the other hand, the nearby V-O bonds get shorter by ~1% than the equilibrium bond length. The rest of the Bi-O and V-O bonds far from the perturbed Bi-site

remain unchanged. The associated local lattice distortion is shown in figure 4(b). Hole trapping at Bi-site changes its oxidation state from Bi^{3+} to Bi^{4+} which generates a shallow dispersive electronic state just above (~20 meV) the valence band edge as shown in the DOS plot and band structure plot (see figure 4(d-e)). Another theoretical study[29] also reported a similar type feature of shallow hole polaronic state in $BiVO_4$. Due to shallow nature of the electronic state originated from the hole trapped at Bi-site having s-orbital character, the state at Bi-site behaves like an acceptor state rather than a hole polaron. Due to this fact, the transport will more likely be band conduction type. Kweon et al.[29] calculated the mobility of Bi-hole polaron by considering band like transport. Note that since the O-site hole polaron is more stable than the Bi-site hole polaron, and because of the energetic position of the respective polaronic states, the O-site hole polaron will play an active and dominant polaronic role towards hole conduction and to PEC water splitting reactions.

5. 3. 4. Photovoltage limitation and relative position of polaronic states

A suitable band gap and proper alignment of band edges with respect to H_2O redox potentials are the two most important requirements that the absorber materials must satisfy in order to split H_2O efficiently. These two requirements act like a determining factor for charge carriers' separation and transfer kinetics. The energy gap provides the upper limit of the available photovoltage needed for charge carrier separation within the bulk, and the relative position of band edges with respect to H_2O redox potentials determines the necessary overpotential to transfer the charge carrier from bulk to the electrolyte medium in order to drive the hydrogen evolution reaction (HER) and oxygen evolution reaction (OER). From a theoretical point of view, a photovoltage of at least 2.0 eV (1.23 eV for water splitting potential + overpotential) has to be generated by the absorber material for efficient H_2O splitting. Moreover, the band edge positions

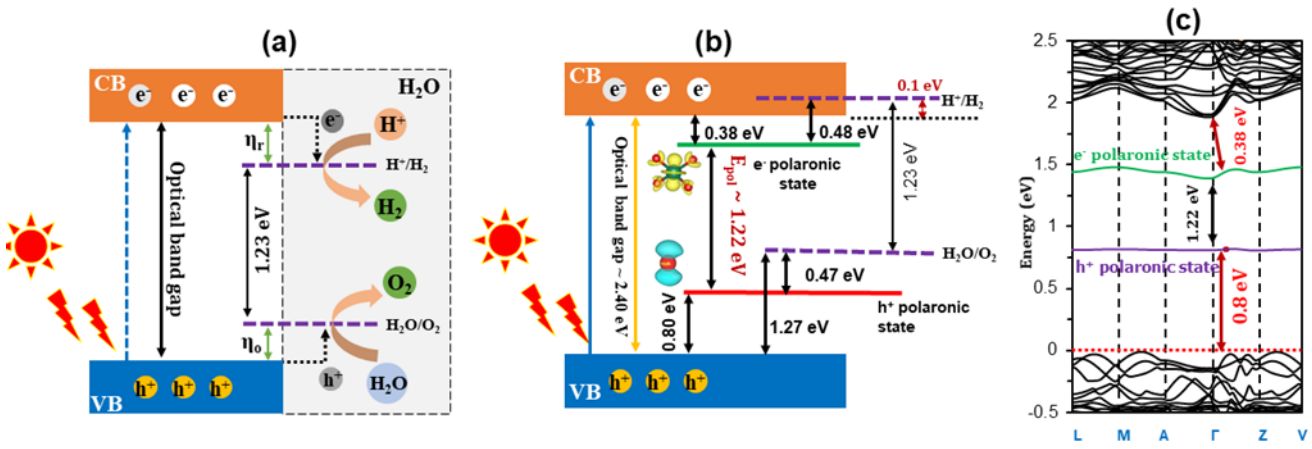

Figure-5. 5: Schematic representation of (a) Ideal case of PEC water-splitting process using photocatalyst. On absorption of solar photon, an electron (e^-) from the valence band (VB) get excited to the conduction band (CB), leaving a hole (h^+) in the VB. The CB electrons and VB holes take part in the reduction of H^+ to H_2 and oxidation of H_2O to O_2 reaction, respectively. (b) $BiVO_4$ photocatalyst in which some of CB electrons and VB holes form polarons within the bulk. The electron polaron state lies 0.38 eV below the CBM and hole polaron state lies 0.80 eV above the VBM. The polaronic gap is 1.22 eV which is less than the required gap (1.23 eV). (c) The calculated band structure with both the electron and hole polaronic state.

have to be aligned properly with respect to H_2O redox potentials. The CB edge has to straddle above the hydrogen evolution (H^+/H_2) potential and VB edge has to straddle below the oxygen evolution (H_2O/O_2) potential. Figure 5(a) shows the ideal scenario of the relative position of band edges with respect to H_2O redox potentials of a PEC absorber material. It is very important to note that, in general, the above-mentioned criteria are applicable if the charge carrier transport is band-conduction type. Instead of band conduction, if the charge transport of absorber material is dominated by thermally activated slow moving polarons, the polaronic gap and the position of polaronic states w.r.t. H_2O redox potentials become the determining factor for carrier separation and transport than the band gap and band edge position.

Polaronic gap is defined as the energy gap between the electron- and hole- polaronic states within the gap. For polaron conducting photo-absorber material, polaronic gap as well as relative position of polaronic states with respect to H_2O redox potentials have to satisfy in a similar

manner as it is for band type conduction. The charge transport of $BiVO_4$ is polaronic which have been demonstrated experimentally[24–26] and theoretically[31–33]. We have also characterized polaron formation in $BiVO_4$ in this study. We have identified that electron and hole polaron pin the Fermi level at ~0.38 eV below CBM and ~0.8 eV above the VBM, respectively. This results in a relatively smaller effective polaronic gap (~1.22 eV) compared to optical gap (2.10 eV) as shown in figure 5(b-c). The estimated effective polaronic gap is also comparable with the experimentally obtained polaronic gap of 1.08 eV.[27] According to this energy profile, the polaronic gap is bounded by states that are mainly highly localized V 3d and O 2p states, classifying this material as charge-transfer type Mott insulators[65]. The calculated polaronic gap is in fact smaller than the least required energy (1.23 eV) to split H_2O. This finding reveals an important yet not well studied limitation of photocatalyst material for PEC application, and that is the reduction of available photovoltage by polaronic states. Polaron restricts the usage of available photovoltage by pinning the Fermi level within the band gap. Polaron induced limitation of photovoltage had been recently demonstrated in α-Fe_2O_3[41] and delafossite $CuFeO_2$[20]. Due to the reduced photovoltage, the efficient carrier (in this case polarons) separation within the bulk will be heavily hindered and this will eventually increase the carrier recombination, one of the major pathways for efficiency loss.

Now, we turn our discussion to the relative position of polaronic state with respect H_2O redox potential. As shown in figure 5(b), electron polaronic state straddles below the hydrogen evolution potential (H^+/H_2) by ~0.48eV. For ideal case, electron polaronic state supposed to straddle above the H^+/H_2 potential for efficient transfer of charge carriers to the electrolyte medium; however, this is not the case for electron polarons in $BiVO_4$. Such a significant misalignment between electron polaronic state and H^+/H_2 reduction potential will restrict the

reactive electrons to migrate into electrolyte to reduce H_2O into H_2. That is why, in practice, we need to apply external bias to reduce H_2O into H_2 using $BiVO_4$ photoanode. On the other hand, the calculated hole polaronic state is located ~0.47 eV below the oxygen evolution potential (H_2O/O_2). Even though the hole polaronic state aligns properly with respect to H_2O/O_2 oxidation potential, the observed oxygen evolution reaction (OER) still shows sluggish reaction kinetics. The slow kinetics results from the fact that the highly localized hole polaron (as indicated by the nondispersive hole polaronic state in the band structure plot in figure 5(c)) are too heavy and OER lack sufficient overpotential to drive the reactive holes in electrolyte to oxidize H_2O in to O_2. These negative attributes coming from polarons in $BiVO_4$ directly hamper the PEC H_2O splitting reaction as manifested by low STH conversion efficiency as well as smaller photocurrent.

5. 3. 5. Polaron transport in $BiVO_4$

Polaron transport takes place via thermally activated site to site hopping. In this study, we have calculated the electron and hole polaron mobility using the framework of Marcus/Holestein theory[66,67]. In this framework, electron and hole polaron migrates from initial to final polaronic configuration by gradually distorting the lattice. Due to the identical chemical environment (such as atomic coordination) of initial and final configuration, the transition state occurs at the midpoint between these two configurations. Then the site to site hopping activation barrier, E_a can be estimated by taking the energy difference between transition and initial state. The calculated activation barrier for electron (V-site polaron) and hole (O-site polaron) polaron is 0.40 eV and 0.28 eV, respectively. Previously reported experimental[64] and theoretical[28] (hybrid DFT method) value of electron polaron activation barrier is 0.30 eV and 0.35eV, respectively. Another DFT+U[32] study also reported a range of electron polaron activation barrier from (0.36-

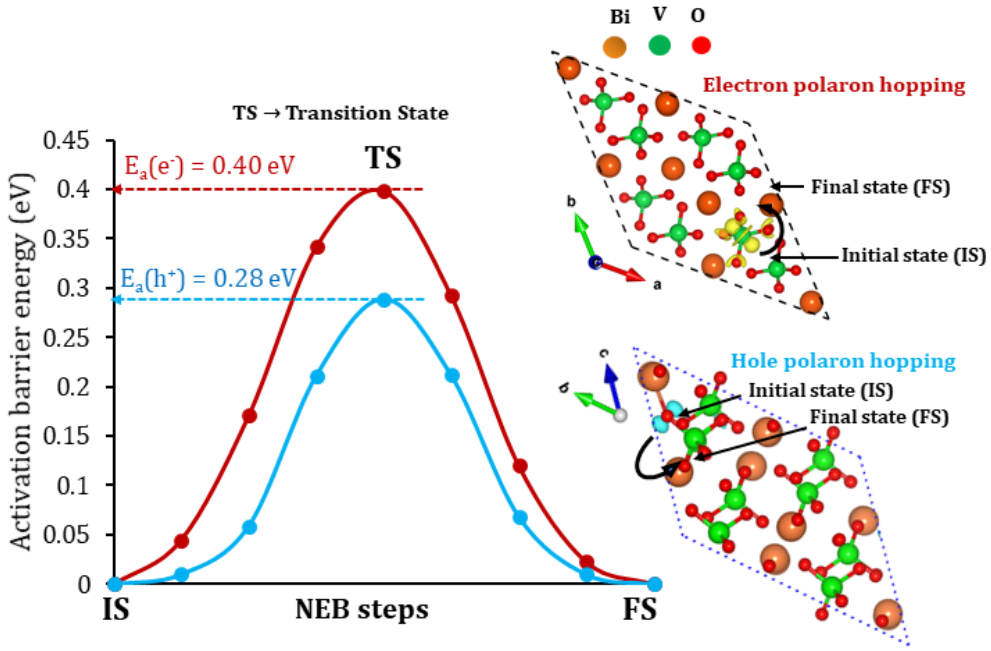

Figure-5. 6: Activation barrier energy, Ea, for electron and hole polaron along the migration path linearly interpolated between the initial and final configuration state. The transition state (TS) is located in the midway between initial state (IS) and final state (FS). Right hand side panel shows the electron and hole polaron migration pathway considered in this study.

.48eV) depending on various V-V hopping distance in different hopping directions. The calculated activation barrier for electron polaron in the shortest V-V hopping distance along the direction shown in SI figure 4 of this study falls within the range and compare well with the previously reported DFT+U[32] method. On the other hand, the reported[32] hole polaron activation barrier varies from (0.17-0.58 eV) depending on various migration path. Figure 6 shows the calculated activation barrier for electron and hole polaron.

We have used the most commonly used Einstein formula to estimate the electron and hole polaron mobility. The polaron mobility is given by the following equation[30–32,36],

$$\mu = \frac{eD}{K_B T} = \frac{e(1-c)a^2 \upsilon_0 e^{-\left(\frac{E_a}{K_B T}\right)}}{K_B T},$$

where, e is the electron/hole charge, $(1-c)$ is the probability that a neighboring site is available for hopping, a is the nearest neighbor hopping distance, υ_o is the longitudinal optical phonon frequency, E_a is the activation barrier, K_B is the Boltzmann constant, and T is temperature. We have used $(1-c)=1$, a = 3.92 Å (2.78 Å) for electron (hole) polaron, and T = 300K. Additionally, for electron and hole polaron mobility calculation, we have used υ_o = 10 THz and 5 THz, respectively, which we have obtained from our phonon frequency band and dos calculations (details in SI figure-2 in the supplementary information). The estimated electron polaron mobility is μ_e = 1.12×10^{-6} $cm^2V^1S^{-1}$. On the other hand, the estimated hole polaron mobility is μ_h = 2.96×10^{-6} $cm^2V^{-1}S^{-1}$. The calculated electron and hole polaron mobility in $BiVO_4$ is of the same order as in TiO_2 and Ga_2O_3 at room temperature[36,68,69]. Note that the calculated hole polaron mobility is around three times higher than the electron polaron mobility, even though both electron and hole polaron mobility is far lower than the theoretical upper limit of 1 $cm^2V^{-1}S^{-1}$ at room temperature[70]. Faster O-site hole polaron mobility as well as band type conduction for Bi-site hole explains why oxygen evolution reaction (OER) is faster than the hydrogen evolution reaction (HER).

Now we turn into Bi-site hole polaron mobility discussion. Since the hole localization at Bi-site generates acceptor state just above the VB edge, we have used Drude's model ($\mu=\frac{e\tau}{m^*}$) to estimate the hole polaron mobility assuming the band-type conduction of localized Bi-site hole. Here, τ is the scattering time and m* is hole effective mass. The scattering time τ ranges from 10^{-12} – 10^{-14} s at room temperature for many oxides[71,72], and we have used $\tau = 10^{-14}$s and m* = 0.8 m_e[29] for this present calculation. The calculated mobility turned out to be 22 $cm^2V^{-1}S^{-1}$. So, Bi-site hole polaron is much faster than the O-site small hole polaron. This is consistent with the general trend that band-type conduction is much faster than the small polaron hopping

conduction. Due to smaller activation barrier as well as less polaron formation energy of O-site hole polaron than V-site electron polaron, the hole polaron transport will relatively be dominant in $BiVO_4$. That is why OER is relatively faster than HER. The electron and hole polaron binding energy is provided in the supplementary figure 3.

Conclusion

Polaron plays the decisive role in determining the carrier separation, transfer as well as PEC reaction kinetics, and hence the quantum efficiency of some transition metal-oxide photoanode materials. Even though the formation and transport of polaron in TMO's are well studied, the mechanism of efficiency reduction by polaron has hardly been explored, especially in the case of PEC water splitting. By applying the state-of-the-art computational method, we have characterized the formation of polarons in $BiVO_4$ and provided detail atomistic view of the mechanism for efficiency reduction by polarons. We have found that electron and hole polaron states are formed within the band gap. Fermi level pinning by polarons generate a sufficiently smaller effective polaronic gap (E_{pol}) of 1.22 eV compared to the optical gap (2.10 eV). Hence, pinning of Fermi level by polarons limit the photovoltage that the photocatalyst material can attain, and directly restrict the carrier separation and chemical transformation that can be achieved. We theoretically showed the limitation of photovoltage by polarons in $BiVO_4$ photoanode after Lohaus et. al.[41] recently postulated this as a mechanism for moderate STH conversion efficiencies in hematite. In addition to photovoltage limitation, the misalignment of polaronic states with respect to H_2O redox potentials impact PEC reaction by restricting the polaronic charge transport to the electrolyte, therefore facilitate the loss of charge carriers by carrier recombination. Based on our calculations and other reported experimental observations, we further propose potential mechanisms which can either block the polaron formation or

increase the polaron mobility. Modification of ligand bonds by means of doping, forming metal oxo-hydroxides, or using multinary oxides are some of the potential ways of suppressing polaron in the crystal lattice. Finally, different synthetic route of materials can also be used to suppress polaron formation. For example- $BiVO_4$ forms O-vacancy defects which act as trapping center of electron polarons[68–70]. Very recently, a report[73] showed the reduction of electron polaron formation by suppressing O-vacancy defect formation via applying a specific synthetic technique.

Acknowledgement

The authors would like to thank Professor Wolfram Jaegermann for enlightening discussions. M.N.H. was supported by the national Science Foundation (Award No. DMR-1609811). M.N.H. and H.P.S. thank the Texas Advance Computing Center (TACC) (Austin-TX, USA) for their computational needs.

Competing Financial Interest

The authors declare no competing financial interests.

Key words

$BiVO_4$, Polaron, H_2, PEC water splitting, Density Functional Theory (DFT)

References:

[1] T.W. Kim and K.-S. Choi, Science (80-.). **343**, 990 (2014).

[2] M. Grätzel, Nature **414**, 338 (2001).

[3] J. Willkomm, K.L. Orchard, A. Reynal, E. Pastor, J.R. Durrant, and E. Reisner, Chem. Soc. Rev. **45**, 9 (2016).

[4] R. Li, H. Han, F. Zhang, D. Wang, and C. Li, Energy Environ. Sci. **7**, 1369 (2014).

[5] Lewis S. Nathan, Science (80-.). **351**, 353 (2016).

[6] Y. Park, K.J. McDonald, and K.S. Choi, Chem. Soc. Rev. **42**, 2321 (2013).

[7] K. Sivula and R. Van De Krol, Nat. Rev. Mater. **1**, 1 (2016).

[8] Y. Pihosh, I. Turkevych, K. Mawatari, J. Uemura, Y. Kazoe, S. Kosar, K. Makita, T. Sugaya, T. Matsui, D. Fujita, M. Tosa, M. Kondo, and T. Kitamori, Sci. Rep. **5**, 1 (2015).

[9] M.S. Prévot and K. Sivula, J. Phys. Chem. C **117**, 17879 (2013).

[10] Z.F. Huang, L. Pan, J.J. Zou, X. Zhang, and L. Wang, Nanoscale **6**, 14044 (2014).

[11] Q. Wang, T. Hisatomi, Q. Jia, H. Tokudome, M. Zhong, C. Wang, Z. Pan, T. Takata, M. Nakabayashi, N. Shibata, Y. Li, I.D. Sharp, A. Kudo, T. Yamada, and K. Domen, Nat. Mater. **15**, 611 (2016).

[12] Q. Wang, T. Hisatomi, Y. Suzuki, Z. Pan, J. Seo, M. Katayama, T. Minegishi, H. Nishiyama, T. Takata, K. Seki, A. Kudo, T. Yamada, and K. Domen, J. Am. Chem. Soc. **139**, 1675 (2017).

[13] K.R. Tolod, S. Hernández, and N. Russo, Catalysts **7**, (2017).

[14] Y. Liang, T. Tsubota, L.P.A. Mooij, and R. Van De Krol, J. Phys. Chem. C **115**, 17594 (2011).

[15] Y. Ma, S.R. Pendlebury, A. Reynal, F. Le Formal, and J.R. Durrant, Chem. Sci. **5**, 2964 (2014).

[16] T.S. Sinclair, B.M. Hunter, J.R. Winkler, H.B. Gray, and A.M. Müller, Mater. Horizons **2**, 330 (2015).

[17] A.J.E. Rettie, W.D. Chemelewski, D. Emin, and C.B. Mullins, J. Phys. Chem. Lett. **7**, 471 (2016).

[18] F. Giustino, Rev. Mod. Phys. **89**, 1 (2017).

[19] M.A. Husanu, L. Vistoli, C. Verdi, A. Sander, V. Garcia, J. Rault, F. Bisti, L.L. Lev, T. Schmitt, F. Giustino, A.S. Mishchenko, M. Bibes, and V.N. Strocov, Commun. Phys. **3**, 1 (2020).

[20] Y. Hermans, A. Klein, H.P. Sarker, M.N. Huda, J. Henrik, T. Thierry, and J. Wolfram, Adv. Funct.

Mater. **30**, 1910432 (2020).

[21] E. Pastor, J.S. Park, L. Steier, S. Kim, M. Grätzel, J.R. Durrant, A. Walsh, and A.A. Bakulin, Nat. Commun. **10**, 1 (2019).

[22] D. Emin, *Polarons* (Cambridge University Press, Cambridge, 2012).

[23] D. Emin, Phys. Rev. B **48**, 691 (1993).

[24] A.J.E. Rettie, W.D. Chemelewski, J. Lindemuth, J.S. McCloy, L.G. Marshall, J. Zhou, D. Emin, and C.B. Mullins, Appl. Phys. Lett. **106**, 022106 (2015).

[25] K.T. Butler, B.J. Dringoli, L. Zhou, P.M. Rao, A. Walsh, and L. V. Titova, J. Mater. Chem. A **4**, 18516 (2016).

[26] M. Ziwritsch, S. Müller, H. Hempel, T. Unold, F.F. Abdi, R. Van De Krol, D. Friedrich, and R. Eichberger, ACS Energy Lett. **1**, 888 (2016).

[27] Y. Hermans, S. Murcia-López, A. Klein, R. Van De Krol, T. Andreu, J.R. Morante, T. Toupance, and W. Jaegermann, Phys. Chem. Chem. Phys. **21**, 5086 (2019).

[28] K.E. Kweon, G.S. Hwang, J. Kim, S. Kim, and S. Kim, Phys. Chem. Chem. Phys. **17**, 256 (2015).

[29] K.E. Kweon and G.S. Hwang, Phys. Rev. B **87**, 205202 (2013).

[30] K.E. Kweon and G.S. Hwang, Appl. Phys. Lett. **103**, 1 (2013).

[31] T. Liu, X. Zhou, M. Dupuis, and C. Li, Phys. Chem. Chem. Phys. **17**, 23503 (2015).

[32] T. Liu, V. Pasumarthi, C. Laporte, Z. Feng, Q. Li, J. Yang, C. Li, and M. Dupuis, J. Mater. Chem. A **6**, 3714 (2018).

[33] J. Wiktor, F. Ambrosio, and A. Pasquarello, ACS Energy Lett. **3**, 1693 (2018).

[34] J. Wiktor and A. Pasquarello, ACS Appl. Mater. Interfaces **11**, 18423 (2019).

[35] M. Setvin, C. Franchini, X. Hao, M. Schmid, A. Janotti, M. Kaltak, C.G. Van de Walle, G. Kresse, and U. Diebold, Phys. Rev. Lett. **113**, 086402 (2014).

[36] N.A. Deskins and M. Dupuis, J. Phys. Chem. C **113**, 346 (2009).

[37] L. Bjaalie, A. Janotti, K. Krishnaswamy, and C.G. Van De Walle, Phys. Rev. B **93**, 115216 (2016).

[38] A. Janotti, J.B. Varley, M. Choi, and C.G. Van De Walle, Phys. Rev. B **90**, 085202 (2014).

[39] C. Di Valentin and A. Selloni, J. Phys. Chem. Lett. **2**, 2223 (2011).

[40] M. Jaime, H.T. Hardner, M.B. Salamon, M. Rubinstein, P. Dorsey, and D. Emin, Phys. Rev. Lett. **78**, 951 (1997).

[41] C. Lohaus, A. Klein, and W. Jaegermann, Nat. Commun. **9**, 1 (2018).

[42] L.M. Carneiro, S.K. Cushing, C. Liu, Y. Su, P. Yang, A.P. Alivisatos, and S.R. Leone, Nat. Mater. **16**, 819 (2017).

[43] J. Husek, A. Cirri, S. Biswas, and L. Robert Baker, Chem. Sci. **8**, 8170 (2017).

[44] G. Kresse and J. Furthmüller, Phys. Rev. B **54**, 11169 (1996).

[45] J.P. Perdew and Y. Wang, Phys. Rev. B **45**, 244 (1992).

[46] P.E. Blöchl, Phys. Rev. B **50**, 17953 (1994).

[47] S. Dudarev and G. Botton, Phys. Rev. B **57**, 1505 (1998).

[48] Q. Zhao and H.J. Kulik, J. Chem. Theory Comput. **14**, 670 (2018).

[49] Z. Hu and H. Metiu, J. Phys. Chem. C **115**, 5841 (2011).

[50] H.J. Kulik, J. Chem. Phys. **142**, 240901 (2015).

[51] A. Einstein, Ed. by R. Furth A. D. Cowper, Dover, New York, (1956).

[52] R.R. Heikes and W.D. Johnston, J. Chem. Phys. **26**, 582 (1957).

[53] A. Togo and I. Tanaka, Scr. Mater. **108**, 1 (2015).

[54] A. Walsh, Y. Yan, M.N. Huda, M.M. Al-Jassim, and S.-H. Wei, Chem. Mater. **21**, 547 (2009).

[55] A. Walsh, D.J. Payne, R.G. Egdell, and G.W. Watson, Chem. Soc. Rev. **40**, 4455 (2011).

[56] N. Lu, L. Li, D. Geng, and M. Liu, Org. Electron. **61**, 223 (2018).

[57] C. Deibel, A. Wagenpfahl, and V. Dyakonov, Phys. Rev. B **80**, 075203 (2009).

[58] S. Selim, E. Pastor, M. García-Tecedor, M.R. Morris, L. Francàs, M. Sachs, B. Moss, S. Corby, C.A. Mesa, S. Gimenez, A. Kafizas, A.A. Bakulin, and J.R. Durrant, J. Am. Chem. Soc. **141**, 18791 (2019).

[59] J.K. Cooper, S.B. Scott, Y. Ling, J. Yang, S. Hao, Y. Li, F.M. Toma, M. Stutzmann, K. V. Lakshmi, and I.D. Sharp, Chem. Mater. **28**, 5761 (2016).

[60] T.W. Kim, Y. Ping, G.A. Galli, and K.S. Choi, Nat. Commun. **6**, 1 (2015).

[61] H. Seo, Y. Ping, and G. Galli, Chem. Mater. **30**, 7793 (2018).

[62] C. Ding, J. Shi, D. Wang, Z. Wang, N. Wang, G. Liu, F. Xiong, and C. Li, Phys. Chem. Chem. Phys. **15**, 4589 (2013).

[63] S. Kokott, S. V. Levchenko, P. Rinke, and M. Scheffler, New J. Phys. **20**, 033023 (2018).

[64] Y. Hermans, A. Klein, K. Ellmer, R. Van De Krol, T. Toupance, and W. Jaegermann, J. Phys. Chem. C **122**, 20861 (2018).

[65] M.N. Huda, M.M. Al-Jassim, and J.A. Turner, J. Renew. Sustain. Energy **3**, 053101 (2011).

[66] R.A. Marcus and N. Sutin, Biochim. Biophys. Acta **811**, 265 (1985).

[67] R.A. Marcus, Rev. Mod. Phys. **65**, 599 (1993).

[68] N.A. Deskins and M. Dupuis, Phys. Rev. B **75**, 195212 (2007).

[69] J.B. Varley, A. Janotti, C. Franchini, and C.G. Van De Walle, Phys. Rev. B **85**, 081109 (2012).

[70] A.J. Bosman and H.J. van Daal, Adv. Phys. **19**, 1 (1970).

[71] C.W. Chen, Y.C. Lin, C.H. Chang, P. Yu, J.M. Shieh, and C.L. Pan, IEEE J. Quantum Electron. **46**, 1746 (2010).

[72] T. Makino, A. Tsukazaki, A. Ohtomo, M. Kawasaki, and H. Koinuma, Jpn. J. Appl. Phys. **45**, 6346 (2006).

[73] W. Qiu, S. Xiao, J. Ke, Z. Wang, S. Tang, K. Zhang, W. Qian, Y. Huang, D. Huang, Y. Tong, and S. Yang, Angew. Chemie **58**, 19263 (2019).

Chapter 6

Aliovalent doping mechanism of suppressing polaron formation: A case study of Ca & Sr doping in $BiVO_4$

Hori Pada Sarker[1] *and Muhammad N. Huda*[1*]

[1]Dept. of Physics, The University of Texas at Arlington

Arlington, Texas 76019, United States of America

In preparation for publication at:

Chemistry of Materials

[*] Corresponding author: huda@uta.edu

Abstract

The deep localized trapping states within the band gap act as a major barrier towards designing transition metal oxide or perovskite based renewable energy technologies as well as other optoelectronic devices. The trapping states adversely affect the carrier transport by restricting the mobility of free carriers, and sometimes they also behave as a recombination center for carrier recombination. So, in order to design efficient devices, these trapping states have to be eliminated from the band gap. In this study, we have applied a conventional yet very powerful aliovalent doping technique to eliminate the sub-band gap states. We have used the prominent H_2O splitting photocatalyst, $BiVO_4$ as our model system. In $BiVO_4$, O-vacancy mediated bound polarons form deep trapping states (V^{4+}- state) within the band gap. The substitutional doping of group-II elements (Ca^{2+} or Sr^{2+}) in Bi^{3+} position effectively suppress the polaron formation and hence eliminates the sub-band gap trapping states. Ca^{2+} or Sr^{2+} substitutional doping not only suppress the V^{4+}- trapping state but also brings back the shifted Fermi level (E_F) to the top of valence band maxima. In this study, we have demonstrated the suppression of polaron formation as well as elimination of trapping states by the state of the art first principles density functional theory (DFT). The detail electronic structure calculations as well as optical absorption plots clearly showed the complete elimination of sub-band gap states by (Ca^{2+} or Sr^{2+}) aliovalent doping. So, this study suggests that aliovalent doping can be a general technique to handle the sub-band gap trapping states for other materials as well.

6. 1. Introduction

Sustainable and renewable energy producing technologies such as solar cell[1–3], PEC water splitting[4,5], battery[6,7], supercapacitor[8,9] etc. will play a major role in controlling the 21st century global energy landscape. Most of these technologies are hinged on metal oxide or perovskite based semiconducting materials. The efficiency of these devices is mostly dependent on the transport behavior of the semiconducting materials among other factors. Until now, the efficiency of renewable energy technologies lacks far behind from the predicted theoretical values[7,10–12]. For an example, $BiVO_4$ (one of the champion materials for PEC water splitting) based stand-alone water splitting PEC reactor so far reached only ~ 1.1% efficiency[10], even though theoretically it can reach up to 10% efficiency[13,14]. The reason behind the efficiency lack is primarily the poor transport of charge carriers (electrons/holes). In metal oxide or perovskite-based semiconductors, defects play a crucial role in determining their charge transport behavior[12,15–18]. In general, defect introduces crystal asymmetry, and in return, crystal asymmetry modifies the orbital configuration in the electronic structure. Any changes in the orbital configuration eventually affect the transport of free carriers through these orbitals. There are several types of defects (i.e., vacancy, interstitial, anti-site, substitutional doping etc.) commonly found in the semiconducting materials. Among them, some of the defects create shallow defect level while others generate deep level within the band gap of the material. Shallow defect levels are those which lies just below or above the conduction band minima (CBM) or valence band maxima (VBM), respectively. For shallow defects, $\Delta E \leq K_B T$, where , ΔE define the energy difference between the band edge and defect state, $K_B T (\sim 25\ meV$ at room temperature) is the thermal energy and K_B is the Boltzmann constant. In most cases, shallow defect levels are harmless and sometimes they are even considered

beneficial because they give extra carriers (electron/hole) to the conduction or valence band. On the other hand, deep localized level ($\Delta E > K_B T$) resides somewhere between the band gap and free carriers fall into these energetically more favorable state and get trapped, and hence, the transport of the trapped carriers become restricted. Detrapping process of trapped carriers from the deep localized state is way more difficult than the shallow states, thus these deep level trapping states sometime facilitate non-radiative recombination pathway to the carrier recombination. That is why deep level localized defect states are considered detrimental for semiconductor materials and they are highly unwanted.

Among other available defects, O-vacancy defect is more prevalent in metal oxides and perovskite materials[19–23]. One single O-vacancy leads to transfer two extra electrons and these extra electrons either spread out through the whole cell and create partially filled shallow bands just below the conduction band minima (signature for n-type character) or become localized to the nearby cationic sites as polaron and form deep level polaronic state below the CBM. It was reported that in $BiVO_4$[16], $SrTiO_3$[24] as well as other metal oxides[15,20,25], O-vacancy form deep level polaronic state and hinder the carrier transport, and hence, limit the quantum efficiency. In this study, we have applied aliovalent doping mechanism as an effective way to suppress the formation of polaron, hence, elimination of deep localized defect level within the band gap of material. We have used $BiVO_4$ as our model system. It is well documented that $BiVO_4$ forms polaron[26–30] and polaron limit the efficiency by restricting the splitting of quasi-Fermi level[31]. Hosung Seo et.[16] al. theoretically and Shababa Selim et. al.[32] experimentally demonstrated the O-vacancy mediated polaron formation in $BiVO_4$. Another experimental study by Weitao Qiu et. al.[32] demonstrated two-fold performance enhancement of $BiVO_4$ PEC cell by restricting the formation of O-vacancy and hence freeing the O-vacancy mediated bound polaron. In this study,

we have calculated electronic structure of O-vacancy defective $BiVO_4$. We have found that O-vacancy generates deep defect state (~0.6 eV below the conduction band) within the band gap and the extra electrons coming from O-vacancy become trapped to the nearby V atoms and form polaron. The detail is discussed in the results and discussion section.

In this study, we have substitutionally doped group-II elements- Ca/Sr in place of Bi position. Bi has Bi^{3+} oxidation state in $BiVO_4$ and on the other hand Ca/Sr has Ca^{2+}/Sr^{2+} oxidation state. So, there is +1 oxidation state difference if Ca/Sr is substituted in Bi position. Due to a very little mismatch of ionic radius of Ca^{2+}(0.99 Å) and Sr^{2+}(1.13 Å) with Bi^{3+} (1.11 Å)[33], Ca/Sr has high solubility and act as an effective aliovalent dopant in $BiVO_4$. So, hypothetically, a single Ca or Sr atom doping in Bi position will create a hole state just above the VBM. We have shown that indeed Ca/Sr doping produce shallow hole state just above the VBM (see supplementary figure 4). Later, we have doped Ca/Sr in O-vacancy defective $BiVO_4$ supercell. Since, one single O-vacancy generates two extra electrons, we have substitutionally doped two Ca/Sr in Bi position in different configurations to counterbalance the extra electrons. Total energy calculations show that 2Ca atom doping near to O-vacancy and 2Sr doping far from O-vacancy configurations are the most stable Ca/Sr doping configurations in O-vacancy defective $BiVO_4$. 2Ca/Sr doping completely eliminates the deep localized state originated from the O-vacancy (see figure 4). O-vacancy moves the Fermi level (E_F) in higher energy direction toward the conduction band. 2Ca/Sr aliovalent doping brings back the shifted Fermi level (E_F) toward the top of the valence band maxima (VBM). 2Ca/Sr aliovalent doping further pushes the band gap to be more direct nature direction. We have further justified the elimination of deep localized state by 2Ca/Sr aliovalent doping by calculating the optical absorption (see figure 5) as well as doping of Ca/Sr directly to polaron containing $BiVO_4$ supercell. Both of these observation further confirms the

complete elimination of the O-vacancy/polaron generated deep localized sub-band gap state within the band structure. The elimination of deep localized state will be reflected in the observe photocurrent. Experimental studies reported increase of photocurrent in $BiVO_4$ by few folds after Ca doping[34]. Similar type of localized state elimination and photocurrent increment in $SrTiO_3$ by Al aliovalent doping is also reported by Zeqiong Zhao et. al.[24] Very recently, Tsuyoshi Takata et. al.[35] also reported the enhancement of quantum efficiency by 96% of Al doped $SrTiO_3$.

In this study, we have presented a detail electronic structure calculations to understand the atomistic level mechanism of elimination of deep localized electronic state in $BiVO_4$ via Ca or Sr aliovalent doping. This paper is organized as follows: we first briefly outline the computational technique, followed by the results and discussions, and finally draw the conclusions. Overall, this study suggests a general yet powerful technique to control the trapping state and hence a way to design highly effective semiconductor materials for renewable energy applications.

6. 2. Computational Methodology

We have performed first principles density functional theory (DFT) calculations using the Vienna ab initio Simulation Package (VASP) code[36]. Within this framework, the exchange and correlations were described by the PBE (Perdew-Burke-Ernzerhof)[37] functional within the generalized gradient approximation (GGA). For ion-electron interactions, projector-augmented wave (PAW) method[38] was employed. The 1st Brillouin zone (BZ) was sampled using the Mohkhorst-Pack (MP) scheme into a 3×3×5 k-point grid for geometric optimization, and higher k-point gird has been used for density of states (DOS) and polaronic state calculations. A 96 atoms supercell with periodic boundary conditions in all three directions were used to simulate $BiVO_4$. For geometric optimization, the supercell was fully relaxed until the residual forces on

all the constituent atoms become smaller than 0.01 eV $Å^{-1}$. A plane wave energy cut-off of 500 eV was used throughout the whole calculations, which gave a well converged results.

To model electron polaron, one extra electron was added to the relaxed $BiVO_4$ supercell. In addition of adding an extra electron, to produce polaronic solution, we initially applied a small perturbation around a selected VO_4 tetrahedron to break the lattice symmetry prior to structural relaxation. To ensure the charge neutrality of the supercell, a compensating homogeneous background counter charge was also added.

To model O-vacancy defected $BiVO_4$ supercell, we take out one O-atom from the relaxed supercell. Finally, Ca or Sr dopped BiVO4 were simulated by replacing Bi-atoms by Ca or Sr atoms within the crystal lattice.

6. 3. Results and Discussions

6. 3. 1. Electronic Structure of polaron in pristine $BiVO_4$

$BiVO_4$ crystallizes into monoclinic clinobisvanite scheelite type structure at ambient condition. Bi and V atoms form alternate layers of VO_4 tetrahedron and slightly distorted BiO_8 dodecahedron. The slight distortion in BiO_8 dodecahedron makes the monoclinic scheelite phase of $BiVO_4$ thermodynamically more favorable and photo-catalytically more active than the other polymorphs of $BiVO_4$. The valence band of $BiVO_4$ is mainly O 2p-orbitals character but there is significant contribution from stereochemically active Bi 6s-orbitals just below the Fermi level. The conduction band is predominantly composed of localized V 3d-orbitals. There is also a little contribution from O 2p – Bi 6p hybridized orbitals just above the conduction band minima (CBM). In fact, the photo-catalytic active behavior of monoclinic scheelite type $BiVO_4$ stems from the mixing of coupled Bi 6s – O 2p anti-bonding orbitals near the Fermi level with Bi 6p

unoccupied orbitals in the conduction band. The crystal geometry as well electronic structure of pristine $BiVO_4$ were presented in the supplementary figure 1.

Due to the presence of highly localized V 3d-orbitals at CBM as well as strong carrier-lattice interaction, some of the conduction electrons generated by photo excitation or defect i.e., O-vacancy in case of $BiVO_4$, get trapped at V-sites and form electron polaron[27–30,32]. Trapping of electron at V-sites cause them to change their oxidation state from formerly $V^{5+} \rightarrow V^{4+}$. Formation of polaron at V-site by electron trapping generates a deep electronic state below the CBM. This deep polaronic state behaves as a recombination center for hole and plays a crucial

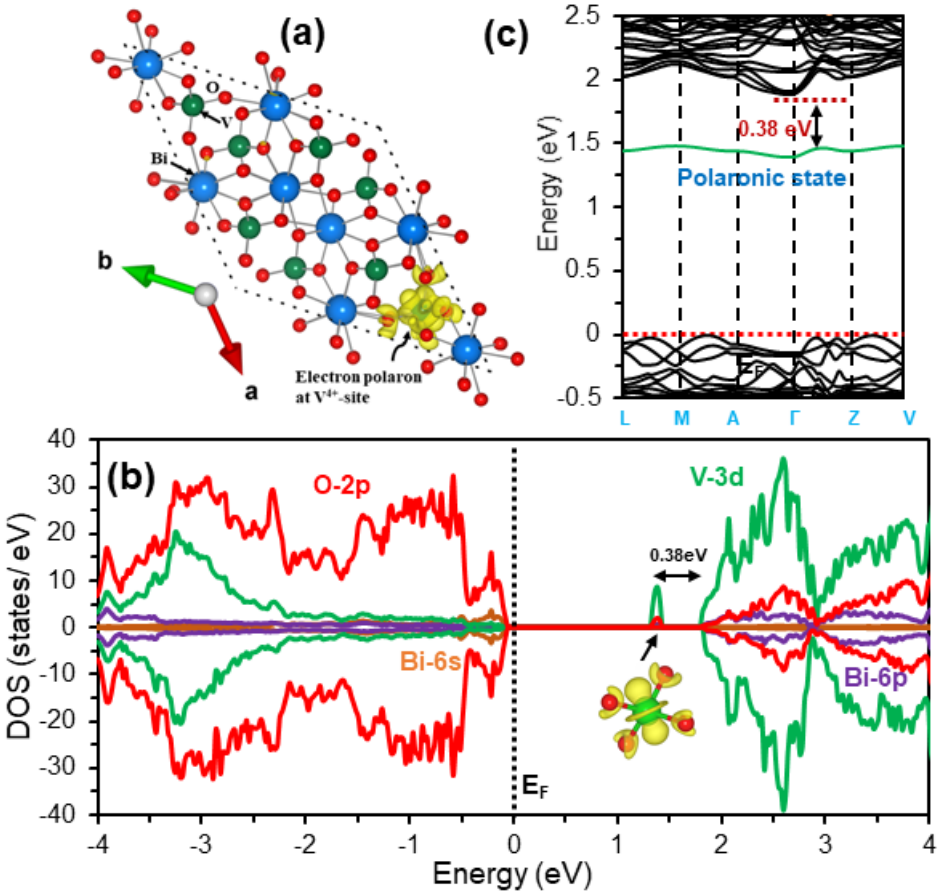

Figure-6. 1: (a) Iso-charge surface density of extra electron as polaron at V-site in pristine $BiVO_4$. (b) The orbital projected density of states of polaronic configuration of $BiVO_4$. The inset figure shows the V-$3d_z^2$ orbital character of electron polaron. (c) The electronic band structure of polaronic configuration of $BiVO_4$. The polaronic state is showed as green band below the conduction band minima.

role in PEC reaction kinetics. Very recently, Shababa et. al.[32] identified the deep electron polaronic state in bulk $BiVO_4$ as a hole trapping center. In this study, we have calculated electron polaron formation in pristine $BiVO_4$. To form electron polaron, we have added an extra electron to a relaxed supercell and perturbed a selected VO_4 tetrahedron to break the lattice symmetry in order to facilitate the carrier localization. Figure 1(a) shows the charge density of localized electron at V-site. Figure 1(b-c) shows the orbital projected density of states (DOS) and electronic band structure of the electron polaronic configuration of $BiVO_4$. As shown in DOS and iso-charge density in the inset figure, the extra electron fills the lowest energy unoccupied V-$3d_z^2$ orbital below the CBM. It is important to note that the polaronic state is highly nondispersive which indicates the heavy effective mass nature of polarons. The calculated electron polaronic state lies ~0.38 eV below the CBM as shown in the DOS and band structure (see figure 1(b-c)). A recent in-situ photoelectron spectroscopy experiment reported[31] the position of deep polaronic state at ~0.3 eV below CBM. Another theoretical study[26] also predicted that the polaronic state lies at ~ 0.3 eV below CBM. This present study overestimates the polaronic state position by ~0.08 eV compared to the reported values, but the calculated value is well comparable within the DFT limit.

6. 3. 2. Electronic Structure of O-vacancy defective $BiVO_4$

O-vacancy is an omnipresent defect in transition metal oxides[12,17,20,22,24,33], and $BiVO_4$ is not an exception. O-vacancy is thermodynamically stable in $BiVO_4$ which has been demonstrated by this study (see SI figure 2) as well as other studies[33]. Since, oxygen has O^{2-} oxidation state in $BiVO_4$, O-vacancy is an n-type dopant. So, a single O-vacancy will generate two extra electron in O-vacancy defective $BiVO_4$ crystal lattice. In this study, we have created a single O-vacancy by removing one O-atom from a 96-atoms supercell and relax the supercell completely. Figure

2(a-b) shows the orbital projected density of states (DOS) and electronic band structure of O-vacancy defective $BiVO_4$. Typically, O-vacancy creates shallow donor level at the bottom of the conduction band and responsible for n-type character of materials[39]. But in $BiVO_4$, the O-vacancy defect state is rather a deep state as shown in figure 2(a-b). The calculated defect state is located ~0.59 eV below the conduction band. Cooper et. al.[40] and Kim et. al.[41] reported that O-vacancy defect state is indeed a deep state. By using photo luminescence spectroscopy, Cooper et.

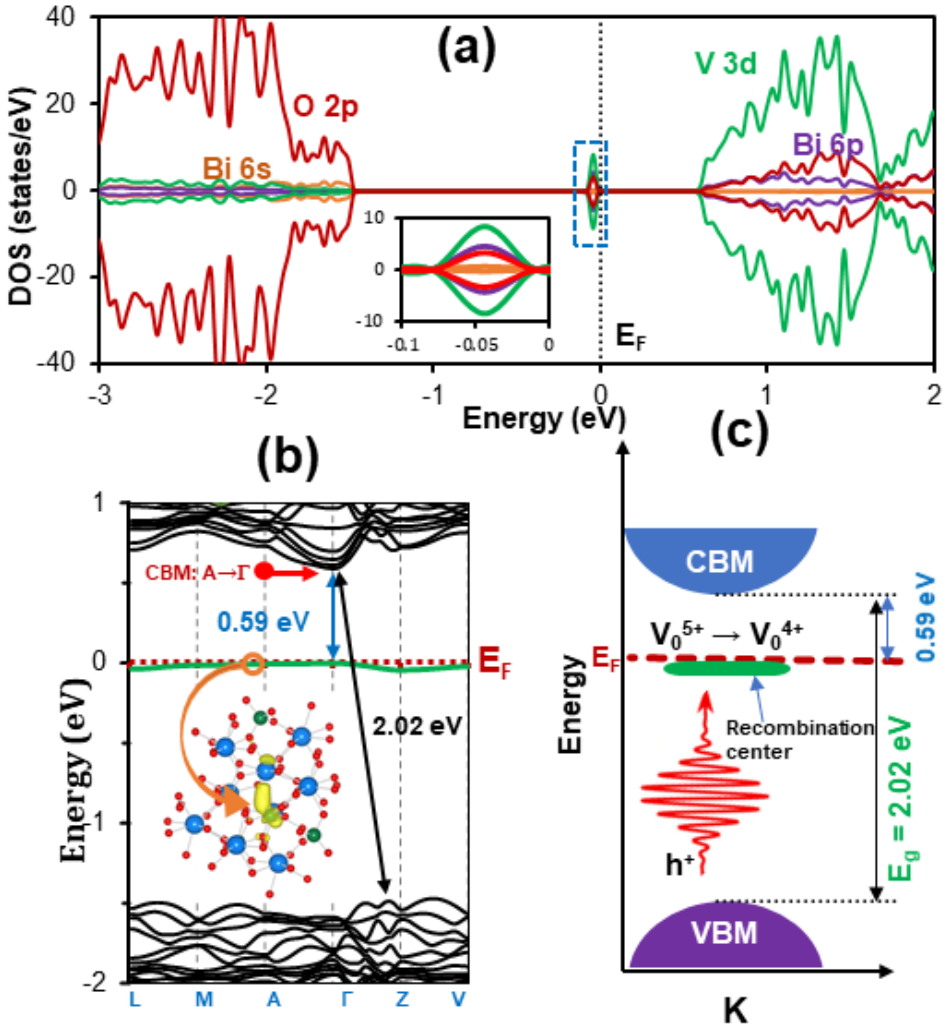

Figure-6. 2: (a) The orbital projected density of states of O-vacancy defective $BiVO_4$. The inset figure shows the amplified view of the defect state (b) The electronic band structure of O-vacancy defective $BiVO_4$. The defective band is shown by the green band and the inset figure shows the band decomposed charge density of the defect band. (c) Schematic diagram of the

electronic structure. The mid gap state coming from O-vacancy behaves like an electron polaronic state as well as hole recombination center, which is shown by the green bold line.

al.[40] measured the position of defect level at ~ 0.6 eV below the conduction band. In fact, the calculated defect level position is pretty much similar as measured by Cooper et. al.[40] The argument of deep defect level from O-vacancy is also consistent with the calculation of Hosung Seo et. al.[16]. As a side note, the position of defect state w.r.t. CBM is comparable with the position of polaronic state in pristine $BiVO_4$ (see figure 3). The defect level is ~0.6 eV below the conduction band means that it will take ~0.6 eV ionization energy to generate free carriers from defect level to the conduction band which is very difficult to do. Hence, O-vacancy defect state may not donate electrons to the conduction band as free carriers at ambient conditions. Rather the defect state will behave as an electron polaronic state which makes O-vacancy an effective n-type dopant. As shown in figure 2(a), the extra electrons coming from O-vacancy fill the unoccupied V 3d-orbitals below the conduction band. Moreover, band decomposed charge density of the defect band as shown in the inset figure of figure 2(b) shows that instead of spreading out throughout the whole cell, the charge density (coming from O-vacancy) of the extra electron become localized at a single V-atom nearby to the O-vacancy. The shape of the iso-charge surface shows that the extra electron fills the lowest energy V-$3d_z^2$ orbital. Additionally, the defect band is, as shown in the band structure, highly non-dispersive. All the above-mentioned features indicate that O-vacancy defect level acts as polaronic state in $BiVO_4$. Very recently, Shababa Selim et. al.[32] showed that extra electrons generated by O-vacancy in $BiVO_4$ reduce V-atoms ($V^{5+} \rightarrow V^{4+}$) nearby to the defect center and form electron polaron. By using five complementary electrochemical, thermal, and all-optical techniques, they also showed that polaronic state originates from O-vacancy act like an active recombination center for the hole carriers. The formation of polaron by O-vacancy in Fe_2O_3 is also demonstrated by Tyler J.

Smart et. al.[15]. It is worthy to mention that O-vacancy has the tendency to make the indirect gap of $BiVO_4$ into a direct one as well as it reduces the band gap by 0.8 eV with respect to pristine gap (see figure 2b).

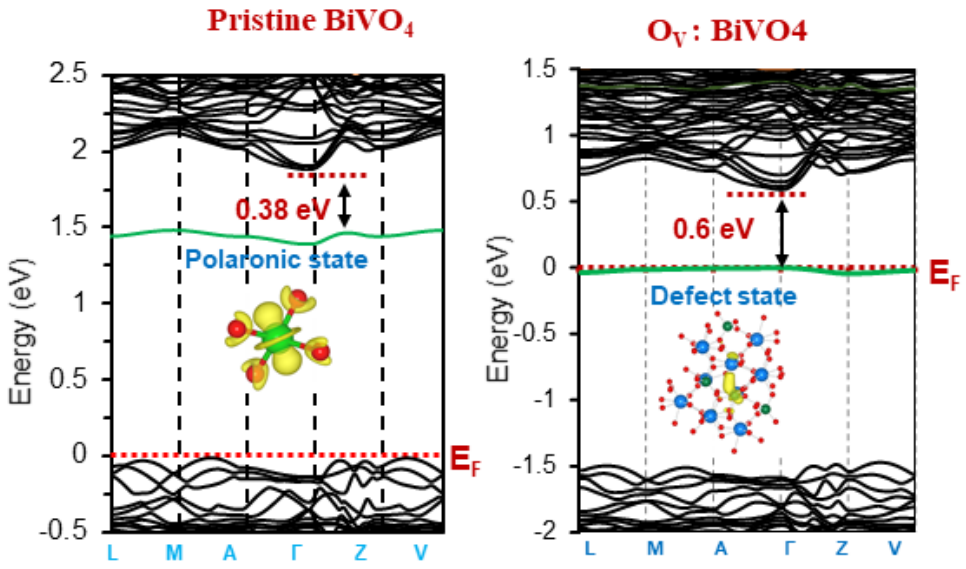

Figure-6. 3: Electronic band structure of pristine $BiVO_4$ in polaronic configuration and O-vacancy defective $BiVO_4$. The polaronic state as well as O-vacancy defective states are denoted as green band.

6. 3. 3. Aliovalent doping- Ca and Sr substitutional doping in $BiVO_4$

In $BiVO_4$, Bi atoms have Bi^{3+} oxidation state. The substitutional doping of group II-elements [in this case Ca (Ca^{2+}) and Sr (Sr^{2+})] in place of Bi atoms falls into the category of aliovalent doping. Due to a little mismatch of the ionic radius of Ca^{2+} (0.99 Å) and Sr^{2+} (1.13 Å) with Bi^{3+} (1.11 Å) ion, Ca and Sr supposed to show high solubility in $BiVO_4$. In fact, Sr supposed to show higher solubility than Ca. In a recent publication written by Wan-Jian Yin et. al.[33] demonstrated that Ca and Sr indeed have high solubility, and Sr is more soluble than Ca in $BiVO_4$. They have used first principles density functional theory calculations of defect formation energy. Yao et. al.[42] and Sameera et. al.[43] experimentally synthesized $Ca_xBi_{1-x}V_{1-x}Mo_xO_4$ and $Ca_xBi_{1-x}V_{1-x}W_xO_4$ solid solution, respectively, and found that Ca had a variable range of solubility in $BiVO_4$. Very

recently, Fatwa F. Abdi et. al.[34] successfully synthesized Ca doped $BiVO_4$ (Ca_{Bi}: $BiVO_4$) via spray pyrolysis technique. In this study, we have simulated Ca_{Bi}: $BiVO_4$/ Sr_{Bi}: $BiVO_4$ by replacing one Bi atom by Ca/Sr atom and assumed that Ca/Sr are soluble in $BiVO_4$ without further calculations to check their solubility in $BiVO_4$. Before doing the electronic structure calculations, we have allowed the internal degrees of freedom of the supercell to relax completely. After complete relaxation, we have found a minute volume change of supercell doped with Ca/Sr. Ca doping decreases the supercell volume by only 0.41% and on the other hand, Sr doping increases the volume by only 0.16% with respect to pristine supercell volume (see SI figure 3). The crystal geometry of Ca/Sr doped $BiVO_4$ remains almost unchanged compared to pristine one, and this also reflected in the Bi-O and V-O bonding environment. Bi-O and V-O bond lengths remains almost same as they were in pristine cell. Ideally, this means that the band edges will remain unperturbed in Ca/Sr doped BiVO4, except inclusion of an acceptor level just above the valence band maxima. Since, Ca/Sr has +2 oxidation state, Ca/Sr substitutional doping in place of Bi position will act like a p-type dopant. Wan-Jian Yin et. al.[33] found Ca/Sr to be very shallow acceptor with transition energies smaller than 0.1 eV and they have very small formation energies under O-rich growth condition. We have also calculated the electronic structure (DOS and band structure) of Ca/Sr doped $BiVO_4$. We found that Ca/Sr doping in Bi-place generates a shallow acceptor level just above the valence band maxima, which justify the observation of Wan-Jian Yin et. al.[33] (detail in SI figure 4) . So, Ca/Sr will serve as a good candidate for p-type doping in $BiVO_4$. We also found that Ca/Sr doping reduces the band gap by 0.02 eV compared to pristine gap and the former position of CBM at A-point changes to Γ-point which tends to make the indirect gap into direct one

6. 3. 4. Electronic structure of $2Ca_{Bi} + O_V$: $BiVO_4$ and $2Sr_{Bi} + O_V$: $BiVO_4$

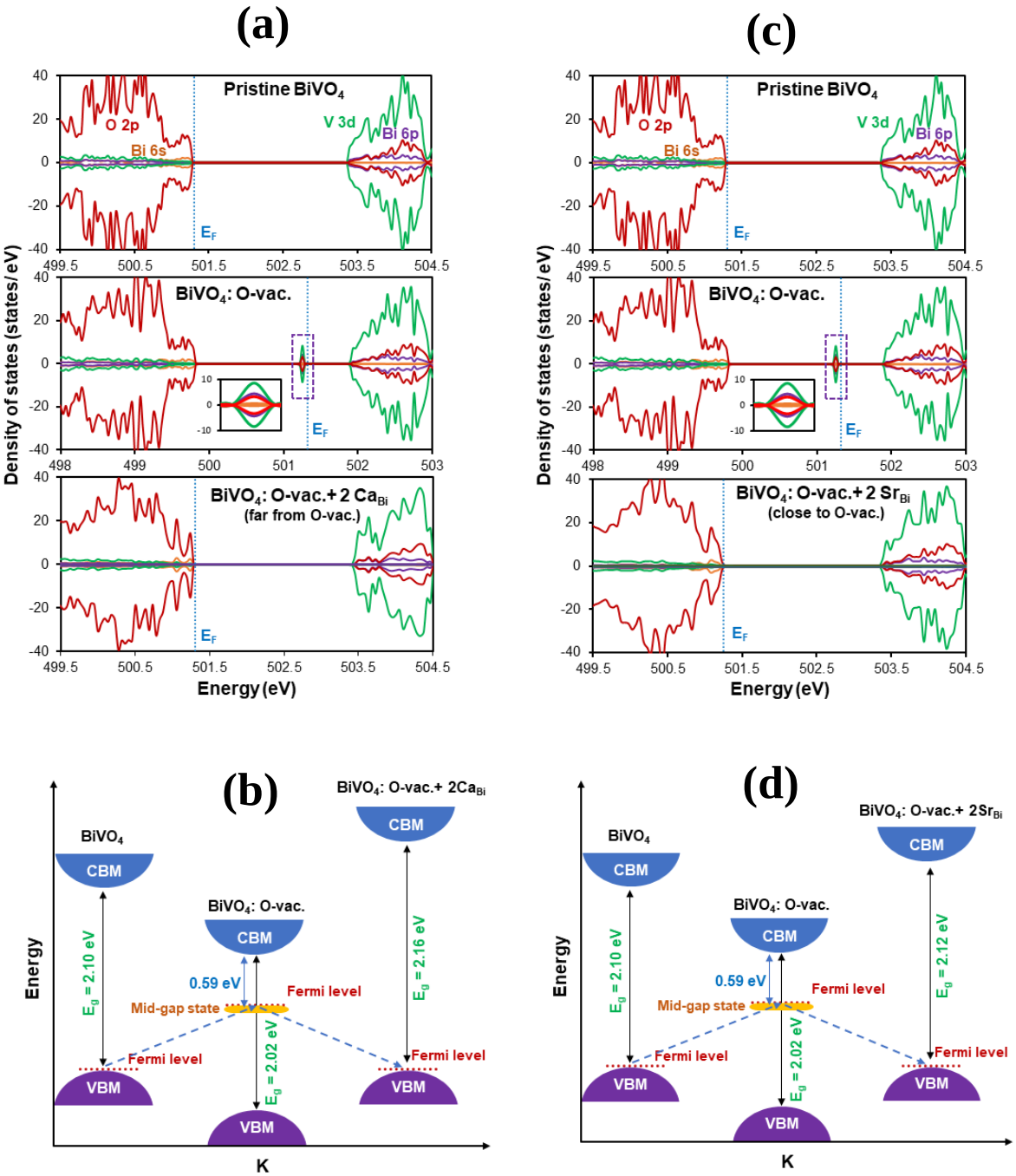

Figure-6. 4: (a) Comparison of Density of states of $2Ca_{Bi} + O_V$: $BiVO_4$ with pristine and O-vacancy defective $BiVO_4$. (b) Schematic diagram of electronic structure of $2Ca_{Bi} + O_V$: $BiVO_4$, pristine and O-vacancy defective $BiVO_4$. (c) Comparison of Density of states of $2Sr_{Bi} + O_V$: $BiVO_4$ with pristine and O-vacancy defective $BiVO_4$. (d) Schematic diagram of electronic structure of $2Sr_{Bi} + O_V$: $BiVO_4$, pristine and O-vacancy defective $BiVO_4$. The Fermi level is defined as the zeroth energy level and the O 1s-core level energy was taken as reference.

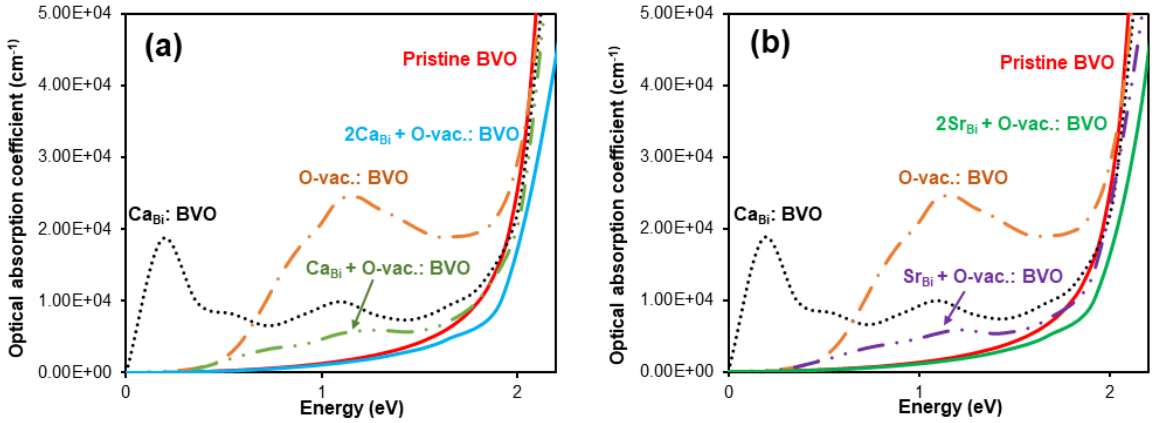

Figure-6. 5: (a-b) Optical absorption plot of $2Ca_{Bi}$ + O_V: $BiVO_4$ and $2Sr_{Bi}$ + O_V: $BiVO_4$ configurations with others. All other configurations have optical peak somewhere within the band gap except these two. These two configurations have optical absorption behavior similar like pristine $BiVO_4$.

A single O-vacancy generates two extra electrons in the crystal lattice of $BiVO_4$. These electrons become localized to V atoms nearby to the vacancy site, and as a consequence, reduces V atoms from $V^{5+} \rightarrow V^{4+}$ oxidation state. In this process, a sub-band gap defect state has been created and this defect state can be treated as a polaronic state. This type of mid-gap state behaves like a trapping state or a recombination center and adversely affects the transport behavior of materials. For example- the quantum efficiency of PEC water splitting by $SrTiO_3$ photocatalyst is greatly reduced by the sub-band gap polaronic trapping state created by O-vacancy[24]. So, an effective mechanism of suppressing sub-band gap state is highly sought. It was reported that aliovalent doping with suitable dopant can suppress sub-band gap defect state. Recently, Zeqiong Zhao et. al.[24] demonstrated the suppression of Ti^{3+} sub-band gap state orginated from O-vacancy in $SrTiO_3$ by Al doping. Another study by Tsuyoshi Takata et. al.[35] reported an overall water splitting at an external quantum efficiency (EQE) of upto 96% by using Al doped modified $SrTiO_3$ photocatalyst. In this study, we doped group II-elements- Ca (Ca^{2+}) and Sr (Sr^{2+}) in Bi (Bi^{3+}) position. Since, the oxidation state difference between Bi^{3+} and Ca^{2+}/Sr^{2+} is +1, a single

Ca/Sr doping generates a hole in $BiVO_4$ crystal lattice (see SI figure 4). In contrast of Ca/Sr doping, a single O-vacancy creates two extra electrons in $BiVO_4$ crystal lattice. So, to counter balance two extra electrons coming from a single O-vacancy, we doped 2Ca/2Sr atoms in Bi position. We have found that 2Ca/2Sr substitutional doping in Bi place completely suppress the V^{4+} sub-band gap trapping state within a O-vacancy defective $BiVO_4$ cell (see the middle and lower pannel of figure 4(a) and 4(c)). Furthermore, 2Ca/2Sr doping brings the shifted Fermi level of O-vacancy defective $BiVO_4$ back at the top of valence band as it in the pristine case (see figure 4). To justify the suppression of V^{4+} sub-band gap state by 2Ca/2Sr doping, we further calculated the optical absorption of different defective configurations of $BiVO_4$ (see figure 5(a-b)). As shown in figure 5 (a-b), all the defective configurations of $BiVO_4$ show optical absorption peak somewhere within the band gap except $2Ca_{Bi}$ + O-vac.: $BiVO_4$ and $2Sr_{Bi}$ + O-vac.: $BiVO_4$ configurations. These two configurations have very similar optical absorption behavior like pristine $BiVO_4$. This further justify the claim of suppression of V^{4+} sub-band gap state which is clearly shown in the DOS plot (figure 4) as well as band structures (see SI figure 5). Since, Ca/Sr doping in Bi position supply extra hole, Ca/Sr acts like an antidopant[44] for the electron doped O-vacant $BiVO_4$. As a consequence, the extra electron coming from O-vacancy get annihilated by the extra hole generated from Ca/Sr doping. The only change is happened in the band gap of these two configurations, which got little bit blue shifted with respect to the pristine gap. It is important to note that Ca/Sr s and p-orbitals contribute to both valence and conduction band edges eventhough their contribution is very small. In the conduction band edge, s and p orbitals are highly hybridized than the valence band edge (see SI figure 6). Finally, to check whether Ca/Sr doping could suppress the polaron formation within an electron doped polaronic configuration of pristine $BiVO_4$, we doped one Ca/Sr atom close to the polaronic site

and let the system relax completely. We found that Ca/Sr doping comletely delocalize the polaronic charge density throughout the whole cell (see figure 6). Along with the polaronic charge density, the extra hole coming from Ca/Sr doping also become delocalized within the entire cell.

This clearly indicates that Ca/Sr doping suppress the sub-band gap polaronic state via counter balancing the extra charge. Very recently, Fatwa F. Abdi et. al.[34] successfully syntheszied Ca doped $BiVO_4$ and reported two fold increase in photocurrent. They proposed the photocurrent enhancement by out-diffusion of Ca atoms during synthesis process and subsequent formation of spontaneous p-n junction within the bulk. Their hypothesis regaring the photocurrent increament

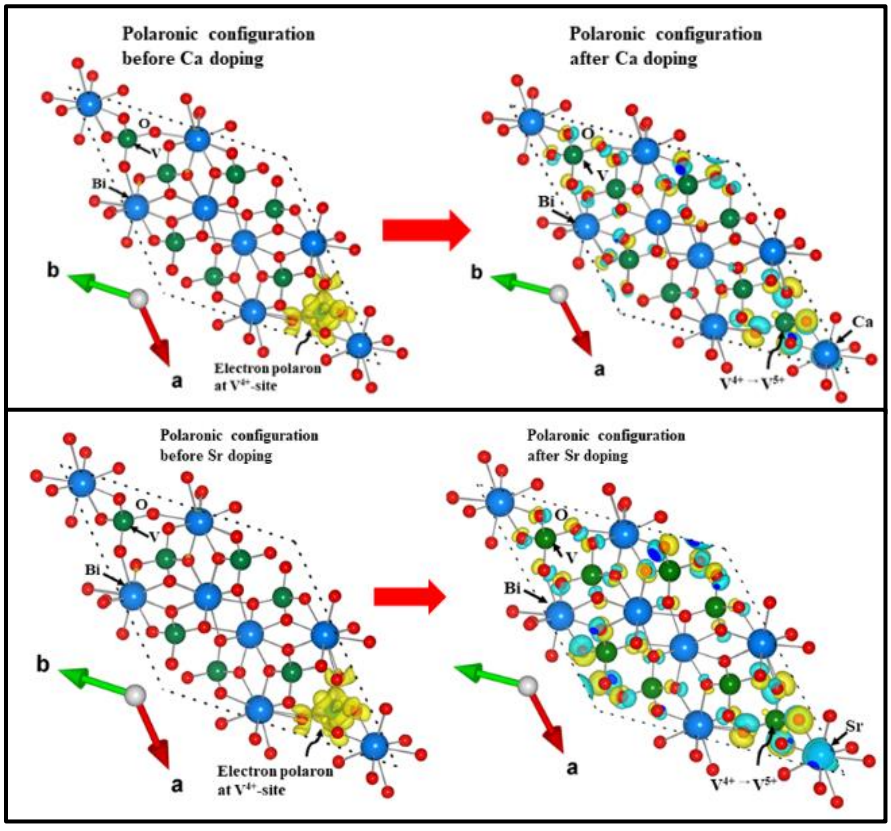

Figure-6. 6: The charge density plot for Ca/Sr doping in electron doped polaronic configuration of $BiVO_4$. The yellow iso-surface indicates electron charge density and sky blue iso-surface indicates hole charge density.

may not be quite accurate. Firstly, Ca is a highly soluble dopant in $BiVO_4$ and there should not be any Ca diffusion in the sample. Secondly, they might have missed to detect the signature of sub-band gap state created by O-vacancy. They have mentioned that their prepared sample is n-type, so the n-type conductivity is most probably coming from O-vacany. If O-vacancy mediated n-type conductivity scenerio is true, then Ca doping actually suppressed the formation of sub-band gap states coming from O-vacancy and facilitated the photocurrent enhancement in Ca doped $BiVO_4$.

Conclusion

In summary, we have used density functional theory (DFT) calculations to understand the aliovalent doping mechanism of sub-band gap state elimination or polaron formation suppression in $BiVO_4$. We have found that aliovalent doping of Ca^{2+}/Sr^{2+} in $BiVO_4$ eliminates the deep V^{4+} polaronic state completely and brings the Fermi level back to the top of the valence band maxima. Electronic structure (DOS and band structure) along with optical calculations clearly show no mid-gap trapping state within the band gap. The overall band structure remains same except the band gap value and type. Ca^{2+}/Sr^{2+} doping increases the band gap by ~(1-3)% compared to the calculated pristine gap and changes the CBM from A to Γ-point in the band structure, and hence pushes the band gap to be more direct in nature as opposed to the indirect gap in pristine $BiVO_4$. Ca^{2+}/Sr^{2+} doping in polaron containing $BiVO_4$ configuration further shows that Ca^{2+}/Sr^{2+} doping not only suppress the polaron formation by counterbalancing extra charge but also delocalize the charge carrier throughout the entire cell. This further confirms the elimination of sub-band gap polaronic state by Ca^{2+}/Sr^{2+} aliovalent doping. Overall, these findings suggest that aliovalent doping can be a potential means of controlling trapping states, and hence improving the charge transport in metals oxides and other materials.

Acknowledgement

M.N.H. was supported by the national Science Foundation (Award No. DMR-1609811). M.N.H. and H.P.S. thank the Texas Advance Computing Center (TACC) (Austin-TX, USA) for their computational needs.

Competing Financial Interest

The authors declare no competing financial interests

Key words

$BiVO_4$, Polaron, Aliovalent doping, Trapping state, Density Functional Theory (DFT)

References:

[1] N.S. Lewis, Science (80-.). **351**, 353 (2016).

[2] P.K. Nayak, S. Mahesh, H.J. Snaith, and D. Cahen, Nat. Rev. Mater. **4**, 269 (2019).

[3] T.D. Lee and A.U. Ebong, Renew. Sustain. Energy Rev. **70**, 1286 (2017).

[4] J. Willkomm, K.L. Orchard, A. Reynal, E. Pastor, J.R. Durrant, and E. Reisner, Chem. Soc. Rev. **45**, 9 (2016).

[5] M. Grätzel, Nature **414**, 338 (2001).

[6] J. Janek and W.G. Zeier, Nat. Energy **1**, 1 (2016).

[7] N. Nitta, F. Wu, J.T. Lee, and G. Yushin, Mater. Today **18**, 252 (2015).

[8] Z.S. Iro, C. Subramani, and S.S. Dash, Int. J. Electrochem. Sci. **11**, 10628 (2016).

[9] S. Najib and E. Erdem, Nanoscale Adv. **1**, 2817 (2019).

[10] Q. Wang, T. Hisatomi, Q. Jia, H. Tokudome, M. Zhong, C. Wang, Z. Pan, T. Takata, M. Nakabayashi, N. Shibata, Y. Li, I.D. Sharp, A. Kudo, T. Yamada, and K. Domen, Nat. Mater. **15**, 611 (2016).

[11] ERIC C. EVARTS, Nature **526**, S93 (2015).

[12] H. Jin, E. Debroye, M. Keshavarz, I.G. Scheblykin, M.B.J. Roeffaers, J. Hofkens, and J.A. Steele, Mater. Horizons **7**, 397 (2020).

[13] Z.F. Huang, L. Pan, J.J. Zou, X. Zhang, and L. Wang, Nanoscale **6**, 14044 (2014).

[14] Q. Wang, T. Hisatomi, Y. Suzuki, Z. Pan, J. Seo, M. Katayama, T. Minegishi, H. Nishiyama, T. Takata, K. Seki, A. Kudo, T. Yamada, and K. Domen, J. Am. Chem. Soc. **139**, 1675 (2017).

[15] T.J. Smart and Y. Ping, J. Phys. Condens. Matter **29**, 1 (2017).

[16] H. Seo, Y. Ping, and G. Galli, Chem. Mater. **30**, 7793 (2018).

[17] J. Hu, X. Zhao, W. Chen, H. Su, and Z. Chen, J. Phys. Chem. C **121**, 18702 (2017).

[18] S. Lardhi, L. Cavallo, and M. Harb, J. Phys. Chem. C **122**, 18204 (2018).

[19] M.L. Crespillo, J.T. Graham, F. Agulló-López, Y. Zhang, and W.J. Weber, J. Phys. D. Appl. Phys. **50**, 155303 (10pp) (2017).

[20] M. Sachs, J.S. Park, E. Pastor, A. Kafizas, A.A. Wilson, L. Francàs, S. Gul, M. Ling, C. Blackman, J. Yano, A. Walsh, and J.R. Durrant, Chem. Sci. **10**, 5667 (2019).

[21] S. Corby, L. Francàs, S. Selim, M. Sachs, C. Blackman, A. Kafizas, and J.R. Durrant, J. Am. Chem. Soc. **140**, 16168 (2018).

[22] Z. Wang, X. Mao, P. Chen, M. Xiao, S.A. Monny, S. Wang, M. Konarova, A. Du, and L. Wang, Angew. Chemie - Int. Ed. **58**, 1030 (2019).

[23] J.M. Wu, Y. Chen, L. Pan, P. Wang, Y. Cui, D.C. Kong, L. Wang, X. Zhang, and J.J. Zou, Appl. Catal. B Environ. **221**, 187 (2018).

[24] Z. Zhao, R. V. Goncalves, S.K. Barman, E.J. Willard, E. Byle, R. Perry, Z. Wu, M.N. Huda, A.J. Moulé, and F.E. Osterloh, Energy Environ. Sci. **12**, 1385 (2019).

[25] Z. Li, X. Zhang, L. Zhang, C. Xu, and Y. Zhang, J. Phys. Chem. C **124**, 26214 (2020).

[26] T. Liu, X. Zhou, M. Dupuis, and C. Li, Phys. Chem. Chem. Phys. **17**, 23503 (2015).

[27] K.E. Kweon, G.S. Hwang, J. Kim, S. Kim, and S. Kim, Phys. Chem. Chem. Phys. **17**, 256 (2015).

[28] A.J.E. Rettie, W.D. Chemelewski, J. Lindemuth, J.S. McCloy, L.G. Marshall, J. Zhou, D. Emin, and C.B. Mullins, Appl. Phys. Lett. **106**, 022106 (2015).

[29] J. Wiktor and A. Pasquarello, ACS Appl. Mater. Interfaces **11**, 18423 (2019).

[30] J. Wiktor, F. Ambrosio, and A. Pasquarello, ACS Energy Lett. **3**, 1693 (2018).

[31] Y. Hermans, S. Murcia-López, A. Klein, R. Van De Krol, T. Andreu, J.R. Morante, T. Toupance, and W. Jaegermann, Phys. Chem. Chem. Phys. **21**, 5086 (2019).

[32] S. Selim, E. Pastor, M. García-Tecedor, M.R. Morris, L. Francàs, M. Sachs, B. Moss, S. Corby, C.A. Mesa, S. Gimenez, A. Kafizas, A.A. Bakulin, and J.R. Durrant, J. Am. Chem. Soc. **141**, 18791 (2019).

[33] W. Yin, S. Wei, M.M. Al-jassim, J. Turner, and Y. Yan, Phys. Rev. B **83**, 155102 (2011).

[34] F.F. Abdi, D.E. Starr, I.Y. Ahmet, and R. van de Krol, Chempluschem **83**, 941 (2018).

[35] T. Takata, J. Jiang, Y. Sakata, M. Nakabayashi, N. Shibata, V. Nandal, K. Seki, T. Hisatomi, and K. Domen, Nature **581**, 411 (2020).

[36] G. Kresse and J. Furthmüller, Phys. Rev. B **54**, 11169 (1996).

[37] J.P. Perdew and Y. Wang, Phys. Rev. B **45**, 244 (1992).

[38] P.E. Blöchl, Phys. Rev. B **50**, 17953 (1994).

[39] G. Wang, Y. Ling, X. Lu, F. Qian, Y. Tong, J.Z. Zhang, V. Lordi, C. Rocha Leao, and Y. Li, J. Phys. Chem. C **117**, 10957 (2013).

[40] J.K. Cooper, S.B. Scott, Y. Ling, J. Yang, S. Hao, Y. Li, F.M. Toma, M. Stutzmann, K. V. Lakshmi, and I.D. Sharp, Chem. Mater. **28**, 5761 (2016).

[41] T.W. Kim, Y. Ping, G.A. Galli, and K.S. Choi, Nat. Commun. **6**, (2015).

[42] W. Yao and J. Ye, J. Phys. Chem. B **110**, 11188 (2006).

[43] S.F. Sameera, P.P. Rao, L.S. Kumari, and P. Koshy, Chem. Lett. **38**, 1088 (2009).

[44] O.I. Malyi and A. Zunger, Phys. Rev. B **101**, 235202 (2020).

Chapter 7

Role of f-electrons in determining insulator to metal phase transitions of Ca $(La_{1-x}Ce_x)_2S_4$ $(0 \leq x \leq 1)$ solid solution: A DFT+U study

Hori Pada Sarker and Muhammad N. Huda*

Department of Physics, University of Texas at Arlington

Arlington, Texas 76019, United States of America

Submitted for publication at:

Journal of Applied Physics

* Corresponding author: huda@uta.edu

Abstract

We have presented a DFT+U study of structural, magnetic, electronic, and optical properties of $Ca(La_{1-x}Ce_x)_2S_4$ ($0 \leq x \leq 1$) solid solution. In conjunction with the DFT+U method, we applied spin-orbit coupling (SOC) to determine the magnetic ground state. A unique site selection technique based on local magnetic moment arrangements was applied to build the atomic arrangements for Ce doped $Ca(La_{1-x}Ce_x)_2S_4$ solid solution. The incorporation of f-electrons by Ce doping modifies the properties of the parent compound, $CaLa_2S_4$. For example, the inclusion of 25% Ce transforms the non-magnetic (NM) parent compound to an antiferromagnetic (AFM) compound, and AFM magnetic ordering remains unaltered throughout the whole solid solution series. In addition, these compounds also undergo insulator to semiconducting to metallic phase transitions as Ce concentration increases. While $CaLa_2S_4$ is an insulator, $Ca(La_{1-x}Ce_x)_2S_4$ with x = 0.25 and 0.50 are n-type semiconductor and on the other hand, compounds with x = 0.75 and 1.0 are metallic. From the calculated electronic structures, we explained these transitions. In addition, we have presented an explanation to the experimentally observed red-orange colors of $Ca(La_{0.25}Ce_{0.75})_2S_4$ and $CaCe_2S_4$ compounds.

7. 1. Introduction

Strongly correlated quantum systems manifest a variety of unique, interesting, and technologically useful phenomena, namely, Mott transition, Kondo effect, quantum criticality, superconductivity, quantum spin liquid (QSL), heavy fermion, topological insulator (TI), etc.[1–7]. These exquisite materials' behaviors stem from the effect of strongly correlated electrons. Usually, strongly correlated systems are common among transition metals and rare earth compounds where the Fermi level (E_F) crosses the d and f-bands, respectively. For example, rare earth chalcogenides having cubic Th_3P_4 structure can exhibit Mott transition as well as magnetic or superconducting behavior[8]. Rare earth oxides/chalcogenides materials possess immense importance due to their diverse technological applications[2,6,7,9–11]. However, the main challenges in developing rare-earth-based new materials are understanding the complexities that arise from the highly localized f-electrons[12–15] that impact the properties of these materials significantly. The partially or fully occupied localized f-electrons produce fascinating material phenomena, such as localized-itinerant cross-over. These intriguing properties arise due to interactions between localized f-orbitals and conduction electrons[16–20]. Moreover, theoretical modeling of the f-electron system is considered a challenge in condensed matter physics and becomes the testing ground of different electronic structure calculations methodologies. In light of this, we have studied structural, electronic, magnetic, and optical properties of $Ca(La_{1-x}\,Ce_x)_2S_4$ ($0 \leq x \leq 1$) solid solution. We have mainly addressed the following questions arised from experimental studies[21–24]: (I) what is the origin of n-type conductivity, and semiconducting to metallic phase transition of $Ca(La_{1-x}Ce_x)_2S_4$ compounds? and (II) what type of optical transition is responsible for experimentally observed color of $Ca(La_{1-x}Ce_x)_2S_4$ compounds?

To model $Ca(La_{1-x}Ce_x)_2S_4$ ($0 \leq x \leq 1$) alloy configurations, we have introduced a concept of local magnetic moment guided solid solution formation. To form the solid solution series, we have applied the local magnetic moment rule for Ca and Ce doping within the host La_3S_4. Ideally, Ln_3S_4 (Ln: La, Ce) crystalizes into cubic Th_3P_4 structure, having 3:4 stoichiometry. But in practice, cubic Ln_3S_4 structure forms cationic vacancy (one-third of the total number of cations) and transforms into 2:3 stoichiometric cubic γ-Ln_2S_3[25,26]. Consequently, a large number of cationic (magnetic or non-magnetic) impurities can be incorporated via filling the vacancy sites within the host to modify the material properties. Th_3P_4 type rare earth chalcogenides such as γ-Ln_2S_3 were shown to have extensive solid solubility of impurities[8,25–28]. In this study, 4 Ln (La/Ce) metal vacancy sites of γ-Ln_2S_3 were filled by alkaline-earth metal, Ca, and the resultant stoichiometry becomes $CaLa_2S_4$ and $CaCe_2S_4$. These stoichiometries can also be expressed as Ca doped γ-Ln_2S_3 or Ca: γ-Ln_2S_3. Note that the filling of La vacancy site by Ca atoms in $CaLa_2S_4$ was originated due to the processing difficulties that existed for synthesizing the γ-La_2S_3, which forms above 1300°C[11]. It was shown[28] that the addition of a large divalent cation like Ca stabilizes the γ-La_2S_3 at lower temperatures (600-1250° C). The role of Ca will be discussed later in the results section.

Even though these two compounds ($CaLa_2S_4$ and $CaCe_2S_4$) share the same structure, their physical properties are significantly different. $CaLa_2S_4$ behaves as an insulator with its optical absorption edge in the UV-range[21]. High transmission in 8-14μm range, thermal stability, and high corrosion resistance makes it applicable for various infrared (IR) optical applications[10,11,29–33]. On the other hand, $CaCe_2S_4$ shows metallic behavior with its red-orange color, and it is suitable as a coating material[21,34]. The other three intermediate members of the solid solution

series, i.e., (x = 0.25, 0.50) and x = 0.75, show semiconducting and metallic behavior with their characteristic colors as reported in a previous study[21].

We have performed a thorough electronic structure study to understand the role of f-electrons of $Ca(La_{1-x}Ce_x)_2S_4$ solid solution. Serendipitously, within the $Ca(La_{1-x}Ce_x)_2S_4$ solid solution there lies an effective way to study f-electron system by contrasting the electronic structure of f-electron compounds to that of an isostructural compound having no occupied f-electron as a reference. The $Ca(La_{1-x}Ce_x)_2S_4$ solid solution is such that $CaLa_2S_4$ have no occupied f-electrons, then f-electron density increases with increasing Ce concentration, and become maximum at the end member, $CaCe_2S_4$. Upon careful comparison, our calculation revealed that phase transition (magnetic as well as semiconducting to metallic) will take place as the f-electron density changes throughout the solid solution series. For example, $CaLa_2S_4$ is non-magnetic (NM) and other compounds turned out to be antiferromagnetic (AFM). A previous study[21] reported the electronic structure calculations of $Ca(La_{1-x}Ce_x)_2S_4$ solid solution using DFT-only method without spin orientation, so the magnetic moment localizations were absent. For highly localized d and f electrons, it is necessary to use post-DFT methods[35–37], such as appropriate Hubbard U parameter as well as correct spin orientation for a proper description of electronic, and magnetic properties. The present study considered DFT+U method with appropriate Hubbard U parameter to describe the localized nature of the d and f- orbitals. DFT+U method used in this study produced magnetic moment associated with Ce atoms which are in good agreement with experimental values. The paper is organized as follows: we first briefly outline the computational technique, followed by the results and discussions, and finally draw the conclusions. The presence and the impact of the 4f electrons will be highlighted by the electronic structure plots. The limitations of DFT+U method when applied to these systems will be noted as well.

7. 2. Computational Techniques

First principles spin-polarized density functional theory (DFT)[38,39] calculations were performed using the Vienna ab initio Simulation Package (VASP)[40]. The exchange and correlations were described within the generalized gradient approximation (GGA), namely by the PBE (Perdew-Burke-Ernzerhof) functional[41]. Projector-augmented wave (PAW)[42] method was employed to treat the ion-electron interaction. To model the system, we have used the conventional unit cell, 28 atoms cubic cell, with periodic boundary conditions. To determine the magnetic configurations, a larger supercell of 56 atoms was used. The S, Ca, La and Ce atoms have been described by S:$3s^2 3p^4$, Ca:$3s^2 3p^6 4s^2$, La:$5s^2 5p^6 6s^2 5d^1 4f^0$ and Ce:$5s^2 5p^6 6s^2 5d^1 4f^1$ valence electrons configuration, respectively. The first Brillouin zone (BZ) was sampled by using the Mohkhorst-Pack (MP) scheme into a 3×3×3 k-point grid for geometric optimization, and higher k-point gird has been used for density of states (DOS) calculations. For geometric optimization, the cell was fully relaxed until the residual forces on all the constituent atoms become less than 0.01 eV $Å^{-1}$. A plane wave energy cut-off of 600 eV was used throughout the calculation, which gave a well converged result. GGA-DFT has a well-known limitation of underestimating the electron self-interaction correction (SIC) error for localized electrons, especially for d and f-electrons. Because of SIC error, DFT fails to produce the correct description of lattice constants, band gap as well as magnetic behavior. To overcome the SIC error to some extent, we employed DFT+U framework[43] to study the structural, electronic, and magnetic properties of $Ca(La_{1-x}Ce_x)_2S_4$ solid solution. DFT+U theory has been proven successful towards simulating materials properties having localized electrons, especially the transition and f-electron metal oxides/sulfides[36,37,44–47]. Within this framework, the on-site Coulomb interaction term U and exchange parameter J are employed to compensate the error due to the SIC. U_{eff} = (U-J) controls

the magnitude of the SIC correction in the Duderav approach of DFT+U[43]. A representative value of U = 5 eV for La d and Ce f orbitals and a fixed value of J = 1 eV was applied in this study. Similar U values for La/Ce oxides/sulfide systems have also been reported in the previous studies[9,48,49]. For example: C. Morice et. al.[9] used U = 5 eV for both La and Ce electrons. M. Alaydrus et. al.[49] used U = 4.5 eV and 5 eV for La and Ce electrons, respectively. The chosen values of U in this study gave a reasonable description of lattice constant, band gap and magnetic behavior of $Ca(La_{1-x}Ce_x)_2S_4$ ($0 \leq x \leq 1$) solid solution. We have also applied spin- orbit coupling (SOC) to confirm the calculated magnetic ground state obtained from DFT+U method. We performed at least three independent iteration for each compound while applying SOC. For Bader charge analysis, we have used the "**Bader**" script from Henkelman's group[50]. For visualization and analysis of crystal structure, we have used the visualization software VESTA[51]. Furthermore, the procedures for Ca atoms substitution and formation of the structures for $Ca(La_{1-x}Ce_x)_2S_4$ ($0 \leq x \leq 1$) solid solutions were discussed in detail in the following section.

7. 3. Results and Discussions

7. 3. 1. Site selections for $Ca(La_{1-x}Ce_x)_2S_4$ ($0 \leq x \leq 1$) alloy configurations

Ln_3S_4 (Ln = La and Ce) adopts Th_3P_4 type structure that crystallizes into cubic symmetry with $I\bar{4}3d$ space group[26]. Within this structure, cations form a body centered cubic lattice and there are 12 symmetry equivalent (local S_4 point group symmetry) cationic sites per unit cell and each of the cation is surrounded by 8 anions, and forms distorted dodecahedron. The conventional unit cell of Th_3P_4 contains total 28 atoms- 12 cations and 16 anions. The structure of end members of $Ca(La_{1-x}Ce_x)_2S_4$ ($0 \leq x \leq 1$) solid solution series ($CaLa_2S_4$ and $CaCe_2S_4$) can be understood by considering the one third Ln-metal vacant Ln_3S_4 structure [or $Ln_{(8/3)}V_{Ln(1/3)}S_4$), where V_{Ln} symbol represents the Ln vacancy site] which is alternatively denoted as γ-Ln_2S_3 and adopts the cubic

Th_3P_4 structure. When these Ln vacancy sites are filled up by alkaline earth metal such as Ca, the resultant stoichiometry become $Ln_{(8-2y)/3}Ca_yV_{Ln(1-y)/3}S_4$ ($0 \leq y \leq 1$). With y = 1, all the Ln cation vacancy sites will be occupied by Ca ions, and the stoichiometry become the end members of the solid solution ($CaLa_2S_4$ and $CaCe_2S_4$). It is experimentally verified that filling up the Ln vacancy sites by Ca atoms form a continuous and homogeneous range of stoichiometries for the ternary $Ln_{(8-2y)/3}Ca_yV_{Ln(1-y)/3}S_4$ ($0 \leq y \leq 1$)[52]. Within this structure, Ca and Ln atoms are distributed apparently "randomly" over the 12-symmetry equivalent (local S_4 point group symmetry) sites whereas the S atoms are fully occupied within the 16 symmetry equivalent sites[25]. The Ln atomic sites within Ln_3S_4 are symmetrically equivalent without time reversal symmetry. When the local magnetic moments were imposed within the Ln_3S_4 structure, the associate local magnetic moments of Ln atoms form a groupwise pattern and each group contains 4 Ln atoms. Figure1 (a-b) shows the groupwise pattern of the associated local spin magnetic moments of Ln atoms in La_3S_4 and Ce_3S_4. The pattern of Ln magnetic moments originates from the fact that Ln atoms possess mixed valence state within cubic Th_3P_4 structure[53,54]. The orbital projected DOS as well as partial charge state of La and Ce atoms in La_3S_4 and Ce_3S_4 are also presented in the supplementary information (see in SI figure-1 and 2). We have created 4 Ln atoms vacancy by choosing one specific group of 4 Ln atoms having same magnetic moment. We then distributed the vacancy sites by 4 Ca atoms to form $CaLa_2S_4$ and $CaCe_2S_4$. These configurations indeed yield lowest energy configurations for the respective lanthanide chalcogenides.

To understanding the role of f-electrons better, we have studied a range of solid solution $Ca(La_{1-x}Ce_x)_2S_4$, where ($0 \leq x \leq 1$). To form the solid solution with x = 0.25, 0.50 and 0.75, we have used the local magnetic moment guided site selection technique discussed above. By progressively replacing La by Ce atoms from a specific group containing same magnetic moment,

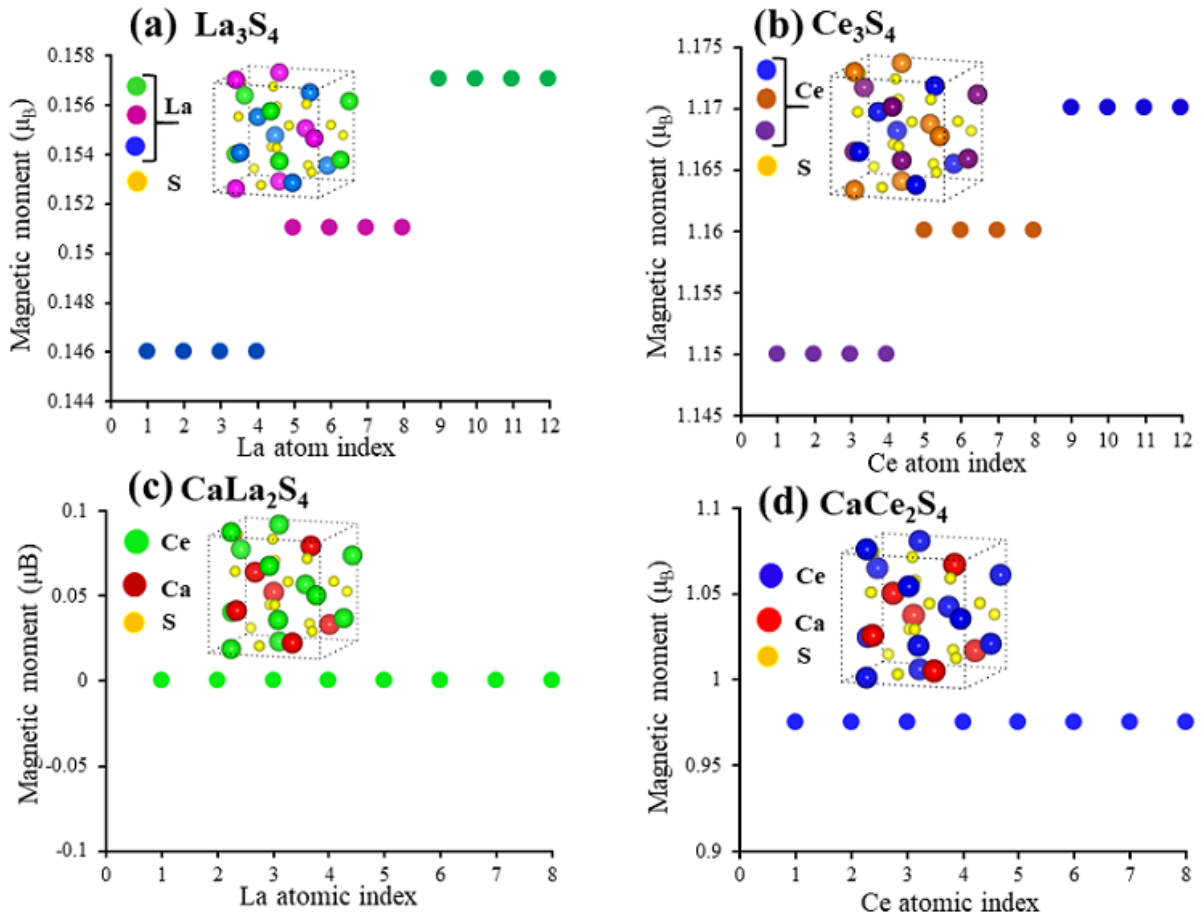

Figure-7. 1: Groups of 4 atoms having same value of local magnetic moment of La and Ce atoms within (a) La_3S_4 and (b) Ce_3S_4 structure. (c-d) The value of magnetic moment of Ln (La/Ce) atoms when a specific group of 4 Ln atoms were replaced by 4 Ca atoms. Due to Ca atom substitution, value of magnetic moment of Ln atoms decreases and the groupwise pattern of magnetic moment no longer exist. The magnetic moment value of La atoms reduced to zero. The color of dots for magnetic moment values in the plot resembles with the color of atoms in the conventional unit cell. Yellow solid spheres represent S atoms.

we formed the solid solution series of $Ca(La_{1-x}Ce_x)_2S_4$. Within the solid solution series, there is no f- electron in $CaLa_2S_4$ and f-electron increases with the increment of Ce concentration, and finally it become maximum in $CaCe_2S_4$. Figure 2 shows the crystal structure of $Ca(La_{1-x}Ce_x)_2S_4$ solid solution with their associated magnetic ordering. As shown in figure 2, the structures of these solid solutions maintain the Th_3P_4 type cubic structure. It has been previously shown that $Ca(La_{1-x}Ce_x)_2S_4$ solid solution series maintain the Th_3P_4 type structure via neutron scattering experiment[21]. Moreover, in order to determine the formation probability of $Ca(La_{1-x}Ce_x)_2S_4$ solid

solution during the synthesis process, we have calculated the formation enthalpy. The formation enthalpy, ΔH_f for a given bulk phase is defined as-

$$\Delta H_f = E_{tot}(solid) - \sum m_\alpha E_\alpha^{bulk},$$

where, $E_{tot}(solid)$ is the total energy of the system in its bulk phase, E_α^{bulk} is the energy of a single atom of atomic species α taken out from its standard elemental phase, m_α is the number of atomic species α per formula unit of the solid phase. The calculated formation enthalpies per formula unit are tabulated in Table 1. The calculated formation enthalpies for all compounds are negative which implies that these are exothermic processes. Note, we have also considered a random mix of La and Ce for $Ca(La_{1-x}Ce_x)_2S_4$ solid solution, however, the configurations obtained by site selection method via the local magnetic moments as described above were found to the more favorable ones.

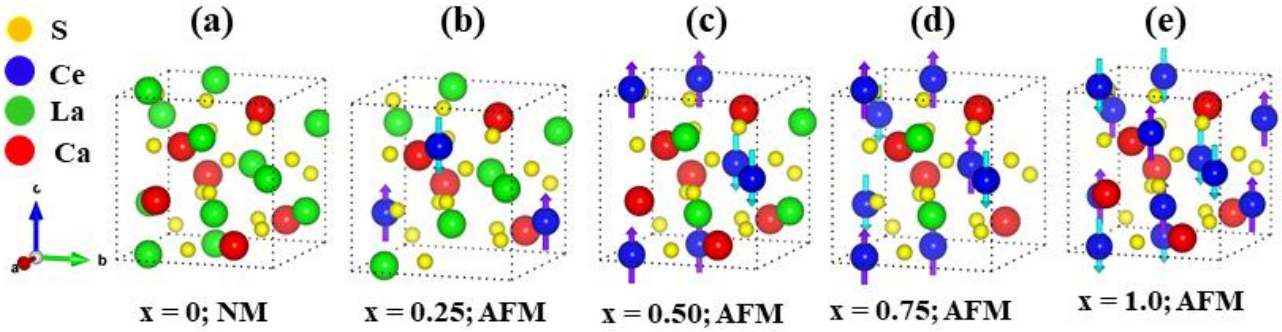

Figure-7. 2: Crystal structure of $Ca(La_{1-x}Ce_x)_2S_4$ ($0 \leq x \leq 1$) solid solution series with their respective spin ordering indicated by up and down spin at the Ce sites. (a) $CaLa_2S_4$; (b) $Ca(La_{1-x}Ce_x)_2S_4$ with x = 0.25; (c) $Ca(La_{1-x}Ce_x)_2S_4$ with x = 0.5; (d) $Ca(La_{1-x}Ce_x)_2S_4$ with x = 0.75; and (e) $Ca(La_{1-x}Ce_x)_2S_4$ with x = 1.0. NM and AFM stands for non-magnetic and anti-ferromagnetic spin orientation, respectively.

7 .3. 2. Substitutional Defect Formation energy and phase stability

The method of calculating defect formation energy of a charge-neutral system having defect Ω is[55,56],

$$E_f(\Omega) = E_{tot}(\Omega) - E_{tot}(host) + \sum_\alpha n_\alpha(\mu_\alpha + \Delta\mu_\alpha),$$

where, $E_f(\Omega)$ is the defect formation energy of the system, $E_{tot}(\Omega)$ is the total energy of the system having the defect Ω, $E_{tot}(host)$ is the total energy of the pristine system. The number n_α determines how many atoms of atomic species α is removed from or added to the system: n_α is positive if the atomic species α is removed from the system and negative if it is added to the system. μ_α is the reference chemical potential of the atomic species α in its standard elemental phase; $\Delta\mu_\alpha$ reflects the growth condition, i.e., α- rich, or α-poor growth condition. We define

Table-7. 1: Lattice constant and average cation-anion bond length of $Ca(La_{1-x}Ce_x)_2S_4$ ($0 \leq x \leq 1$) solid solution series

Ce - content (x)	**Formation enthalpy (eV)**	**Lattice constant, a (Å)**		**Average cation-anion bond length (Å)**		
		Calculated	**Experiment**[21]	**Ca-S**	**La-S**	**Ce-S**
0.00	-15.98	8.80	8.72	3.0442	3.0524	
0.25	-15.72	8.76	8.68	3.0324	3.0429	3.0191
0.50	-15.36	8.72	8.66	3.0205	3.0330	3.0118
0.75	-15.19	8.70	8.64	3.0150	3.0308	3.0090
1.00	-14.96	8.66	8.61	3.0033		2.9993

α-rich or α-poor growth condition by the following:

$$\Delta H_f \leq n_\alpha \Delta\mu_\alpha \leq 0,$$

where the lower limit $\Delta H_f \leq n_\alpha \Delta\mu_\alpha$ defines the α-poor growth condition where the availability of atomic species α is very rare. On the other hand, the upper limit $n_\alpha \Delta\mu_\alpha \leq 0$ defines the α-rich growth condition where the atomic species α is abundant within the synthesis environment.

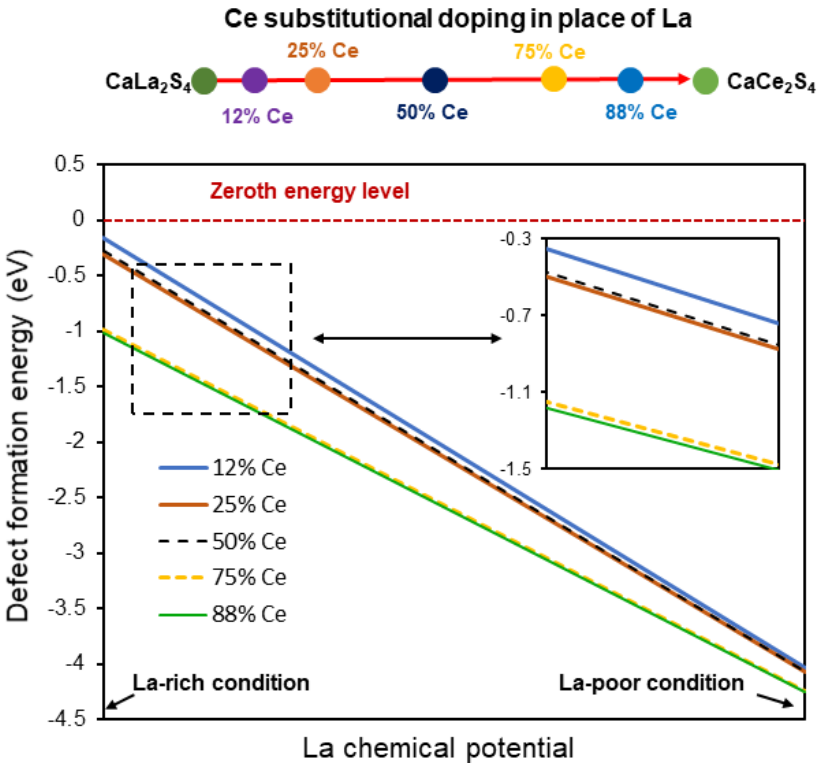

Figure-7. 3 Defect formation energy for $Ca(La_{1-x}Ce_x)_2S_4$ ($0 \leq x \leq 1$) solid solution. The zeroth energy level is indicated by the dotted red line. We excluded the end members since there is no replacement of La or Ce atoms and calculated the defect formation energy of composition as near as possible to the end members.

A defect/impurity formation energy of a system gives information about whether the system with the defect/impurity can be formed at thermodynamic equilibrium. Negative values of defect formation energy imply that the defect formation is an exothermic process. $Ca(La_{1-x}Ce_x)_2S_4$ ($0 \leq x \leq 1$) solid solution was formed by substitutional doping of Ce atoms at La sites. Figure 3 shows the defect formation energies of the entire solid solution except the end members. The defect formation energies are negative throughout the accessible range of La-chemical potentials. It is also clear that as the Ce content increases, the defect formation energy become more negative implying that the formation probability become higher as we start from the first member to the

end member of the $Ca(La_{1-x}Ce_x)_2S_4$ ($0 \leq x \leq 1$) solid solution. So, thermodynamically this solid solution is very favorable to synthesis.

7. 3. 3. Local Crystal Structure and bond length distortion

The entire $Ca(La_{1-x}Ce_x)_2S_4$ solid solution series maintain the cubic Th_3P_4 structure. Each cation (Ca/La/Ce) is coordinated with 8 anions (S atom) and forms triangular faceted irregular dodecahedron. These dodecahedra are connected to each other by means of shared faces or edges. Figure 4(a-b) shows the polyhedral model of the crystal structure with Ca, La and Ce dodecahedron. Table 1 shows the lattice constants as well as the average cation-anion bond length. The calculated lattice constants are in very good agreement (within 1%) as compared to the reported experimental (neutron diffraction) values[21]. As shown in figure 4(c), the calculated and experimental[21] lattice constants follow the similar decreasing trend with increasing Ce concentration. In addition, the lattice constants obey Vegard's law; the unit cell volume decreases linearly as the Ce concentration increases. The change of cell volume will affect the bond lengths as well as the distortion of polyhedra. We have investigated the local polyhedron distortion since these distortion has direct consequence in changing the band edge dispersion. To study the polyhedron distortion, we have used bond length distortion index, D defined by[57]-

$$D = \frac{1}{n}\sum_i^n \frac{|l_i - l_{avg}|}{l_{avg}},$$

where, l_i is the bond length from the central atom to the i^{th} coordinating atom, and l_{avg} is the average bond length from the central atom within the polyhedron. Table 1 shows that the average cation-anion bond lengths become shorter as the Ce concentration increases, which also agrees with the decreasing trend of lattice constants (figure 4(c)). Further bond length analysis shows that longer cation-anion bonds, irrespective of the cation type (Ca/La/Ce), are more affected by the increasing Ce concentration. For example, the longest and the shortest La-S bonds of 75% Ce

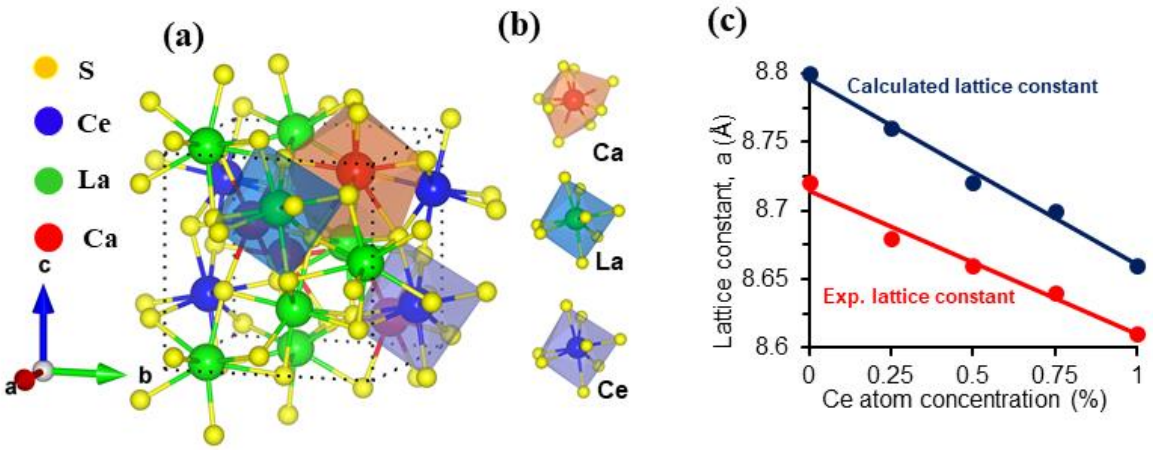

Figure-7. 4: (a) Representative polyhedral model of $Ca(La_{1-x}Ce_x)_2S_4$, x = 0.25 crystal structure; (b) Associated Ca, La and Ce polyhedron; (c) Calculated and experimental lattice constant of $Ca(La_{1-x}Ce_x)_2S_4$ solid solution. The lines are linearly extrapolated lines to show the decreasing trend of lattice constant as the Ce concentration increase. The experimental lattice constants are taken from ref. 21.

doped $Ca(La_{1-x}Ce_x)_2S_4$ shortened by 1.5% and 0.7% respectively, compared to the longest and shortest La-S bonds of $CaLa_2S_4$ (no Ce doping). In concert with bond length shortening, the bond length distortion index, D also become smaller with higher Ce concentration in the solid solution as presented in supplementary Table 1. The reduction of bond length distortion index, D within the polyhedron means that the local structures are becoming more symmetric in terms of bond length i.e., bonds within a given polyhedron are more uniform in length. The higher symmetry in the local structures with decreasing bond lengths yields more dispersive band edges. We have also previously studied[58] local distortions and their impact on band edges dispersion by using the similar method for Nb doping within $BiVO_4$ photocatalyst. This issue will be discussed again with the band structures.

7. 3. 4. Magnetic orientation and magnetic phase transition

To understand the role of f-electrons towards the magnetic behavior in $Ca(La_{1-x}Ce_x)_2S_4$ ($0 \leq x \leq 1$) solid solutions, we have calculated the magnetic exchange energy with a 56 atoms supercell

that has more flexibility to relax to a lower ground state, whereas the electronic structure calculations were done with a 28 atoms conventional unit cell. We first consider $CaLa_2S_4$ which does not have any occupied f-bands and exhibit no local magnetic moments at La-sites. Hence, $CaLa_2S_4$ turns out to be a non-magnetic system. The number of f-electrons increases gradually as more and more La atoms are replaced by Ce substitutional doping. Finally, the f-electron density become maximum at the end member of the solid solution, $CaCe_2S_4$. The Ce ($Ce:6s^24f^15d^1$) atoms have f^1 configuration in $Ca(La_{1-x}Ce_x)_2S_4$ solid solution, giving a local magnetic moment of ~0.98 μ_B per Ce ion in the present study. Loschen et. al.[44] reported Ce magnetic moment is about 0.98 μ_B within ceria (CeO_2) by DFT+U calculation. They also reported the experimental magnetic moment of Ce in ceria about 1 μ_B. Another neutron diffraction study[59] of CeF_2 reported 0.7 μ_B magnetic moment of Ce atom. So, the calculated magnetic moment of Ce ion in this study agrees well with the available reported results.

To obtain the magnetic ground state, we have considered several ferromagnetic (FM) and antiferromagnetic (AFM) configurations. Among all the configurations tested, it turned out that AFM configurations have lower energy than the FM for all compositions (x = 0.25, 0.50, 0.75, and 1.0) within $Ca(La_{1-x}Ce_x)_2S_4$ solid solution. Furthermore, the calculated exchange energy between lowest energy AFM and FM configurations for x = 0.25, 0.5, 0.75 and 1.0 are 0.028 eV, 0.043 eV, 0.037 eV and 0.028 eV per Ce atom, respectively. The exchange energies for x = 0.25 and 1.0 compositions are almost equal to the thermal energy at room temperature (K_BT~0.025 eV). So, it is possible to get paramagnetic states for these two compositions. On the other hand, at ambient condition x = 0.5 and 0.75, $Ca(La_{1-x}Ce_x)_2S_4$ compounds are likely to preserve AFM magnetic ordering with x = 0.5 being more probable. In addition, we have further tested whether the magnetic ground state obtained by DFT+U method remains the same by invoking spin-orbit

coupling (SOC). It turns out that the magnetic ordering of the compounds remains the same. So, it is clear that f-electrons via Ce substitutional doping act as a trigger for the non-magnetic (NM) to antiferromagnetic (AFM) phase transition in $CaLa_2S_4$ matrix.

From the above discussion, it can be concluded, the magnetic ordering within $Ca(La_{1-x}Ce_x)_2S_4$ solid solution depends on the positions of the f-electron contributing Ce atoms within the $CaLa_2S_4$ matrix. Figure-2(a-e) shows the crystal structures of each compound with their associated spin magnetic moment orientation. For following electronic and optical calculations, we have used the lower energy AFM structures for x = 0.25, 0.50, 0.75, and 1.0.

7. 3. 5. Electronic properties

To better understand the f-electron's role towards electronic properties, we have calculated electronic band structures and orbital projected density of states (DOS) of $Ca(La_{1-x}Ce_x)_2S_4$ ($0 \leq x \leq 1$) solid solutions. Figure-5(a-b) shows the calculated orbital projected density of states (DOS) and electronic band structure of $CaLa_2S_4$.

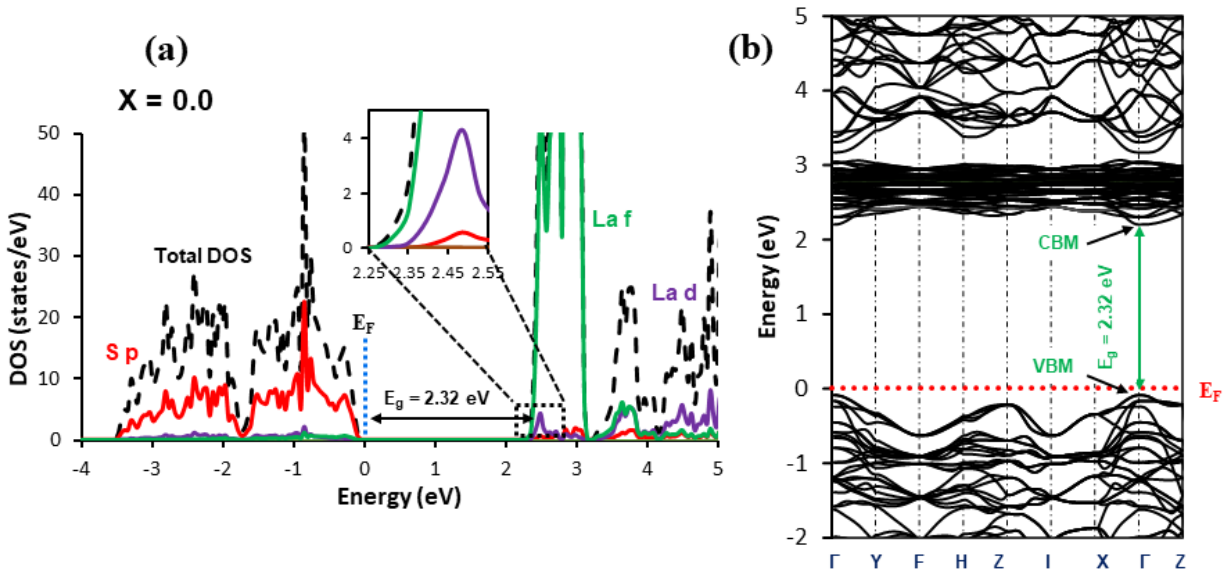

Figure-7. 5: Electronic structure of $CaLa_2S_4$. (a) Orbital projected density of states (PDOS). The Fermi level (E_F) is set to the zeroth energy level and indicated by the dashed blue line. The

amplified inset figure shows the conduction band minima. (b) Electronic band structure. The Fermi level (E_F) is also set to the zeroth energy level and indicated by the red dashed line.

As shown in the DOS plot, valence band maximum (VBM) is composed of mainly S p orbitals and the conduction band minimum (CBM) is of predominantly unoccupied La f character. Note, La f bands are unoccupied, so DFT+U method does not have significant effect on these bands. Hence the position of the La-f bands from 2.5eV to 3eV in the band structure of $CaLa_2S_4$ is similar to DFT calculations without any *U* value. This leads to the significant underestimation of the band gap, as we'll see below. At the very bottom of CBM, there are also very small contributions from La d and S p orbitals as shown in SI figure 3. Due to S p character, the VBM is dispersive along every high symmetry direction in the first Brillouin zone (BZ) (band structure is in figure 5(b)). The lower part of the CBM also shows some dispersion, which can be seen from the band structure around Γ-point. This dispersion comes from the hybridization among La d, f, and S p orbitals, as shown in amplified DOS plot in the inset figure. The DOS become sharped peaked after 2.5 eV, which produced the localized flat band region in the conduction band and these bands are solely from highly localized La f orbitals. So, the optical transition in $CaLa_2S_4$ will occur from occupied S p orbitals to unoccupied La d, f, and S p hybridized orbitals. The calculated band gap as shown in band structure for $CaLa_2S_4$ is 2.32 eV, which is same as the calculated optical gap as will be discussed below. As shown in the band structure (figure 5(b)), the VBM and CBM are located along the Γ-point and, hence, the gap is direct in nature. Yiyu et. al.[29] reported the experimental DRS band gap of $CaLa_2S_4$ powder is 2.89 eV. Another DRS experimental study[31] also reported the $CaLa_2S_4$ band gap is 2.70 eV. Batouche el. al.[30] reported calculated band gap of $CaLa_2S_4$ is 2.12 eV and 2.80 eV via GGA-WC and TB-mBJ method, respectively. Very recently Paola et. al.[21] reported SPS and DRS experimental band gaps for $CaLa_2S_4$ of 2.76 eV and 3.20 eV, respectively. Compared to the other DRS measured band gap,

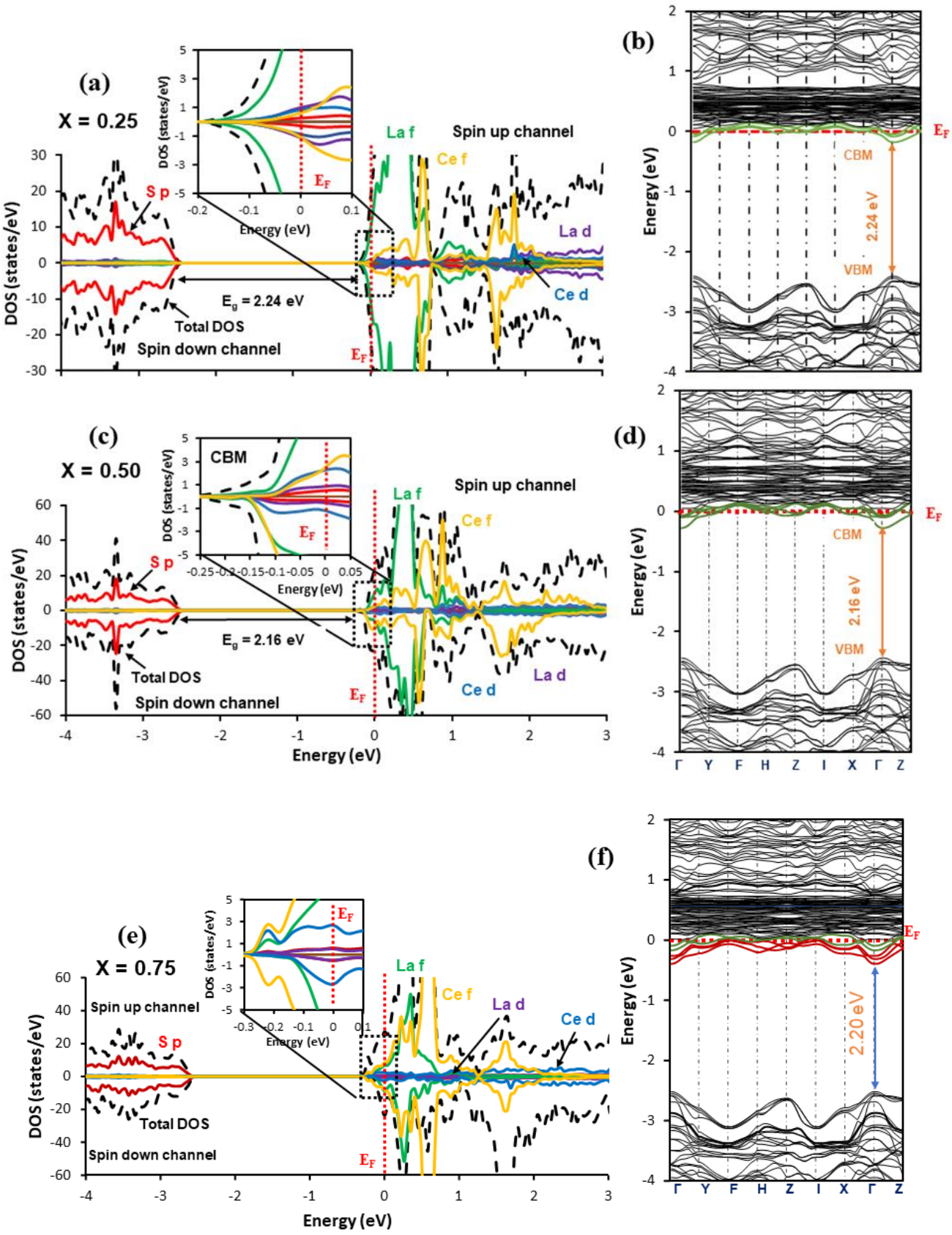
(a)
X = 0.25
DOS (states/eV)
Energy (eV)
S p
Total DOS
Spin down channel
Spin up channel
La f
Ce f
La d
Ce d
E_g = 2.24 eV
E_F
(b)
Energy (eV)
CBM
VBM
2.24 eV
E_F
(c)
X = 0.50
CBM
E_g = 2.16 eV
(d)
2.16 eV
Γ Y F H Z I X Γ Z
(e)
X = 0.75
(f)
2.20 eV

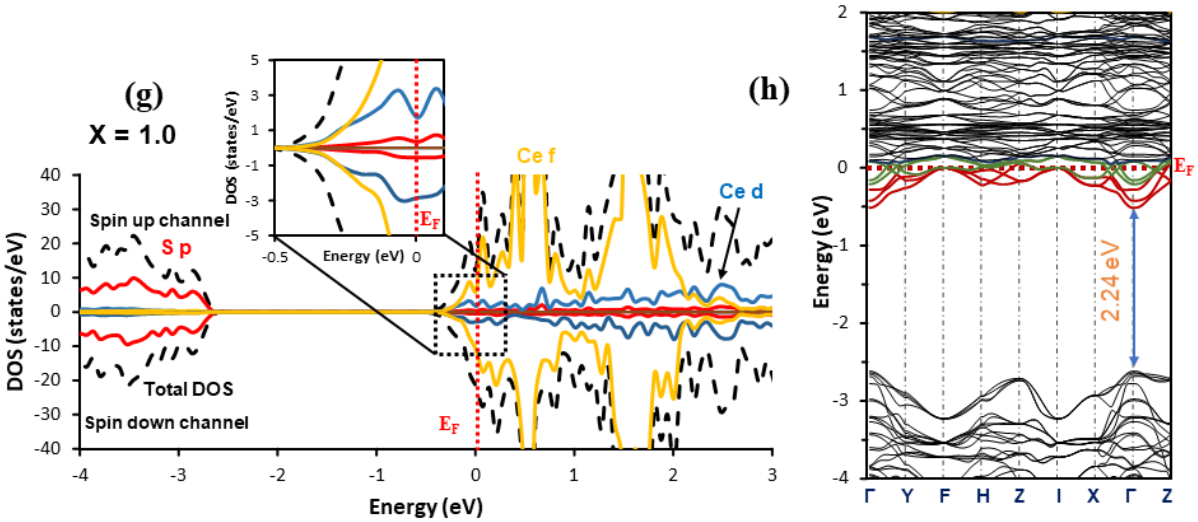

Figure-7. 6: Electronic structure of $Ca(La_{1-x}\ Ce_x)_2S_4$ ($0.25 \leq x \leq 1$) solid solution. Orbital projected density of states (DOS) and band structure- (a-b) For x = 0.25; (c-d) For x = 0.50; (e-f). For x = 0.75 and (g-h) For x = 1.0. The Fermi level (E_F) is set to the zeroth energy level and indicated by the dashed red line. The amplified inset figure shows the conduction band minima (CBM). The partially occupied bands near to the Fermi level is presented as green and fully occupied bands are presented in red.

the reported DRS band gap of ref. 21 is somehow larger by ~ (0.4 – 0.5) eV. The present GGA+U calculated band gap is close to the gap obtained by GGA-WC method[30].

However, the calculated band gap underestimates the reported experimental gap by ~ (0.4 – 0.6) eV, which can be a result of La f band being insensitive to the DFT+U, as mentioned above.

We now discuss how f-electrons modify the electronic structures in $Ca(La_{1-x}Ce_x)_2S_4$ ($0 \leq x \leq 1$) solid solution. Figure 6 (a-h) shows the calculated orbital projected density of states (DOS) and electronic band structures of $Ca(La_{1-x}Ce_x)_2S_4$ ($0.25 \leq x \leq 1$) solid solutions, respectively. As shown in the DOS plot for x = 0.25 and 0.50 compounds (figure 6(a, c)), VBM is predominantly S p character and CBM is composed of hybridized states coming from La and Ce d, f, and S p orbitals (see SI figure 4). On the other hand, Ca atoms do not have significant contribution to the electronic structure (SI figure 5 and 6 shows Ca orbital projected density of states). Ca atoms only help to overcome the synthesizing difficulty. It has been reported[28] that a small amount of

large divalent cation like Ca stabilize the cubic Th_3P_4 structure at lower temperature (~600-1250^{o}C). The instability of γ-La_2S_3 may happen due to the charge transfer imbalance between cations and anions. The Bader charge analysis as shown in SI figure 7, shows that the partial charge state of La and Ce almost stabilized with increase of Ce concentration when Ca atom is incorporated within the Ln_3S_4 (Ln = La, Ce) matrix. Like the partial charge state, the local magnetic moment of all La and Ce atoms also behave similarly in their respective phases, $CaLa_2S_4$ and $CaCe_2S_4$ as shown in figure 1(c-d). Note, within the scope of this study, after Ca doping, the local magnetic moment for all La atoms become zero. The hybridized states at the bottom of CBM produce dispersive bands. With the increment of f-electron density, hybridization become stronger, and the band dispersion at CBM also increase. Previously discussed bond length distortion index (See SI Table-1), D also showed that the Ca/La/Ce polyhedron become more symmetric as f electron density increases. The higher polyhedron symmetry eventually generates more dispersive band in the CB region. These two results are consistent with each other, implying that an increase of f-electron in the solid solution system can help increase the electron mobility by lowering electron effective mass. Importantly, across the solid solution, the band gap remains direct. The calculated band gaps for x = 0.25, 0.5, 0.75 and 1.0 compounds are 2.24eV, 2.16eV, 2.20eV and 2.24eV, respectively. These gaps are defined from the VBM to the lowest energy of the occupied conduction bands. In addition, comparison between the reference $CaLa_2S_4$ and Ce doped $Ca(La_{1-x}Ce_x)_2S_4$ compounds show some prominent changes, such as: (i) The upward shift of the Fermi level (E_F) from top of VBM to the bottom of CBM (an indication of n-type semiconducting behavior), (ii) appearance of partially and fully occupied bands at the bottom of CBM, and (iii) semiconducting to metallic phase transitions.

7. 3. 6. Effect of f-electrons

Unlike the Fermi level position of $CaLa_2S_4$ with no occupied f-electron, the Fermi level shifted to the bottom of CB for all four (x = 0.25, 0.50, 0.75 and 1.0) Ce containing $Ca(La_{1-x}Ce_x)_2S_4$ compounds. The Fermi levels are located just above (E_F-E_{CBM} < 0.5 eV) the CBM. The upshift of Fermi level towards bottom of the CB is an indication of n-type character. Surface photovoltage (SPV) measurement[21] of $Ca(La_{1-x}Ce_x)_2S_4$ compounds also justified the n-type character. This n-type behavior is originating from the fact that Ce substitutional doping supplies extra majority carrier (electron) within the system. This happens due to the mixed oxidation state of Ce ($Ce^{3+/4+}$) atoms unlike La (La^{3+}) oxidation state. The mixed oxidation state of Ce atoms was demonstrated via the partial charge state calculations using Bader charge analysis as well as atomic density of states of Ce atoms as shown in SI figure 8 and 9. These extra majority carriers generate donor levels at the bottom of the CB. The donor levels are partially filled for all $Ca(La_{1-x}Ce_x)_2S_4$ solid solutions and there are in fact fully occupied levels below the Fermi level for x = 0.75 and 1.0 composition. The partially and fully occupied bands are indicated by green and red bands as shown in the band structures (figure 6(b, d, f, h)). The number of partial and completely filled bands increase with the f-electron density due to increase of Ce atoms concentration. For x = 0.75 and 1.0, occupied states are extended about 0.4 eV and 0.5 eV below from the Fermi level, respectively. In addition, the occupied and unoccupied levels in the band structure form a continuum without any gap (see figure 6 (f and h)). Absence of band gap between occupied and unoccupied states are characteristics of metals. So, $Ca(La_{1-x}Ce_x)_2S_4$ compounds with x = 0.75 and 1.0 will have metal-like behavior. Another study[60] of cubic Ce_3S_4 also showed the similar metallic behavior. Moreover, the dispersion at the minima of conduction band also increases as the f-electron density increases. Increase of Ce concentration in $Ca(La_{1-x}Ce_x)_2S_4$ cause to reduce

volume of the crystal cell up to 4.2% with respect to the $CaLa_2S_4$. Reduction ofvolume enforces higher hybridization of Ce 5d with 4f bands, which results in as relatively larger dispersion at CBM for $CaCe_2S_4$. It is a counter intuitive scenario, where the increasing presence of highly localized f electrons are responsible for the band dispersions at the CBM. Overall, upshift of Fermi level from VBM to the bottom of the CB, generation of partially or completely filled bands below the Fermi level, a semiconducting to metallic phase transition, all are originating due to the presence of f-electrons within the matrix. So, this study suggests that we can modify the material properties of f-electron materials by tuning the f-electron density for desired properties. Note, in a recent study [21], photocurrent measurement in an electrochemical cell showed that photocurrent in $CaLa_2S_4$ is in the order of μA, whereas it is in mA in $Ca(La_{1-x}Ce_x)_2S_4$ with $x \neq 0$. The metallic behavior found in the band structures of figure 6(f) and (h) for $x = 0.75$ and 1.00, respectively is due to the underestimation of localizations in Ce d band within the DFT+U theory.

7. 3. 7. Optical properties

To elucidate the different observed color of $Ca(La_{1-x}Ce_x)_2S_4$ ($0 \leq x \leq 1$) solid solutions as reported in ref. 21, we have calculated the optical absorption coefficient, shown in figure 7(a-e). The optical gap obtained from the absorption plot shows that the gap goes through a red shift with increasing Ce concentration, x. Previously reported[21,34] diffuse reflectance spectroscopy (DRS) measurements also showed similar shift of optical transition to a longer wavelength (~500-550 nm) when Ce is introduced compared to the transition in parent $CaLa_2S_4$ that was centered about 400 nm. Further mapping of optical gap and density of states (DOS) revealed that for $x = 0.00$, 0.25 and 0.50, the optical transition happens from S 3p → La/Ce 4f orbitals. Similar type of S 3p → Ce 4f optical transition was observed in CeSF[61] and responsible for observed

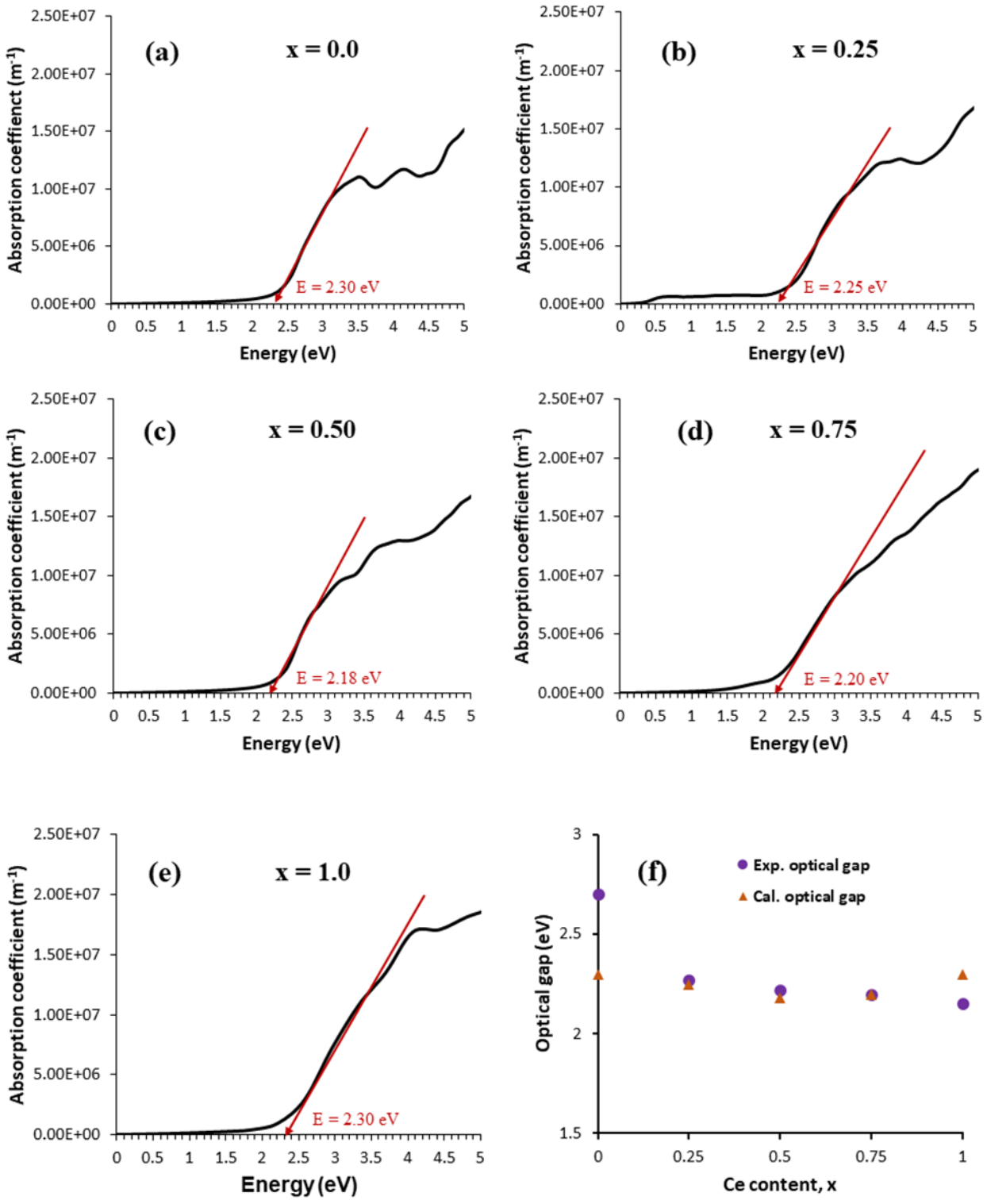

Figure-7. 7: Optical band gap for $Ca(La_{1-x}\ Ce_x)_2S_4$ ($0.25 \leq x \leq 1$) solid solution (a-e). (f) Comparison of optical gaps obtained by DFT+U calculation and DRS experiments in reference 11 and 28. The experimental band gap for CaLa2S4 was taken from reference 28

color. However, for x = 0.75 and 1.0, the optical transition happens from the completely filled Ce 4f states below the Fermi level to the unoccupied Ce 5d states within the conduction bands. Even though, these two compounds show metallic behavior, the electrons below the Fermi level will not move like free electrons in metals, rather they have to make a jump to the higher energy empty bands via optical or thermal excitation above the Fermi level. As shown in figure 6 (e, g), Ce f orbitals have dominant contribution over Ce d orbitals from Fermi level up to ~2eV and afterwards Ce d orbitals dominates. Since, the cross section of optical excitation from occupied Ce 4f → unoccupied Ce 4f is insignificant due to the forbidden nature of f→f transition, the optical transition in these two compounds will happen from Ce 4f→ Ce 5d orbitals. The Ce 4f→ Ce 5d optical transitions are intraband in nature as opposed to the interband transitions and responsible for the observed red orange colors in $Ca(La_{1-x}Ce_x)_2S_4$ compounds for x = 0.75 and 1.0. It was reported[62] that the optical transition of well-known metal chalcogenide pigments (i.e., CdS and CdSe) is also intraband and responsible for observed colors. Previously reported[62] electronic structure calculation showed that the Ce 4f → Ce 5d optical transition in alkali earth doped-Ce_2S_3 is responsible for the observed red color. So, the observed red orange color of $CaCe_2S_4$ and $CaCe_{0.75}La_{0.25}S_4$ is intrinsically caused by the presence of rare earth element, Ce and hence, the presence of f-electron. Finally, we compared the calculated optical gap with experiment[21], and they showed good agreement except for $CaLa_2S_4$ (figure 7(f)). This may imply that in La and Ce f-band mixed environments, DFT+U–predicts band gaps well due to the partially filled Ce-f bands.

Conclusion

In summary, we have presented a comprehensive study of structural, magnetic, electronic and, optical properties of two end members and three solid solutions in the series, $Ca(La_{1-x}Ce_x)_2S_4$

within the scope of DFT+U method. Within its limitations, results with DFT+U method show reasonable agreements with the available experimental results. To form the $Ca(La_{1-x}\ Ce_x)_2S_4$ solid solutions, we have used a unique site selection mechanism based on local magnetic moment arrangements on cations within the structures, which can be explored further for other magnetic systems. The f-electron incorporation via Ce doping induces magnetic as well as semiconducting to metallic phase transitions. $CaLa_2S_4$ is a non-magnetic phase and other four members of the solid solution showed AFM magnetic ordering. Here, from the band structure, due the presence of highly localized f band at the bottom of the conduction band, $CaLa_2S_4$ behaves like an insulators. The first two members (x = 0.25 and 0.50) of the solid solution showed to have n-type semiconducting behavior, which was due to the mixed valence state for Ce. On the other hand, the last two members (x = 0.75 and 1.0) showed metal-like character. It is a counter intuitive scenario, where the increasing presence of highly localized f-electrons due to Ce are responsible for the band dispersions at the CBM. The origin for this behavior was found to be two-fold: as the Ce concentration increases (i) the crystal volumes decreasd and (ii) it lowers the distortions within the polyhedral, both enhanced coupling between the cations-anions' orbitals. In addition, we have explained the optical transition mechanism for observed colors of the $Ca(La_{1-x}Ce_x)_2S_4$ compounds. For x = 0.0, 0.25 and 0.5, S 3p → La/Ce 4f are interband transition. On the other hand, for x = 0.75 and 1.0, Ce 4f → Ce 5d optical transitions are intraband and responsible for observed red/ orange color. Even though the presence of Ca is not the highlight of the study, it is known to be essential for the synthesis of these solid solutions. We have justified the presence of Ca in these rare earth chalcogenides from the first principles study. In conclusion, a better understanding of correlation between f-electron density and

different physical properties can serve as an important tool to design future technologies based on f-electron materials.

Acknowdgement

MNH was supported by the national Science Foundation (Award No. DMR-1609811). We thank the Texas Advance Computing Center (TACC) (Austin-TX, USA) for their computational needs.

Competing Financial Interests

The authors declare no competing financial interests.

Keywords

Rare earth chalcogenide, f-electron material, magnetism, insulator-metal transitions, DFT+U.

Reference:

[1] S. Raghu, X.-L. Qi, C. Honerkamp, and S.-C. Zhang, Phys. Rev. Lett. **100**, 156401 1 (2008).

[2] B. Yan, H.-J. Zhang, C.-X. Liu, X.-L. Qi, T. Frauenheim, and S.-C. Zhang, Phys. Rev. B **82**, 161108 1 (2010).

[3] F. Steglich and S. Wirth, Reports Prog. Phys. **79**, 084502 (2016).

[4] I. Aviani, M. Miljak, V. Zlatić, K.D. Schotte, C. Geibel, and F. Steglich, Phys. Rev. B **64**, 184438 (2001).

[5] H. Zheng and L.K. Wagner, Phys. Rev. Lett. **114**, 176401 1 (2015).

[6] M.B. Maple, J. Phys. Soc. Japan **74**, 222 (2005).

[7] W. Liu, Z. Zhang, J. Ji, Y. Liu, J. Li, X. Wang, H. Lei, G. Chen, and Q. Zhang, Chinese Phys. Lett. **35**, 117501 (2018).

[8] F. Holtzberg and S. Methfessel, J. Appl. Phys. **37**, 1433 (1966).

[9] C. Morice, E. Artacho, S.E. Dutton, H.J. Kim, and S.S. Saxena, J. Phys. Condens. Matter **28**, 345504 1 (2016).

[10] R.L. Gentilman, M.B. Dekosky, T.Y. Wong, R.W. Tustison, and M.E. Hills, Proc. SPIE , Infrared Opt. Mater. IV **0929**, 57 (1988).

[11] P.N. Kumta and S.H. Risbud, J. Mater. Sci. **29**, 1135 (1994).

[12] N. Tateiwa, J. Pospíšil, Y. Haga, H. Sakai, T.D. Matsuda, and E. Yamamoto, Phys. Rev. B **96**, 035125 1 (2017).

[13] T. Durakiewicz, C.D. Batista, J.D. Thompson, C.G. Olson, J.J. Joyce, G.H. Lander, J.E. Gubernatis, E. Guziewicz, M.T. Butterfield, A.J. Arko, J. Bonča, K. Mattenberger, and O. Vogt, Phys. Rev. Lett. **93**, 267205 1 (2004).

[14] Y. Onuki, Y. Inada, H. Ohkuni, R. Settai, N. Kimura, H. Aoki, Y. Haga, and E. Yamamoto, Phys. B **280**, 276 (2000).

[15] B. Johansson and S. Li, Philos. Mag. **89**, 1793 (2009).

[16] Q. Yao, D. Kaczorowski, P. Swatek, D. Gnida, C.H.P. Wen, X.H. Niu, R. Peng, H.C. Xu, P. Dudin, S. Kirchner, Q.Y. Chen, D.W. Shen, and D.L. Feng, Phys. Rev. B **99**, 081107 1 (2019).

[17] R. Peters, Y. Tada, and N. Kawakami, Phys. Rev. B **94**, 205142 1 (2016).

[18] Q.Y. Chen, X.B. Luo, E. Vescovo, K. Kaznatcheev, F.J. Walker, C.H. Ahn, Z.F. Ding, Z.H. Zhu, L. Shu, Y.B. Huang, and J. Jiang, Phys. Rev. B **100**, 035117 1 (2019).

[19] T. Duchoň, M. Aulická, E.F. Schwier, H. Iwasawa, C. Zhao, Y. Xu, K. Veltruská, K. Shimada, and V. Matolín, Phys. Rev. B **95**, 165124 1 (2017).

[20] G.L. Pascut, M. Widom, K. Haule, and K.F. Quader, Phys. Rev. B **100**, 125114 1 (2019).

[21] P. Sotelo, M. Orr, M.T. Galante, M.K. Hossain, F. Firouzan, C. Longo, A. Kormányos, H. Sarker, C. Janáky, M.N. Huda, K. Rajeshwar, and R.T. Macaluso, Inorg. Chem. **58**, 4553 (2019).

[22] R. Dagys and G.J. Babonas, J. Solid State Chem. **109**, 30 (1994).

[23] R. Dagys, G.-J. Banonas, and and G. Pukinskas, Phys. Rev. B **51**, 6995 (1995).

[24] S. Kačiulis, A. Latišenka, and A. Plešanovas, Surf. Sci. **251/252**, 330 (1991).

[25] C. Lowe-Ma, Mater. Sci. Res. **15**, 267 (1983).

[26] W.H. Zachariasen, Acta Crystallogr. **2**, 57 (1949).

[27] J. Flahaut, M. Guittard, M. Patrie, M.P. Pardo, S.M. Golabi, and L. Domange, Acta Crystallogr. **19**, 14 (1965).

[28] A.W. Sleight and C.T. Prewitt, Inorg. Chem. **7**, 2282 (1968).

[29] Y. Li, L. Zhang, and Y. Wu, RSC Adv. **6**, 34935 (2016).

[30] M. Batouche, T. Seddik, T. V. Vu, K.D. Pham, H.D. Tong, S. Uğur, G. Uğur, A.A. Lavrentyev, O.Y. Khyzhun, H.L. Luong, and A. Belfedal, Phys. B Condens. Matter **558**, 91 (2019).

[31] W.B. White, D. Chess, C.A. Chess, and J. V. Biggers, Proc. SPIE, Emerg. Opt. Mater. **297**, 38 (1981).

[32] W.B. White, Annu. Rep. to Off. Nav. Res. 1 (1981).

[33] P.J. Walker and R.C.C. Ward, Mater. Res. Bull. **19**, 717 (1984).

[34] P. Sotelo, M. Orr, M.T. Galante, M.K. Hossain, F. Firouzan, A. Vali, J. Li, M. Subramanian, C. Longo, K. Rajeshwar, and R.T. Macaluso, J. Solid State Chem. **262**, 149 (2018).

[35] M. Cococcioni, *The LDA+U Approach: A Simple Hubbard Correction for Correlated Ground States* (2012).

[36] H.J. Kulik, J. Chem. Phys. **142**, 240901 (2015).

[37] Q. Zhao and H.J. Kulik, J. Chem. Theory Comput. **14**, 670 (2018).

[38] P. Hohenberg and W. Kohn, Phys. Rev. B **136**, B864 (1964).

[39] W. Kohn and L.J. Sham, Phys. Rev. **140**, A1133 (1965).

[40] G. Kresse and J. Furthmüller, Phys. Rev. B **54**, 11169 (1996).

[41] J.P. Perdew and Y. Wang, Phys. Rev. B **45**, 244 (1992).

[42] P.E. Blöchl, Phys. Rev. B **50**, 17953 (1994).

[43] S. Dudarev and G. Botton, Phys. Rev. B **57**, 1505 (1998).

[44] C. Loschen, J. Carrasco, K.M. Neyman, and F. Illas, Phys. Rev. B **75**, 5115 (2007).

[45] J.K. Shenton, D.R. Bowler, and W.L. Cheah, J. Phys. Condens. Matter **29**, 1 (2017).

[46] Z. Hu and H. Metiu, J. Phys. Chem. C **115**, 5841 (2011).

[47] L. Petit, Z. Szotek, M. Lüders, and A. Svane, J. Phys. Condens. Matter **28**, 1 (2016).

[48] Y.L. Lee, M.J. Gadre, Y. Shao-Horn, and D. Morgan, Phys. Chem. Chem. Phys. **17**, 21643 (2015).

[49] M. Alaydrus, M. Sakaue, and H. Kasai, Phys. Chem. Chem. Phys. **18**, 12938 (2016).

[50] M. Yu and D.R. Trinkle, J. Chem. Phys. **134**, 064111 (2011).

[51] K. Momma and F. Izumi, J. Appl. Crystallogr. **44**, 1272 (2011).

[52] O. Merdrignac-Conanec, G. Durand, S. Walfort, N. Hakmeh, and X. Zhang, Ceram. Int. **43**, 5984 (2017).

[53] E. Shoko, M.F. Smith, and R.H. McKenzie, Phys. Rev. B **79**, 4108 (2009).

[54] A. Alam and D.D. Johnson, Phys. Rev. B **89**, 5126 (2014).

[55] S. Zhang, S.H. Wei, A. Zunger, and H. Katayama-Yoshida, Phys. Rev. B **57**, 9642 (1998).

[56] C. Persson, Y.J. Zhao, S. Lany, and A. Zunger, Phys. Rev. B **72**, 5211 (2005).

[57] B.H. Werner Baur, J. Acta Cryst. **B30**, 1195 (1974).

[58] H.P. Sarker, P.M. Rao, and M.N. Huda, ChemPhysChem 773 (2019).

[59] S.J. Kennedy and B.R. Coles, J. Phys. Condens. Matter **2**, 1213 (1990).

[60] J.H. Shim, K. Kim, B.I. Min, and J.S. Kang, Phys. B **328**, 148 (2003).

[61] J.M. Tomczak, L. V. Pourovskii, L. Vaugier, A. Georges, and S. Biermann, Proc. Natl. Acad. Sci. U. S. A. **110**, 904 (2013).

[62] M. Perrin and E. Wimmer, Phys. Rev. B **54**, 2428 (1996).

Chapter 8: Conclusions and future research directions

8. 1. Conclusions

In this dissertation, the state-of-the-art first principles density functional theory (DFT) has been employed to study the localized *d* and *f* bands and their concomitant effects in the strongly correlated material systems. As a representative of strongly correlated *d* and *f* electron materials, I have studied $BiVO_4$ and $Ca(La_{1-x}Ce_x)_2S_4$ ($0 \leq x \leq 1$) solid solution, respectively. In chapter 4, band structure (conduction band) modification of $BiVO_4$ by means of Nb substitution doping and the effect of hydrostatic pressure on the local structure as well as on carrier transport has been explored. In chapter 5, theoretical characterization of electron and hole polaron formation in $BiVO_4$ and the subsequent effect of polarons toward carrier transport has been studied. Polaron formation adversely effect the carrier transport as well as limit the available photovoltage in $BiVO_4$. A detail study of suppressing polaron formation in $BiVO_4$ by means of Ca and Sr aliovalent doping has been discussed in chapter 6. Finally, in chapter 7, the role of *f* electrons toward insulator to metallic phase transition as well as the optical transition responsible for experimentally observed color of $Ca(La_{1-x}Ce_x)_2S_4$ ($0 \leq x \leq 1$) compounds has been explored.

Due to the presence of localized 3d-bands at the bottom of the conduction band, $BiVO_4$ has poor electron transport as reflected by the calculated heavy electronic effective mass (~2.05 m_e) as well as the experimentally observed low photocurrent. In pursuit of enhancing electron transport, a study on band structure modification was performed by means of Nb substitutional doping at Bi and V-atomic position in $BiVO_4$ as presented in chapter 4. The results showed that simultaneous Nb doping at both sites is an energetically more favorable doping strategy than the Nb substitution at Bi or V-site separately. Simultaneous Nb doping replaces the localized V 3d bands by less localized Nb 4d bands at the bottom of the conduction band. The Nb incorporation

reduces the band gap, and band gap reduction is the highest (~0.16 eV) for combined Nb substitutional doping. Furthermore, Nb incorporation reduces the electron effective mass, and external hydrostatic pressure reduces the electron effective mass more.

Nb incorporation as well as external hydrostatic presseure reduces the electron effective mass in $BiVO_4$, but electron effective mass is still higher. On the other hand, experimental fingerprints as well as calculated band profile of $BiVO_4$ hints the formation of massive polaron quasiparticle within its crystal lattice. In chapter 5, a detailed study of theoretical characterization of polaron formation in $BiVO_4$ has been presented. The results as presented in chapter 5 showed that electron and hole polaron form at V and O-atomic sites, respectively. The formation of polaron introduces electronic states within the band gap which restrict the splitting of quasi-Fermi level of this material, and hence, limit the available photovoltage which can be achieved from this material. The result showed that the effective polaronic gap (E_{pol}) in $BiVO_4$ is ~ 1.22 eV, which is lower than the optical gap (2.40 eV), and it is even smaller than the least required potential (1.23 eV) to split water.

In addition to photovoltage limitation by polarons, polaronic mid-gap states also act like carrier recombination center and reduces the efficiency via the carrier recombination efficiency loss channel. So, in order to design highly efficient renewable energy technologies as well optoelectronic devices, the functional materials have to be free from such trapping states. Chapter 6 presented a detail study of suppressing polaron formation in $BiVO_4$ via Ca and Sr aliovalent dopping. The results as presented in chapter 6 showed that the substitutional aliovalent doping of group-II elements (Ca^{2+} or Sr^{2+}) in Bi^{3+} position in $BiVO_4$ crystal lattice completely eliminates the mid-gap trapping states originated from polaron formation. The results also showed that Ca^{2+} or Sr^{2+} doping not only suppress the mid-gap trapping states, it also completely

delocalized the localized polaronic charge throughout the whole supercell. The optical absorption spectra of Ca^{2+} or Sr^{2+} aliovalently doped $BiVO_4$ further confirmed the complete suppression of polaron in $BiVO_4$. Overall, this study showed that aliovalent doping technique can be a general technique to handle the polaronic as well as mid-band gap trapping states for other materials as well.

Lastly, the role of f-electrons in determining structural, magnetic, electronic, and optical properties of $Ca(La_{1-x}Ce_x)_2S_4$ ($0 \leq x \leq 1$) solid solution was presented in chapter 7. In this study, a unique rule based on the magnetic moment arrangement was employed for cationic site selection to form Ce containing $Ca(La_{1-x}Ce_x)_2S_4$ ($0 \leq x \leq 1$) solid solution. The results showed that depending on the f-electron density, $Ca(La_{1-x}Ce_x)_2S_4$ undergo magnetic phase transition. $CaLa_2S_4$ is non-magnetic, and on the other hand, all other Ce containing compounds showed to have anti-ferromagnetic (AFM) magnetic ordering. Results showed that similar to magnetic phase transition, there is also insulator to metallic phase transition in $Ca(La_{1-x}Ce_x)_2S_4$ ($0 \leq x \leq 1$) solid solution. $CaLa_2S_4$ is an insulator, $Ca(La_{1-x}Ce_x)_2S_4$ with x = 0.25 & 0.50 compounds are n-type semiconductor, and finally $Ca(La_{0.25}Ce_{0.75})_2S_4$ & $CaCe_2S_4$ showed to have metallic character. In addition to magnetic as well as insulator to metallic phase transition in $Ca(La_{1-x}Ce_x)_2S_4$, the optical transitions responsible for experimentally observed different colors of various Ce-containing compositions were also explained. Results showed that for x = 0.0 → 0.50 compositions, the optical transition occurs from unoccupied S 3*p* orbitals to occupied La/Ce 4*f* orbitals, and this transition is interband in nature. On the other hand, for x = 0.75 &1.0, the optical transition is intraband, and the optical transition happens from occupied Ce 4*f* orbitals at the bottom of the Fermi level to unoccupied Ce 5*d* orbitals above the conduction band. In summary, a better understanding of correlation between *f*-electron density and different physical

properties of materials can serve as an important tool to design future technologies based on *f*-electron based strongly correlated materials.

In conclusion, the studies presented in this dissertation will serve as a guidence to further improve the omnipresent limitation of poor transport properties of *d* and *f*-electron based strongly correlated materials. Furthermore, the ideas and techniques discussed in this dissertation will also further help to design *d* and *f*-electron based future technologies ranges from renewable energy to electronic to optoelectronic devices.

8. 2. Future Research Directions

The present dissertation will contribute to the understanding of the effects of *d* and *f* localized bands towards the transport behavior in strongly correlated materials systems. This dissertation will also help to understand the applicability and limitations of density functional theory (DFT), more specifically DFT+U theory, to explain the materials' properties stemming from highly localized *d* and *f* oribtals in strongly correlated materials systems. Furthermore, the contributions of this dissertation also leads to the following future research directions: (1) Exploring the kinetically stabilizing mechanisms (i.e., application of pressure, temperature, doping etc.) to stabilize metastable states; (2) Testing the accuracy and predicting power of DFT+U theory in characterizing polaron formation and polaronic energetics of other *d* and *f* electron systems; (3) Further exploration of the efficacy of aliovalent doping technique of removing localized mid-gap electronic states; (4) Exploring and testing the magnetic moment guided site-selection rule to other magnetic materials; (5) Further testing of the applicability of post-DFT theories in explaining the transport properties of strongly correlated materials systems.